The role of C-O-H volatiles in the martian mantle and the production of the martian atmosphere

A DISSERTATION
SUBMITTED TO THE FACULTY OF THE GRADUATE SCHOOL
OF THE UNIVERSITY OF MINNESOTA
BY

Benjamin Danforth Stanley

IN PARTIAL FULFILLMENT OF THE REQUIREMENTS
FOR THE DEGREE OF
Doctor of Philosophy

Marc M. Hirschmann

August, 2012

Acknowledgements

This document would not exist without a lot of help along the way. First and foremost is my advisor, Marc Hirschmann, who has consistently pushed me to think and analyze my results. I am a better scientist thanks to him. A close second comes Tony Withers whose constant patience and willingness to help other members of our group have cost him time to write more publications than I want to think about. Thanks also go to the remaining members of my committee, David Kohlstedt and, especially, Martin Saar for stepping up at the last minute and joining my committee just a bit before my preliminary oral examination.

The Experimental Petrology group, my extended family over the last five years, have provided thought provoking questions, humorous moments, and unforgettable friendships. Many thanks go to: Travis (my grad mentor and softball idol), Fred (my music consultant and dissertation buddy), Paola (my chocolate pusher), Patrick (my fantasy sports commrade-in-arms), and Anja (my well-traveled translator). To the Ph.D. students left behind, Hong-luo and Johnny, I say good luck and remember to ask lots of questions! Thanks to the undergraduate (and recently graduated) students that have passed through the lab and left their impression on me: Michael Mournier, Douglas Schaub (co-author of Chapter 3), and Neil Foley.

Other members of the department that have been amazing, and deserve many thanks, include: Ellery Frahm (thanks for the patience during my ongoing-duel with the microprobe!), Sharon Kressler and the rest of the department staff, Lars and Elissa, Ryan N. and Stephanie, Marylee, Brady and Josh, Laura, Erkan, Nono and Ioana, Ryan L. and Emily, Dave and Lindsay (who wrote me letters of recommendation while dealing with a newborn!), and the folks next door/Kohlstedt group. Oh, and thanks to the folks who develop LaTeX! This dissertation is written using it and it made my life so much easier during the final stretch!

I am grateful for the funding for this work was provided by: several departmental fellowships, NASA Mars Fundamental Research grants 07-MFRP07-0038 and 10-MFRP10-0069, the

FTIR that made my life so much easier was purchased by NSF grant EAR0930034, and finally the University of Minnesota Doctoral Dissertation Fellowship (2011-2012).

More personally I would like to thank my family for their continued, and amazing, support during my graduate career. To my father, who provided perspective from afar while listening to all my little problems. To my mother, who provided wonderful naggings at appropriate times, support always, and easy flights home to see her. To my sister, who knows the problems I've faced better than most, and who will eventually show the bio-chem-micro science world that she's awesome. To the extended in-law-family in York, thanks for accepting me and making life entertaining.

This dissertation is the result of lots of long hours of hard work that would not have been possible without my furkids (Mozie and Tess) and wonderful wife. Val, you are my rock, my best friend, my veggie pusher, and my kick in the pants. You have celebrated with me and consoled me. Without you I would have fallen apart long ago and I will never be able to thank you enough for helping me achieve this while putting your own life on hold. I owe you more back massages and long lazy days together than we can fit into our lifetimes, but I will try.

Abstract

Evidence suggests that liquid water was once eroding the martian surface at rates comparable to many climates on present-day Earth. However, the thin modern martian atmosphere does not support liquid water. The fundamental variable in the evolution of the martian atmosphere is the storage of C-O-H volatiles in the interior, and the processes and fluxes leading to ventilation of those volatiles to the atmosphere. A key constraint on the likely CO_2 fluxes accompanying martian magmatism is that much of the martian mantle is thought to be sufficiently reduced, between the iron-wüstite buffer (IW) and one log unit above IW (IW+1), such that carbon resides principally as graphite. In a reduced, graphite-saturated mantle there is a simple relationship between CO_2 solubility and oxygen fugacity (f_{O_2}) which shows that an order of magnitude increase in oxygen fugacity changes the amount of CO_2 dissolved in the melt by one order of magnitude.

This thesis presents experimental investigations of the solubility of CO_2, and other C-O-H species, in martian basalts and the implications for martian atmospheric evolution through three sets of laboratory-based experiments. In Chapter 2, experimental carbonate solubility is determined in a synthetic melt based on the Adirondack-class Humphrey basalt at 1-2.5 GPa, and 1400-1650 °C. Experimentally determined CO_2 solubilities are used to model the production of an early martian greenhouse. For the Humphrey source region, constrained by phase equilibria to be near 1350 °C and 1.2 GPa, the resulting CO_2 contents are 51 ppm at the IW, and 510 ppm at IW+1. However, solubilities are expected to be greater for depolymerized partial melts similar to primitive shergottite Yamato 980459 (Y 980459) which are investigated in Chapter 3. Similar experiments are performed on a synthetic starting material based on Y 980459. Despite large differences in FeO* (Fe_2O_3+FeO) and MgO contents, the CO_2 solubilities in Y 980459 are similar to those in a less primitive Humphrey rock and a Hawaiian tholeiite. The small sensitivity of CO_2 solubility to compositional variations among martian and tholeiitic basalts means that the experimentally determined solubilities may be applicable to a wide spectrum of martian magmatic products. In Chapter 4, the extraction of C-O-H volatiles from the Martian mantle is determined using the dissolved concentrations of C-O-H volatiles as a function of oxygen fugacity in synthetic martian magmas coexisting with graphite. CO_2 solubilities change by one

order of magnitude with an order of magnitude change in oxygen fugacity, as predicted by previous work. Other reduced species, such as Fe-carbonyls and amides, are detected in reduced graphite-saturated martian basalts. An atmosphere produced by degassing of magmas similar to this study would be richer in C-O-H species than previously modeled using only CO_2 and could create a much warmer climate that stabilizes liquid water on the ancient martian surface.

Contents

List of Tables

List of Figures

Chapter 1

Introduction

The evidence for stable liquid water on the surface of Mars early in its history (e.g., *Pollack et al.*, 1987; *Craddock and Maxwell*, 1993) requires the presence of a much stronger greenhouse atmosphere in the past relative to the current atmosphere. The composition of this early atmosphere is thought to be mostly CO_2 (*Pollack et al.*, 1987; *Carr*, 1999; *Jakosky and Phillips*, 2001) and many models exist to explain the evolution of such an early CO_2-rich martian atmosphere (*Pepin*, 1994; *Carr*, 1999; *Manning et al.*, 2006; *Hirschmann and Withers*, 2008). The most common influx used in these models is volcanic outgassing during early crustal formation and the construction of the Tharsis magmatic province. A key constraint on the likely CO_2 fluxes accompanying martian magmatic output is that much of the martian mantle is thought to be sufficiently reduced, between the iron-wüstite buffer (IW) and one log unit above IW (IW+1), such that carbon resides principally as graphite. In a reduced, graphite-saturated mantle there is a simple relationship between CO_2 solubility and oxygen fugacity which shows that an order of magnitude increase in oxygen fugacity, f_{O_2}, changes the amount of CO_2 dissolved in the melt by one order of magnitude.

This thesis presents experimental investigations of the solubility of carbon dioxide in martian basalts and the implications for martian atmospheric evolution. High pressure and temperature experiments were conducted in a piston-cylinder apparatus at the Experimental Petrology Laboratory at the University of Minnesota. Experimental conditions ranged from 1-3 GPa, and 1340-1650 °C with synthetic starting materials that consisted of a martian basalt similar to the Humphrey rock discovered in Gusev Crater (Chapter 2) and a basalt similar to the olivine-pyhric

shergottite Yamato 980459 (Y 980459) meteorite (Chapter 3). In chapter 4 the starting materials included mixes of Humphrey oxidized and reduced starting powder, to vary the oxidation state of the experiment, with synthetic martian olivine and pigeonite, and later experiments with Fe metal added to reduced the charge further. Examination of experimental run products involved electron microprobe analysis (EMP) to determine phase compositions in all studies. EMP analyses were carried out on the JEOL JXA8900R electron microprobe in the Department of Earth Sciences at UMN. In all studies, the solubilities of CO_2 and H_2O in quenched glass were characterized by Fourier transform infrared spectroscopy (FTIR) using a Bruker Tensor 37 FTIR spectrometer and Hyperion 2000 microscope at the Experimental Petrology Laboratory at UMN. In chapter 2, Mössbauer spectroscopy analyses were conducted by Thelma Berquó at the Institute for Rock Magnetism, Department of Earth Sciences, UMN. Chapter 4 includes analyses performed on the Cameca 6f secondary ion mass spectrometer (SIMS) at Arizona State University. Glass thickness and Raman spectroscopy measurements were carried out on the Confocal Raman microscope in the Institute of Technology Characterization Facility, UMN.

The present work attempts to quantify the solubility of C-O-H volatiles in a reduced martian mantle and, therefore, the outgassing potential of those magmas. A brief description of each chapter is given here.

Chapter 2 presents experiments determining the CO_2 solubility in a synthetic melt based on the Adirondack-class Humphrey basalt. High-pressure experiments are performed in Fe-doped Pt capsules with both oxidized and reduced starting materials. The experimental CO_2 solubilities allow calibration of the thermodynamic parameters governing dissolution of CO_2 vapor as carbonate in silicate melt. This relation, combined with the known thermodynamics of graphite oxidation, facilitates calculation of the CO_2 dissolved in magmas derived from graphite-saturated martian basalt source regions as a function of P, T, and f_{O_2}. The resulting model of martian atmospheric evolution concludes that if typical martian volcanic activity was reduced and the melting conditions cool, then degassing of CO_2 to the atmosphere may not be sufficient to create greenhouse conditions required by observations of liquid surface water.

Chapter 3 focuses on the effect of composition on the CO_2 solubility of martian basalts. Piston-cylinder experiments are performed on a synthetic melt based on the martian meteorite Yamato 980459, an olivine-phyric shergottite and a picritic rock (19 wt% MgO) thought to be a near-primary liquid derived from high temperature (>1540 °C) partial melting of the martian mantle. Despite large differences in FeO* and MgO contents, the CO_2 solubilities in Y 980459

are similar to that in a less primitive synthetic martian basalt based on the Humphrey rock and to a Hawaiian tholeiite. The thermodynamic parameters governing dissolution of CO_2 vapor as carbonate in silicate melt are calculated using the new data and applied to the hot conditions in the source of Y 980459. This is used as an analog for plume-related magmas forming the giant Tharsis volcanic complex, which accounts for 50% of martian igneous activity since stabilization of the primordial crust. The new parameterization concludes that the entire Tharsis event would outgas 30-300 mbars of CO_2 (at IW to IW+1 respectively) to the martian atmosphere, which is far from the 2 bars required to stabilize an equable climate in the late Noachian and early Hesperian epochs.

Chapter 4 experimentally investigates the effect of oxygen fugacity on the CO_2 solubility of graphite-saturated martian basalts. Piston-cylinder experiments are performed in Pt-graphite double capsules with a range of starting materials using synthetic Humphrey as a base. The linear relationship between CO_2 and f_{O_2} is confirmed over oxygen fugacities from ~IW+2 to ~IW-1. Other reduced C-O-H species, such as Fe-carbonyls and amides, are detected by FTIR in experimental glasses. These species are associated with the measured difference between total C contents by SIMS and CO_2 contents by FTIR. It is likely that a martian atmosphere produced by degassing magmas similar to this study could produced a thick greenhouse capable of stablizing liquid water on the surface.

Chapter 2

CO_2 solubility in martian basalts and martian atmospheric evolution

This chapter has been published in Geochimica et Cosmochimica Acta, vol. 75, pg. 5987–6003 with co-authors Marc M. Hirschmann and Anthony C. Withers, and is used in this dissertation with permission from Elsevier.

2.1 Introduction

There is considerable evidence that liquid water was stable on the ancient martian surface during at least some parts of the late Noachian and early Hesperian epochs (e.g., *Pollack et al.*, 1987; *Craddock and Maxwell*, 1993; *Mangold et al.*, 2004; *Squyres et al.*, 2004; *Fassett and Head*, 2008; *di Achille et al.*, 2009; *Dehouck et al.*, 2010; *di Achille and Hynek*, 2010). Given the Sun's distance from Mars and its lower irradiance early in solar system history, such equable conditions seemingly require a thick greenhouse in the ancient martian atmosphere (*Pollack et al.*, 1987; *Pepin*, 1994; *Sagan and Chyba*, 1997). Yet there remains considerable uncertainty as to how this greenhouse was created and maintained and how it evolved to the current thin, modern atmosphere. The most common supposition is that the greenhouse was composed chiefly of CO_2 (*Pollack et al.*, 1987; *Pepin*, 1994; *Carr*, 1999; *Jakosky and Phillips*, 2001; *Manning et al.*, 2006; *Craddock and Greeley*, 2009) and maintained by significant volcanic outgassing (*Pepin*, 1994; *Carr*, 1999; *Phillips et al.*, 2001), although there are alternative models arguing for SO_2 or CH_4 as principle gases in the early martian greenhouse (*Brown and Kasting*, 1993; *Squyres*

and Kasting, 1994; *Fairèn et al.*, 2004; *Bullock and Moore*, 2007; *Chevrier et al.*, 2007; *Halevy et al.*, 2007; *Gaillard and Scaillet*, 2009; *Righter et al.*, 2009).

A key limit on the history of the martian atmosphere is the supply of volcanogenic CO_2. This flux has been modeled (*Pepin*, 1994; *Carr*, 1999; *Manning et al.*, 2006; *Hirschmann and Withers*, 2008; *Craddock and Greeley*, 2009) based on the time-integrated volume of volcanism (*Greeley and Schneid*, 1991) and estimates or models of the CO_2 dissolved in martian magmas. Many models of martian atmospheric evolution utilize a range of CO_2 concentrations in martian magmas based on the assumption that martian lavas have CO_2 concentrations similar to those in Hawaiian or Icelandic basalts (*Craddock and Greeley*, 1995; *Phillips et al.*, 2001; *Manning et al.*, 2006; *O'Neill et al.*, 2007; *Craddock and Greeley*, 2009). However, Hirschmann and Withers (2008) argued that this assumption is unjustified. They noted that primitive martian magmas come from sources with low oxygen fugacities and that the capacity of these magmas to dissolve CO_2 is greatly diminished under reducing conditions. Consequently, understanding the volcanogenic flux of CO_2 to the martian atmosphere requires constraints on the oxygen fugacity of primitive martian magmas and on the relationship between oxygen fugacity and CO_2 solubility of martian-composition basalts.

Observations on SNC (Shergotty, Nakhla, Chassigny) meteorites show that the oxygen fugacities prevailing in martian igneous rocks span a wide range, from the iron-wüstite (IW) to quartz-fayalite-magnetite (QFM) buffers (e.g., *Hale et al.*, 1999; *Wadhwa*, 2001; *Herd et al.*, 2002; *Dyar*, 2003; *Herd*, 2003; *Dyar et al.*, 2005; *Herd*, 2006; *Shearer et al.*, 2006; *Karner et al.*, 2007; *Righter et al.*, 2008). This range has been interpreted as relating to different contributions of reduced depleted mantle and an oxidized component deriving from either the crust or from enriched mantle domains (*Herd*, 2003). For example, the two most isotopically primitive meteorites, QUE 94201 and Y 980459, are also the most reduced, yielding oxygen fugacity measurements between the IW and IW+1 (*Borg et al.*, 1997; *Borg and Draper*, 2003; *McKay et al.*, 2004; *Musselwhite et al.*, 2006). Recent estimates of the oxygen fugacities for the Gusev basalts indicate that they are similarly reduced and imply that the range of f_{O_2} in martian mantle is relatively restricted (*Schmidt et al.*, 2011). We assume that reduced conditions are the most relevant for constraining the volcanogenic fluxes of CO_2 from the martian interior to the atmosphere for the following reasons: First, the crust is not a source of juvenile carbon. Any carbon stored in the crust and released by crustal magmatism derives ultimately from the mantle. Second, isotopic constraints require that enriched mantle domains, if present, must

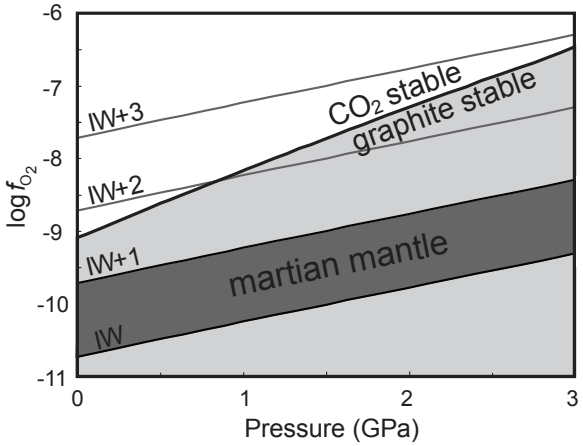

Figure 2.1: Graph of CO_2 and graphite stability fields with respect to f_{O_2} and pressure, calculated from Frost and Wood (1997). The f_{O_2} range for the martian mantle, IW to IW+1, is plotted to show that for all relevant pressures (1-2 GPa) the standard martian mantle conditions fall in the graphite stability field. Modified from Hirschmann and Withers (2008).

be volumetrically subordinate to depleted domains, as the $^{87}Sr/^{86}Sr$ of the former (up to 0.72, *Herd*, 2003) are well in excess of any plausible bulk martian composition (*Borg et al.*, 1997).

If the oxygen fugacity of the martian mantle is between IW and IW+1, then, as pointed out by Hirschmann and Withers (2008), carbon in the shallow martian mantle is stored as graphite (Fig. 2.1). The solubility of carbon as carbonate into partial melts is controlled by the prevailing fugacity of CO_2 (f_{CO_2}) according to the reaction

$$\underset{\text{gas}}{CO_2} + \underset{\text{melt}}{O^{2-}} \rightleftharpoons \underset{\text{melt}}{CO_3^{2-}} \tag{2.1}$$

which has an equilibrium constant given by

$$K_{\text{II}} = \frac{X^{\text{melt}}_{CO_3^{2-}}}{\left(X^{\text{melt}}_{O^{2-}}\right) f_{CO_2}} \tag{2.2}$$

where $X^{\text{melt}}_{O^{2-}} = 1 - X^{\text{melt}}_{CO_3^{2-}}$(*Holloway et al.*, 1992; *Holloway*, 1998). The value of K_{II} must be calibrated from experimental determinations of CO_2 solubility on a melt of appropriate composition. For graphite-saturated magmas, f_{CO_2} is related to f_{O_2} by the reaction:

$$\underset{\text{graphite}}{C} + \underset{\text{gas}}{O_2} \rightleftharpoons \underset{\text{gas}}{CO_2} \tag{2.3}$$

which is described by the equilibrium constant

$$K_{\text{I}} = \frac{f_{CO_2}}{f_{O_2}} \tag{2.4}$$

and which can be calculated from basic thermodynamic data for graphite and O_2 and CO_2 vapor (e.g., *Holloway et al.*, 1992). For graphite-saturated magmas, combining Eqns. 2.2 and 2.4 allows calculation of the mole fraction of dissolved carbonate

$$X^{\text{melt}}_{CO_3^{2-}} = \frac{K_{\text{I}} K_{\text{II}} f_{O_2}}{1 + K_{\text{I}} K_{\text{II}} f_{O_2}}. \tag{2.5}$$

This results in a simple relationship between oxygen fugacity and CO_2 solubility (Eqn. 2.5), in which an order of magnitude increase in oxygen fugacity changes the amount of CO_2 dissolved in the melt by one order of magnitude (*Hirschmann and Withers*, 2008). However, application of Eqn. 2.5 to CO_2 solubility in martian magmas requires calibration of K_{II} appropriate for martian basaltic compositions. For lack of a more appropriate analog, Hirschmann and Withers (2008) used values of K_{II} calibrated from Hawaiian basalt (*Pan et al.*, 1991). Observations of SNC meteorites (e.g., *Bridges and Warren*, 2006), and rover investigations on the martian surface (*Gellert et al.*, 2006; *McSween et al.*, 2006a) indicate that martian igneous rocks are highly enriched in FeO* and depleted in Al_2O_3 compared to terrestrial basalts. Therefore, in this study we have measured the solubility of CO_2 in a composition that more nearly matches the composition of martian basalts.

In addition to variations in dissolved of CO_2 in martian basalts that derive from diminished fugacity of CO_2 under reduced conditions (Eqns. 2.3 and 2.4), an additional effect of oxygen fugacity may arise owing to variations in the oxidation state of Fe. Because martian basalts are Fe-rich, with close to 20 wt% FeO*, the relative concentrations of Fe_2O_3 and FeO could be important factors in the chemical behavior of martian magmas, potentially influencing the solubility of CO_2. The structural roles of Fe^{2+} and Fe^{3+} in silicate melts remain uncertain. Fe^{3+} is generally considered a tetrahedrally coordinated network-forming ion in basalts (e.g.,

Wilke et al., 2006, 2007; *Rossano et al.*, 2008; *Giuli et al.*, 2011), but the structural role of Fe^{2+} is more controversial. Some have considered it an octahedrally coordinated network-modifying ion similar to Ca^{2+} (*Boon and Fyfe*, 1972; *Mysen et al.*, 1982; *Virgo and Mysen*, 1985), but EXAFS (e.g., *Farges et al.*, 2005; *Wilke et al.*, 2007; *Giuli et al.*, 2011), XANES (e.g., *Galoisy et al.*, 2001; *Magnien et al.*, 2004; *Wilke et al.*, 2006, 2007; *Giuli et al.*, 2011), and Mössbauer (*Rossano et al.*, 1999; *Jayasuriya et al.*, 2004; *Mysen*, 2006; *Rossano et al.*, 2008) spectroscopies show that in glasses it has a coordination number of 4-5, giving it a structural role similar to Fe^{3+}. In part for this reason, Brooker et al. (2001a) argued that the solubility of CO_2 in a range of natural and synthetic silicate melts is best reconciled if Fe^{2+} and Fe^{3+} have similar structural roles in silicate melts, both acting as network formers. By employing both oxidized and reduced starting materials, this present study allows further investigation of the role of iron valence state in CO_2 solubility.

2.2 Methods

2.2.1 Experimental methods

The initial starting material for this study consists of a synthetic powder similar in composition to the Adirondack-class, olivine-phyric basalts discovered by the Mars Exploration Rover Spirit in Gusev Crater (*Gellert et al.*, 2006; *McSween et al.*, 2006a, Table 2.1). The powder was provided by Justin Filiberto and synthesized from a mixture of oxides to be compositionally similar to the Humphrey basaltic rock (*Filiberto et al.*, 2008). Work by Filiberto et al. (2008) suggests that the Humphrey composition represents a basaltic liquid, making it an ideal starting material for this experimental study.

To study the effect of variable oxidation state of Fe, we wished to employ starting materials that were both reduced and oxidized. The original starting material provided to us was highly oxidized, with iron chiefly in the ferric state (see below for a description of Mössbauer analyses and Table 2.2, for results). Therefore, a portion of the starting material was reduced at 1250 °C in a gas-mixing furnace for 12 h in a CO-CO_2 gas stream at an oxygen fugacity near QFM-1. Iron in the resulting material was chiefly divalent (Table 2.2).

To the starting basaltic compositions, 3 wt% CO_2 was added as silver oxalate, $Ag_2(CO_2)_2$, which dissociates to Ag metal and CO_2 at 140 °C. Pan et al. (1991) showed that the presence of Ag metal in the charge has no influence on the solubility of CO_2 in the silicate melt. The

Table 2.1: Compositions (wt%) of starting material compared to published compositions of Humphrey martian basalt.

Oxide	Gellert et al. (2006)	McSween et al. (2006a)	Filiberto et al. (2008)	This study
SiO_2	46.96	46.49	45.99	46.91
TiO_2	0.56	0.59	0.56	0.53
Al_2O_3	10.93	10.55	10.89	10.52
FeO^T	19.23	18.95	20.01	19.87
MnO	0.42	0.43	0.42	0.38
MgO	10.65	10.82	10.89	10.79
CaO	8.02	8.26	8.12	7.99
Na_2O	2.56	2.38	2.44	2.40
K_2O	0.10	0.09	0.10	0.11
P_2O_5	0.57	0.60	0.58	0.52
FeS	0.00	0.84	0.00	0.00
Total	100.00	100.00	100.00	100.00
Source	Rover	Rover	Microprobe	Microprobe

FeO^T = total iron (Fe_2O_3 + FeO). Compositions are calculated Cr-free and normalized.

mixtures of basalt powder and silver oxalate were homogenized in an agate mortar under ethanol for 1 h.

Experiments were performed in 2 mm Pt capsules that were iron-presaturated to prevent loss from the starting material during the experiment. Presaturation was accomplished by melting powdered V25-RD1-T1C basalt (*Aubaud et al.*, 2004) in the capsules in a gas-mixing furnace for 24 h at 1250 °C and a CO-CO_2 atmosphere adjusted to an oxygen fugacity of approximately QFM-2.5. These conditions were chosen to ensure that the iron in the glass was chiefly divalent and that it alloyed with the Pt capsule in large amounts. The basaltic glass was then removed by immersion in a bath of warm hydrofluoric (HF) acid for 2-3 days.

Saturation experiments were performed at pressures ranging from 1.0-2.5 GPa and 1400-1625 °C in a half-inch (12.5 mm), end-loaded piston-cylinder apparatus under hot piston-in conditions. Run durations of 30 min were chosen to prevent significant gain of hydrogen or loss of iron during the experiment. Conditions for individual experiments are listed in Tables 2.3 and 2.4.

Integrated molar absorptivity experiments (section 2.2.2) were held at 1500 °C and 2 GPa

Table 2.2: Magnetic hyperfine parameters at room temperature for Mössbauer analyses on starting materials and experimental glasses.

	$B_{HF}(T)$	QS (mm/s)	IS (mm/s)	%	Iron phase
Oxidized starting material	47.5 (5)	0.23 (5)	0.40 (2)	9 (2)	Ti-magnetite
	43.8 (2)	0.13 (5)	0.44 (2)	9 (2)	
	-	1.21 (2)	0.30 (1)	70 (2)	Fe^{3+}
	-	1.90 (2)	1.04 (3)	12 (2)	Fe^{2+}
Oxidized experimental glass	-	1.17 (3)	0.31 (1)	82 (2)	Fe^{3+}
	-	2.10 (4)	1.05 (2)	18 (2)	Fe^{2+}
Reduced starting material	-	1.86 (1)	1.13 (1)	18 (2)	Fe^{2+}
	-	2.85 (1)	1.15 (1)	82 (2)	
Reduced experimental glass	-	0.88 (4)	0.52 (1)	32 (5)	Fe^{3+}
	-	2.11 (1)	1.05 (1)	68 (5)	Fe^{2+}

B_{HF} – magnetic hyperfine parameters, QS – quadrupole splitting, IS – isomer shift and % – relative proportion. Values in parentheses are uncertainties in analyses in terms of least digits cited.
The Fe^{2+} and Fe^{3+} contents of Ti-magnetite were calculated and added to the fitted Fe^{2+} and Fe^{3+} contents yielding 82% Fe^{3+} and 18% Fe^{2+}.

for 30 min, using 2 or 3 mm Pt capsules that were iron-presaturated. Starting compositions were mixes of silver oxalate and oxidized Humphrey starting material, and designed to stepwise cover CO_2 concentrations below the saturation point of the melts (Table 2.5).

Two experiments analyzed by Mössbauer spectroscopy (section 2.2.2) were performed at 1500 °C and 2 GPa using original oxidized and reduced starting materials that were set aside before adding CO_2 as silver oxalate. Durations of 30 min and iron-presaturated capsules were used to match saturation experiments. The oxidized experiment, B254, was run in a 4 mm Pt capsule and the reduced experiment, B306, was run in a 2 mm Pt capsule. Experimental glass from B254 was also analyzed for the integrated molar absorptivity regression (Table 2.5 and Fig. 2.2) and used in density determinations (section 2.2.2).

The experimental assembly consisted of $BaCO_3$ sleeves surrounding straight graphite heaters and internal spacers of crushable MgO. Temperatures were measured and controlled using a $W_{97}Re_3$-$W_{75}Re_{25}$ thermocouple placed above the capsule. We applied a pressure correction of -0.2 GPa for this assembly, and attribute P-T uncertainties of ±0.1 GPa and ±12 °C respectively (*Xirouchakis et al.*, 2001). Experiments were quenched by turning off the power to the piston-cylinder. Oxygen fugacities in the experimental assemblies are not known precisely, but

Table 2.3: Experimental conditions and FTIR measured CO_2 concentrations for oxidized Humphrey runs.

Exp. #	T (°C)	P (GPa)	CO_2 (wt%)		H_2O (wt%)	
B247	1500	1.0	0.34	(4)	0.53	(8)
B248	1500	1.5	1.11	(11)	0.75	(8)
B235	1400	2.0	1.60	(7)	0.84	(8)
B249	1425	2.0	1.61	(5)	0.64	(8)
B238	1450	2.0	1.63	(8)	0.62	(8)
B250	1475	2.0	1.59	(6)	0.66	(8)
B237	1500	2.0	1.43	(10)	0.90	(8)
B261	1500	2.0	1.40	(5)	0.71	(8)
B251	1525	2.0	1.29	(5)	0.58	(8)
B236	1550	2.0	1.36	(7)	0.62	(8)
B252	1575	2.0	1.39	(11)	0.69	(8)
B234	1600	2.0	1.37	(10)	0.68	(8)
B253	1625	2.0	1.33	(8)	0.82	(8)
B255	1500	2.5	2.12	(7)	0.93	(8)

Values in parentheses are uncertainties in analyses in terms of least digits cited.

Table 2.4: Experimental conditions and FTIR measured CO_2 concentrations for reduced Humphrey runs.

Exp. #	T (°C)	P (GPa)	CO_2 (wt%)		H_2O (wt%)	
B311	1500	1.0	0.52	(2)	0.50	(8)
B290	1500	1.5	1.00	(4)	0.37	(8)
B284	1400	2.0	1.59	(5)	0.82	(8)
B274	1450	2.0	1.54	(6)	0.72	(8)
B275	1500	2.0	1.42	(8)	0.73	(8)
B282	1550	2.0	1.44	(7)	0.88	(8)
B288	1575	2.0	1.26	(6)	0.36	(8)
B291	1500	2.5	2.01	(10)	0.53	(8)

Values in parentheses are uncertainties in analyses in terms of least digits cited.

Table 2.5: Loaded CO_2 (wt%) and analyzed CO_2 (wt%) compared to integrated absorbance of the area under the CO_3^{2-} doublet at 1430 and 1520 cm^{-1}.

Exp. #	Loaded CO_2 (wt%)	Analyzed CO_2 (wt%)	Integrated Absorbance (cm^{-2})
B254	0.00	0.02	1292
B269	0.95	1.05	59170
B293	1.00	1.14	78367
B260	1.18	1.39	64193
B296	1.25	1.30	73345
B263	1.42	1.44	81132
M508	3.00	2.62	161161

All data are plotted as black squares in Fig. 2.2

Mössbauer analyses of quenched glasses, described below, allow characterization of the oxidation states of Fe prevailing in the liquids from each starting material.

During the experimental study, the original supply of starting material was exhausted and a new batch was mixed from reagents. This material was not used for the solubility experiments, but was employed for a multi-anvil experiment (described below) used to determine the molar absorptivity of carbonate in Humphrey glass. P_2O_5 was added as ammonium-orthophosphate monohydrate [$(NH_4)_2HPO_4$] (98.0%, Alfa Aesar) to an initial mixture of minor elements including MnO, TiO_2, and sanidine powder. This minor-element mixture was ground in a mortar and pestle under ethanol for 45 min, and heated in a Pt crucible for 5 h at 300 °C to remove volatile components. The resulting powder was then mixed with other oxides and mineral powders to achieve the desired composition. CO_2 was added as $CaCO_3$ to create experiments free from Ag metal blobs. This starting material is reduced because iron was added as FeO.

Using this starting material an additional integrated molar absorptivity experiment was performed in a 1000 ton Walker-type multi-anvil press following the procedures, assemblies, and calibrations described and reported in detail by Dasgupta et al. (2004). The capsule used was the same – iron-presaturated, 2 mm Pt – as for piston cylinder experiments. The experiment was performed at 1650 °C and 4.0 GPa with a Re furnace for 30 min (M508 in Table 2.5 and Fig. 2.2).

2.2.2 Analytical methods

Recovered experimental charges were sectioned using a 50 μm diameter tungsten wire saw. One half of the charge was polished for compositional analysis, using diamond lapping films (15-1 μm), while chips of the remaining half were doubly polished to thicknesses less than 30 μm for FTIR analysis.

Experimental glasses were analyzed by wavelength-dispersive spectroscopy using a JEOL JXA8900R electron microprobe. Glass analyses were performed using a 15 kV acceleration voltage, 10 nA beam current, and a partially defocused beam (5 μm). Count times were 20 s for the peak and 10 s for the background for all elements except Na, which was always counted first for 10 s and 5 s on its respective spectrometer. Natural mineral and glass standards were used for calibration.

The CO_2 content of experimental doubly polished glass chips was determined using a Bruker Tensor 37 FTIR spectrometer and Hyperion 2000 microscope. Spectra were recorded over a range of 600-4000 cm^{-1}, averaging 256 scans, and a resolution of 4 cm^{-1}. A KBr beam-splitter was utilized with a mid-IR source, an unpolarized beam, and a square 45 × 45 μm spot. Total dissolved carbon dioxide of experimental charges was determined from the integrated intensity of the CO_3^{2-} ν_3 antisymmetric stretch bands at 1430 and 1520 cm^{-1} and the Beer-Lambert law

$$C_{CO_2} = \frac{44.01 \cdot I}{d\rho\varepsilon^*} \tag{2.6}$$

Here C_{CO_2} is the weight percent of CO_2 dissolved in the glass as CO_3^{2-}, 44.01 is the molecular weight of CO_2 (g mol^{-1}), I is the integrated absorption intensity (cm^{-1}), d is the thickness of the sample (cm), ρ is the density of the glass (g L^{-1}), and ε^* is the integrated molar absorptivity (L mol^{-1} cm^{-2}). The integrated absorption intensity was obtained by subtracting a linear baseline that was fit by least squares minimization to the regions at 1287-1302 cm^{-1} and 1660-1676 cm^{-1}. The glass thickness was measured for each analyzed spot using a WITec alpha300 R microscope outfitted with a 100× Nikon objective lens and a WITec mechanical stage with z-axis resolution of ±0.2 μm. The density of the oxidized synthetic Humphrey glass (3040±50 g L^{-1}) was determined by the sink-float method in methylene iodide-acetone mixtures using magnesite (2970 g L^{-1}) and lawsonite (3090 g L^{-1}) as standards. The reduced Humphrey was

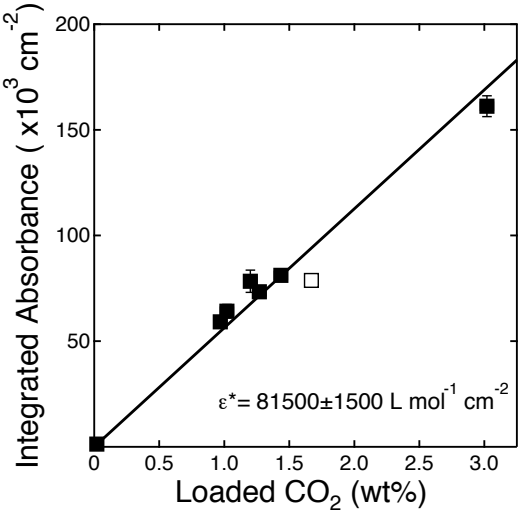

Figure 2.2: Integrated absorbance of dissolved CO_3^{2-} under both the 1430 and 1520 cm^{-1} bands versus loaded CO_2 (wt%) in the experimental capsules. All intensities are normalized to 1 cm sample thickness. The open square is for the experiment (B261), which was not used in the linear regression owing to inferred saturation based on bubbles observed in the experimental charges. Linear regression yields ε^* = 81500±1500 L mol^{-1} cm^{-2} based on a glass density of 3040 g L^{-1}.

not measured, but within uncertainty is not expected to differ from that of oxidized Humphrey based on calculations as a liquid (*Lange and Carmichael*, 1990) or glass (*Fluegel*, 2007).

The integrated molar absorptivity for glassy Humphrey basalt was determined by measuring the integrated intensity under the CO_3^{2-} doublet at 1430 and 1520 cm^{-1} of glasses with known amounts of CO_2 added (Table 2.5). Fig. 2.2 shows the integrated area of this doublet versus loaded CO_2 content. Total CO_2 content is based on amount of silver oxalate or $CaCO_3$ added to the respective starting materials. Intensities increased linearly with gravimetric CO_2 content up to the experiment with 1.65 wt% CO_2 loaded (white square, Fig. 2.2). At this point the data deviate from linearity, indicating that the saturation point of CO_2 of these basalts, at 1500 °C and 2.0 GPa, is between 1.4 and 1.65 wt% CO_2. Further support of this comes from the existence of bubbles in the 1.65 wt% CO_2 experimental glass. The slope given in Fig. 2.2 indicates an integrated molar absorptivity of 81500±1500 L mol^{-1} cm^{-2}. This value is modestly higher than previous studies on terrestrial basalts (e.g. 69500±3000 L mol^{-1} cm^{-2}, *Fine and Stolper*, 1986) and should be applied only to similarly iron-rich basaltic glasses. We note that our calculation of the integrated molar absorptivity assumes that the total CO_2 contents of the glass are accurately known, and that all of the carbon is dissolved as the carbonate anion. However, these

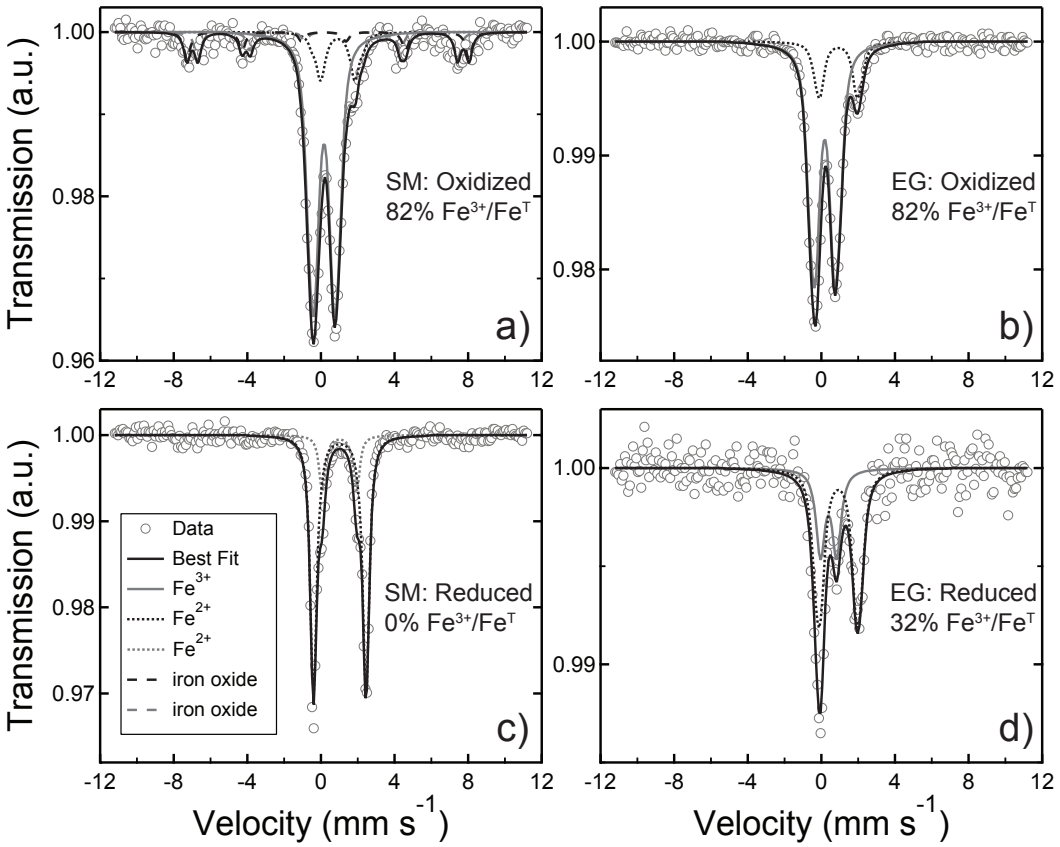

Figure 2.3: Room temperature (300 K) Mössbauer spectra from: a) oxidized starting material (SM) 82% Fe^{3+}/Fe^{T}; b) oxidized experimental glass (EG) 82% Fe^{3+}/Fe^{T}; c) reduced SM 0% Fe^{3+}/Fe^{T}; d) reduced EG 32% Fe^{3+}/Fe^{T}. Also illustrated are the fits to the data using the hyperfine parameters derived by NORMOS program (*Brand*, 1987), as listed in Table 2.2.

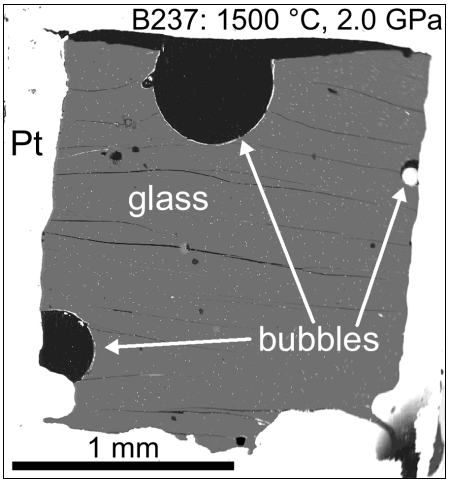

Figure 2.4: Electron backscatter image of experimental run B237 showing glass coexisting with vapor bubbles demonstrating saturation with CO_2 vapor. Bright flecks in glass are Ag metal.

assumptions seem robust owing to the linearity of Fig. 2.2 and to the absence of detectable CO_2 bands in the IR spectra.

The speciation of Fe^{2+} and Fe^{3+} was determined in powders of each starting material, as well as powdered run products of one experiment from each starting material, using Mössbauer spectroscopy. Spectra were acquired at room temperature with a conventional constant-acceleration spectrometer in transmission geometry, with a ^{57}Co/Rh source. Isomer shifts and the velocity scale were calibrated from α-Fe. The Mössbauer spectra were fit using the NORMOS program (*Brand*, 1987) with two doublets using Lorentzian line shapes. Mössbauer spectra are shown in Fig. 2.3 and resulting hyperfine parameters and Fe^{3+}/Fe^{T} determinations listed in Table 2.2.

2.3 Results

Condensed material recovered from saturation experiments consisted almost entirely of glass, but there was minor quench crystallization in experiment B235 conducted at 1400 °C and 2.0 GPa. Additionally, all experiments using silver oxalate as a CO_2 source contain small (0.5-5 μm) finely dispersed crystals of Ag, originating from decomposition of $Ag_2(CO_2)_2$. The glasses coexist with large (10-500 μm) spherical voids inferred to be vapor bubbles present during the experiments. These demonstrate saturation with CO_2 vapor (Fig. 2.4). Major element

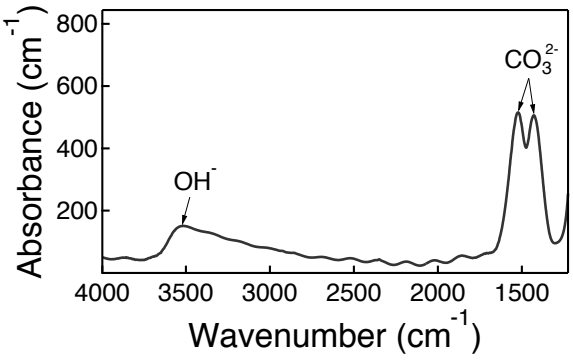

Figure 2.5: Typical FTIR spectrum, normalized to 1 cm, taken on a glass chip from experiment B235 at 2.0 GPa and 1400 °C. The CO_3^{2-} antisymmetric stretch bands are located at 1430 and 1520 cm^{-1}.

compositions of representative experimental glasses, as determined by electron microprobe, are given in Table 2.6. Experiments with Fe-doped capsules yield relative Fe-losses of 0-18%, with greater Fe-losses from those with reduced starting material.

A typical FTIR spectrum from quenched glass is shown in Fig. 2.5. All spectra show strong absorptions characteristic of the CO_3^{2-} bands at 1430 and 1520 cm^{-1} and no evidence of molecular CO_2 at 2350 cm^{-1}. Spectra also have smaller peaks in the region of 3000-3500 cm^{-1}, indicating the presence of OH^- in the melt, with estimated concentrations ranging from 0.36-0.93 wt% (Tables 2.3 and 2.4) using the Jendrzejewski et al. (1996) molar absorption coefficient at the O-H bond fundamental stretching frequency. Owing to the small concentration of dissolved OH^- and the much larger solubility of H_2O compared to CO_2 in basaltic melts (e.g., *Dixon et al.*, 1995), we assume that the vapor coexisting with the melts was effectively pure CO_2. Also, based on the arguments of Brooker et al. (1999) we assume that the CO content of the vapor is too small to have appreciable effect on the CO_2 fugacity, as we did not observe any precipitation of graphite or evidence of dissolved CO in our quenched glasses. Dissolved H_2O is known to enhance CO_2 solubility in silicate melts (e.g., *Mysen et al.*, 1975, 1976; *Behrens et al.*, 2004; *Botcharnikov et al.*, 2006; *Behrens et al.*, 2009), but the small concentrations of H_2O in these experiments should not have significant effect. For example, in the mixed-fluid solubility experiments of Behrens et al. (2009), there is a detectable influence on the relationship between dissolved CO_2 and CO_2 fugacity only for those glasses with >4 wt% H_2O. Dissolved CO_2 and H_2O contents are detailed in Tables 2.3 and 2.4. The CO_2 solubilities measured for synthetic

Table 2.6: Composition (wt%) of representative electron microprobe analyses of experimental glass.

Exp. #	B238	B237	B234	B248	B274	B275	B288	B290
Starting material	Oxidized	Oxidized	Oxidized	Oxidized	Reduced	Reduced	Reduced	Reduced
T(°C)	1450	1500	1600	1500	1450	1500	1575	1500
P (GPa)	2.0	2.0	2.0	1.5	2.0	2.0	2.0	1.5
n[a]	18	20	19	19	19	17	18	19
SiO_2	43.58 (37)	43.44 (28)	44.92 (40)	44.29 (24)	46.39 (28)	46.45 (31)	44.79 (20)	45.83 (20)
TiO_2	0.48 (11)	0.47 (7)	0.52 (8)	0.52 (11)	0.49 (7)	0.56 (10)	0.52 (7)	0.56 (10)
Al_2O_3	9.85 (13)	10.34 (11)	10.62 (16)	10.34 (12)	10.60 (12)	10.58 (8)	10.19 (10)	10.96 (18)
FeO*	19.17 (19)	19.12 (21)	19.01 (24)	19.43 (15)	16.22 (12)	16.58 (13)	17.80 (18)	18.06 (18)
MnO	0.39 (3)	0.37 (4)	0.37 (3)	0.40 (3)	0.38 (3)	0.40 (4)	0.39 (3)	0.38 (3)
MgO	9.92 (9)	10.14 (7)	10.45 (15)	10.16 (9)	10.46 (8)	10.46 (8)	10.12 (9)	10.61 (11)
CaO	7.73 (9)	7.97 (12)	7.51 (9)	8.01 (11)	8.18 (7)	8.12 (9)	7.95 (10)	7.84 (8)
Na_2O	2.36 (10)	2.44 (8)	2.28 (12)	2.47 (11)	2.50 (8)	2.51 (11)	2.43 (8)	2.43 (11)
K_2O	0.09 (1)	0.09 (2)	0.13 (2)	0.10 (1)	0.10 (1)	0.11 (1)	0.13 (2)	0.13 (2)
P_2O_5	0.49 (5)	0.47 (5)	0.52 (7)	0.49 (7)	0.51 (6)	0.52 (8)	0.52 (4)	0.54 (6)
Ag	1.17 (23)	1.38 (16)	1.27 (19)	1.27 (18)	0.49 (6)	0.59 (4)	1.24 (20)	0.66 (8)
Total	95.22	96.25	97.61	97.47	96.34	96.87	96.08	97.99
Mg#	47.98	48.60	49.49	48.24	53.48	52.93	50.33	51.15
Fe^{3+}/Fe^{T}	82	82	82	82	32	32	32	32

[a] – Number of electron microprobe analyses. Values in parentheses are standard deviations of analyses in terms of least digits cited.
Fe^{3+}/Fe^{T} is from Mössbauer data in Table 2.2 and listed under similarly oxidized and reduced experiments.
Mg# = 100 × (molar MgO/(MgO+FeO))

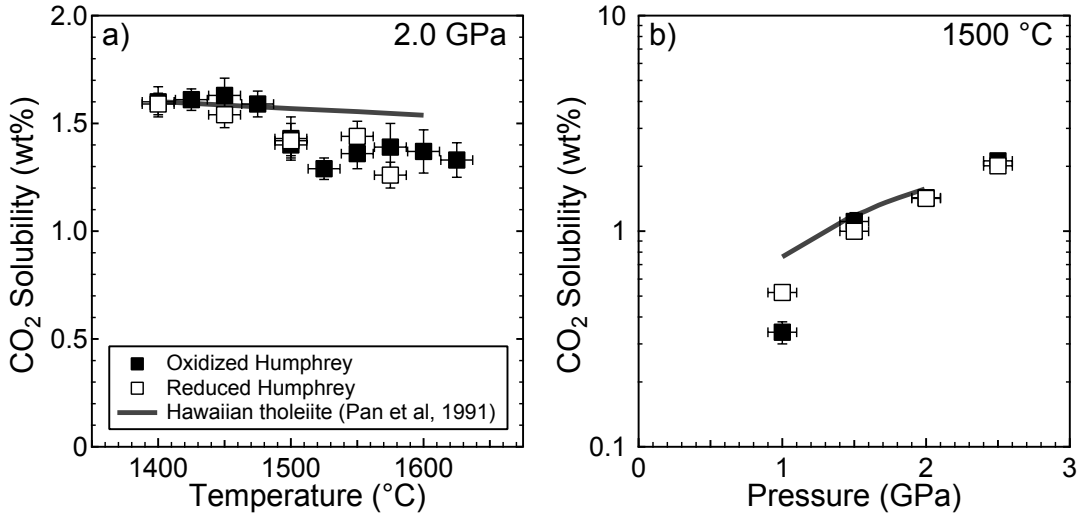

Figure 2.6: a) Plot of CO_2 solubility versus temperature at 2.0 GPa for experimental Humphrey basalt (black squares – oxidized starting material Pt-Fe doped capsule; white squares – reduced starting material Pt-Fe doped capsule) and model of Hawaiian tholeiite from (*Pan et al.*, 1991, gray line); the 1400 and 1500 °C oxidized and reduced Humphrey data points are overlapping; b) Plot of CO_2 solubility versus pressure at 1500 °C; the 2.0 GPa oxidized and reduced Humphrey data points are overlapping (symbols same as Fig. 2.6a).

martian Humphrey basalt range from 0.34-2.12 wt% (Fig. 2.6). Solubilities increase with increasing pressure and decrease with increasing temperature, as has been documented for many other natural and synthetic silicate melts (*Blank and Brooker*, 1994).

Mössbauer spectra are shown in Fig. 2.3 and fitted hyperfine parameters and Fe^{3+}/Fe^{T} determinations listed in Table 2.2. The oxidized and reduced starting materials have 82% and 0% Fe^{3+}/Fe^{T}. The post-experimental glasses are more similar to one another, but remain distinct, with the more oxidized and reduced glasses having 82% and 32% Fe^{3+}/Fe^{T}. Although the liquids have markedly different ratios of ferric and ferrous iron, their CO_2 solubilities are similar (black and white squares, respectively, in Fig. 2.6), meaning that the iron oxidation state has little effect on CO_2 solubility.

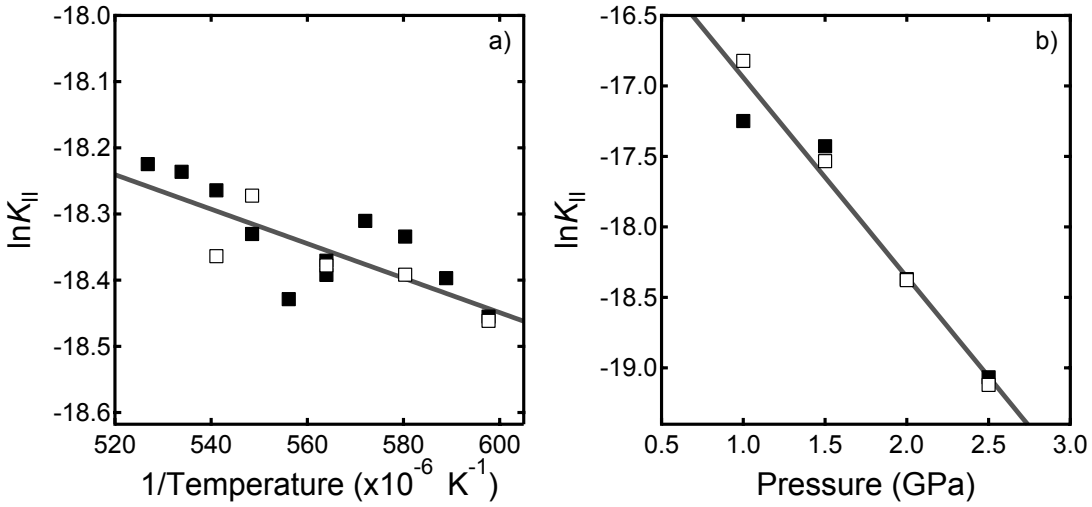

Figure 2.7: Experimentally determined values of $\ln K_{\mathrm{II}}$ (Eqn. 2.7) versus a) inverse temperature and b) pressure of oxidized and reduced experimental run products (symbols same as Fig. 2.6a). Linear regression of the experimental data allows determination of $\ln K^{\mathrm{o}}_{\mathrm{II}}$, ΔV^{o}, and ΔH^{o}. Results are listed in Table 2.7.

2.4 Thermodynamic parameterization

A principal goal of this study is to obtain a parameterization for the equilibrium constant K_{II} (Eqn. 2.2), as this allows calculation of the concentration of dissolved carbonate in graphite-saturated martian basalt (Eqn. 2.5). Consequently, we use our experimentally-determined CO_2 solubilities to calibrate the thermodynamic relationship

$$\ln K_{\mathrm{II}} = \ln K^{\mathrm{o}}_{\mathrm{II}} - \left(\frac{\Delta V^{\mathrm{o}}}{\mathrm{R}T}\right)(P - P^{\mathrm{o}}) - \left(\frac{\Delta H^{\mathrm{o}}}{\mathrm{R}}\right)\left(\frac{1}{T} - \frac{1}{T^{\mathrm{o}}}\right) \tag{2.7}$$

(*Stolper and Holloway*, 1988), where $K^{\mathrm{o}}_{\mathrm{II}}$ is the equilibrium constant at a reference temperature and pressure, P^{o} and T^{o}, taken to be 100 MPa and 1473 K, respectively, and ΔV^{o}, and ΔH^{o} are the volume and enthalpy changes associated with the dissolution reaction (Eqn. 2.1) and are assumed to be independent of temperature and pressure. Calculation of K_{II} from the experimental data requires conversion of solubilities measured in wt%, $C_{\mathrm{CO_2}}$, to mole fractions:

Table 2.7: Experimentally determined model parameters for CO_2 solubility in different melt compositions.

	$\ln K_{II}^{o}$ (P^o, T^o)		ΔV^o (cm^3 mol^{-1})		ΔH^o (kJ mol^{-1})	
Tholeiite[1]	-14.83	(10)	23.14	(103)	5.20	(430)
Basanite[2]	-14.32		21.72	(127)	-13.1	(139)
Leucitite[3]	-13.36		21.53	(42)	-28.15	(424)
Martian basalt[4]	-15.42	(20)	20.85	(91)	-17.96	(1020)

Values in parentheses are uncertainties in analyses in terms of least digits cited. No errors are listed when not available in literature. P^o=100 MPa and T^o=1473 K for all studies. Data from [1]Pan et al. (1991), [2]Holloway and Blank (1994), [3]Thibault and Holloway (1994), and [4]this study.

$$C_{CO_2} = \left[\frac{44.01 \cdot X_{CO_3^{2-}}^{melt}}{44.01 \cdot X_{CO_3^{2-}}^{melt} + \left(1 - X_{CO_3^{2-}}^{melt}\right) FW_{one}} \right] \tag{2.8}$$

where FW_{one} is the one-oxygen formula weight for 1 mol of volatile-free synthetic Humphrey melt, 37.96 g mol^{-1}, calculated from oxide molar units, and 44.01 is the molecular weight of CO_2 (g mol^{-1}). Linear regression of the experimental data (Fig. 2.7) results in the values of $\ln K_{II}^{o}$, ΔV^o, and ΔH^o specified in Table 2.7, which also lists previously calibrated values applicable to other basaltic compositions. This parameterization of K_{II}, combined with calculation of K_I after Holloway et al. (1992), allows us to apply Eqn. 2.5 to calculate concentrations of CO_2 in graphite-saturated magma of the composition of Humphrey basalt as a function of pressure, temperature, and oxygen fugacity (Fig. 2.8). As previously discussed by Holloway (1998) and Hirschmann and Withers (2008), dissolved CO_2 in graphite-saturated magmas increase with increasing temperature and decrease with increasing pressure.

2.5 Applications and discussion

2.5.1 Effect of iron oxidation state on CO_2 solubility, the solubility-NBO/T correlation, and extrapolation to primitive magmas

Another principal focus of this study is the influence of oxygen fugacity on the solubility of CO_2 in graphite-saturated martian magmas, owing to the correspondence between oxygen and CO_2

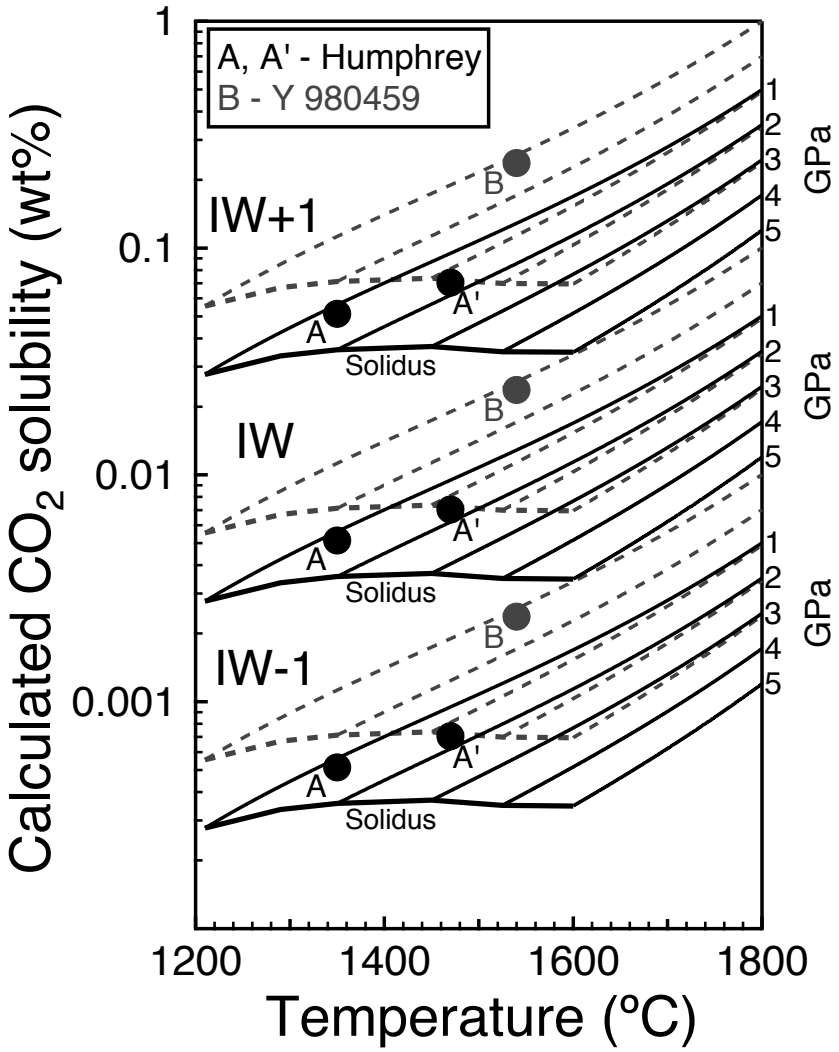

Figure 2.8: Calculated CO_2 solubility versus temperature for graphite-saturated synthetic Humphrey basalt at oxygen fugacities equal to IW-1, IW, and IW+1. Points marked A, A, and B are possible melting conditions discussed in the text: A is based on the source region of Humphrey basalt (1350 °C, 1.2 GPa, see text), A is based on the inferred source region of the Humphrey parental magma (1470 °C, 1.7 GPa, see text, *Filiberto and Dasgupta*, 2011), and B is based on the source regions of primitive shergottite Y 980459 (1540 °C, 1.2 GPa, *Musselwhite et al.*, 2006) and assuming that the CO_2 solubility in Y 980459 is twice that of Humphrey (see text). For each oxygen fugacity, CO_2 solubilities are calculated as a function of temperature for 1, 2, 3, 4, and 5 GPa (solid lines – CO_2 solubilities for points A, A; dashed lines – CO_2 solubilities for point B). Location of the martian mantle solidus is shown (*Bertka and Holloway*, 1994; *Agee and Draper*, 2004).

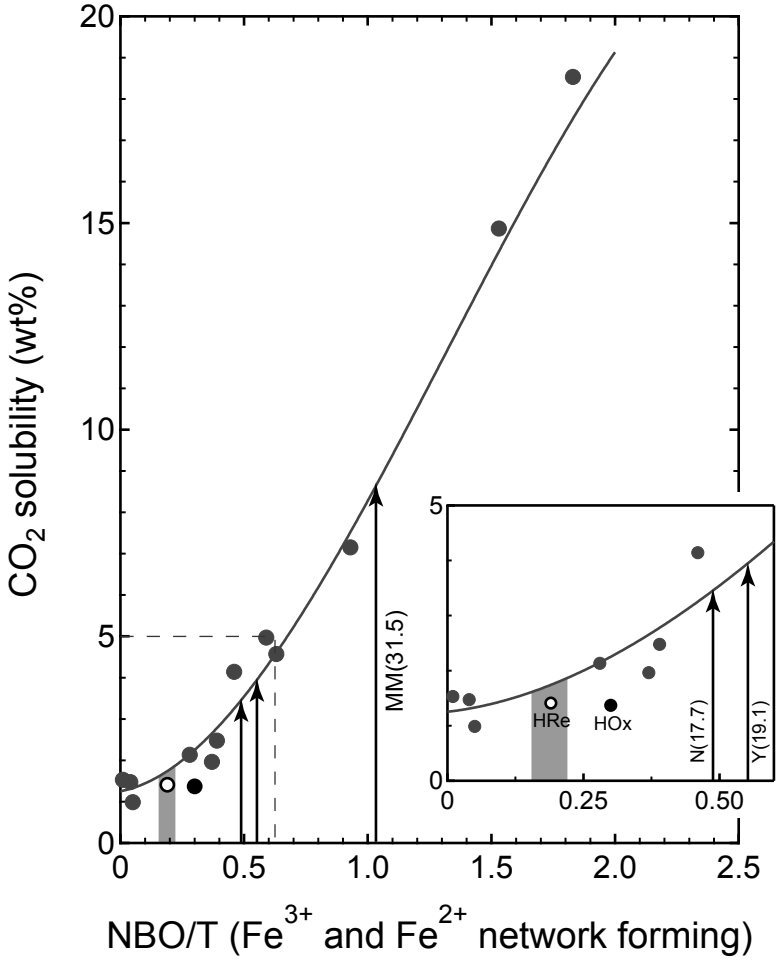

Figure 2.9: A plot of 2.0 GPa CO_2 experimental solubilities from this study and from the literature vs. NBO/T calculated with both Fe^{3+} and Fe^{2+} acting as network formers. The plot is modified after that of Brooker et al. (2001a) and NBO/T ratios are calculated using their method. Solid curve is the best fit trend from Brooker et al. (2001a). Numbers in parentheses are MgO concentrations (wt%) for all samples >12 wt% MgO. Data and abbreviations are: this study, HOx = Humphrey oxidized starting material; HRe = Humphrey reduced starting material; Gross et al. (2011), N = NWA 5789 composition, normalized, and Cr_2O_3 and NiO free; Musselwhite et al. (2006), Y = Y 980459 composition, normalized, and Cr_2O_3, NiO, and FeS free; Bertka and Fei (1997), MM = bulk martian mantle. Gray circles are solubilities from experiments on compositions compiled by Brooker et al. (2001a). CO_2 solubility for N, Y, and MM are estimated from the parameterization best fit curve from Brooker et al. (2001a). Dashed line indicates field enlarged for inset. Solid gray field represents the calculated CO_2 solubility range for the following martian basalts: Fastball (*Squyres et al.*, 2007); Adirondack and Mazatzal (*McSween et al.*, 2006a); and Backstay, Irvine, Wishstone, and Champagne (*McSween et al.*, 2006b).

fugacities (Eqn. 2.5). However, the experiments on Fe-rich basalt also constrain a potential secondary influence of oxygen fugacity on CO_2 solubility owing to variations in ferric and ferrous iron, and therefore help illuminate the relationship between CO_2 solubility and melt structure. Brooker et al. (2001a) argued that CO_2 solubility in silicate melts is unaffected by the valance state of Fe, but this inference came from somewhat indirect evidence. They observed strong correlation between CO_2 solubility and the ratio of non-bridging oxygens to tetrahedral cations (NBO/T, *Mysen et al.*, 1985) from a wide variety of natural and synthetic melt compositions (Fig. 2.9) that held only when they assumed that Fe^{2+} and Fe^{3+} are both network-forming cations, a supposition that is consistent with spectroscopic studies indicating significant tetrahedral Fe^{2+} in aluminosilicate glasses and melts (*Jackson et al.*, 2005; *Mysen*, 2006). Experiments on oxidized and reduced Humphrey support this contention, as otherwise similar Fe-rich melts with greatly different Fe^{3+}/Fe^{2+} ratios have nearly identical solubilities (Tables 2.3 and 2.4; Fig. 2.6). Also, as shown in Fig. 2.9, both oxidized and reduced melts have solubilities close to the NBO/T correlation defined by Brooker et al. (2001a).

The NBO/T-CO_2 solubility correlation discovered by Brooker et al. (2001a) may be of great utility to understanding CO_2 outgassing from terrestrial planets as it allows prediction of CO_2 solubilities for melt compositions that have not yet been or cannot be measured experimentally. For example, the NBO/T ratios of several representative martian compositions are plotted in Fig. 2.9 using the Brooker et al. (2001a) trend. Included are a range of compositions encompassing Fastball and six Gusev basalts (solid gray field in Fig. 2.9, *McSween et al.*, 2006a,b; *Squyres et al.*, 2007), the composition of the primitive shergottites NWA 5789 and Y 980459, inferred to be near-primary martian liquids (*Musselwhite et al.*, 2006; *Usui et al.*, 2008; *Filiberto and Dasgupta*, 2011; *Gross et al.*, 2011), and the bulk martian mantle composition from Bertka and Fei (1997). Y 980459 may be an appropriate analog for the composition of high temperature magmatism associated with early martian crust formation. The similarity in NBO/T for Humphrey basalt (HRe and HOx in Fig. 2.9) to other martian compositions indicates that the experimentally determined CO_2 solubility may be representative of typical martian basalts. The higher NBO/T ratios of NWA 5789, Y 980459, and the bulk martian mantle suggest that these melts should have greater CO_2 solubilities. Thus, at a similar temperature, pressure and oxygen fugacity, the CO_2 solubility of a liquid with the composition of Y 980459 could be about twice as great as Humphrey and that of an early martian magma ocean may be a factor of 4 greater.

2.5.2 Application to graphite-saturated melts in the martian mantle

The solubility of CO_2 determined for the martian basalt, Humphrey, is similar, though not identical, to those documented in terrestrial basalts (e.g., *Pan et al.*, 1991, gray line in Fig. 2.6). The comparison with CO_2 solubility in Hawaiian tholeiite determined by Pan et al. (1991) is particularly relevant, as the Hawaiian tholeiite served, for lack of a better analog, as the basis for Hirschmann and Withers (2008) modeling CO_2 solubility of martian basalts. Thus, the overall similarities in solubility between Humphrey and the Hawaiian tholeiite yield broad verification that the models constructed by Hirschmann and Withers (2008) are relevant to Mars.

Application of the solubility model derived from experiments on Humphrey basalt to magmatic CO_2 outgassing on Mars requires appropriate estimates of temperatures and pressures in magmatic source regions. Partial melting of planetary mantles occurs over ranges of temperature and pressure, but here we select characteristic conditions of plausible source regions of two different martian basalts, Humphrey and Y 980459, to illustrate the effects of these variables on CO_2 solubility.

The conditions of melt generation of Humphrey are constrained in part by inverse experiments conducted by Monders et al. (2007) and Filiberto et al. (2008). Monders et al. (2007) found saturation in olivine and orthopyroxene at 1.2 GPa and 1325 °C for a hydrous (0.8 wt% H_2O) liquid. Filiberto et al. (2008) found saturation in olivine and pigeonite at 1.25 GPa and 1375 °C in a more nearly anhydrous liquid, and concluded that the primary source must have been somewhat more primitive than Humphrey, and therefore somewhat hotter than 1375 °C. The concentration of H_2O in primary martian magmas is uncertain and so we take the Humphrey source region to be near 1350±50 °C and 1.2±0.1 GPa. For these conditions, graphite-saturated melts from source regions similar to that of Humphrey have CO_2 solubilities of 5.1 ppm at IW-1, 51 ppm at IW, and 510 ppm at IW+1 (point A in Fig. 2.8). In our calculations, the parameterized IW buffer is from O'Neill (1988) with a pressure term from Huebner (1971).

Recently Filiberto and Dasgupta (2011) argued that primary martian basalts are more primitive than the composition investigated here and derive from hotter conditions at greater pressure. They estimate that the magma parental to Humphrey had >13 wt% MgO and originated at 1470 °C and 1.7 GPa. Slightly higher solubilities (7, 70, and 700 ppm at IW-1, IW and IW+1, point A in Fig. 2.8) would result for the conditions of the Humphrey parental magma inferred by Filiberto and Dasgupta (2011), but we emphasize that the difference in composition between Humphrey and its putative parent magma would likely affect the actual solubilities.

The primitive SNC meteorite Y 980459 has been interpreted as a near-primary liquid (*Musselwhite et al.*, 2006; *Usui et al.*, 2008) and Musselwhite et al. (2006) found that this composition is multiply saturated in olivine and orthopyroxene with compositions plausibly similar to the martian mantle at 1540 °C and 1.2 GPa. Some studies have explored the possibility that Y 980459 was derived from a hydrous source, in which case source temperatures could be from 50 to 200 °C lower than the anhydrous multiple saturation temperature (*Dalton et al.*, 2007; *Draper*, 2007). Yet, for illustrative purposes we will assume the effects of higher temperature on possible CO_2 outgassing. As noted above, the CO_2 solubility of Y 980459 is predicted to be twice that of Humphrey at 1500 °C and 2 GPa. If we assume that the temperature and pressure dependence of solubility of the two basalts are similar, we can then estimate potential degassing from source regions of very primitive martian basalt. Corresponding compositions for the source region of Y 980459 are 24 ppm at IW-1, 240 ppm at IW, and 0.24 wt% at IW+1 (point B in Fig. 2.8).

2.5.3 Influence of volcanogenic CO_2 on martian climate

If a thick CO_2-rich atmosphere was chiefly responsible for the equable late Noachian martian climate recorded by fluvial and lacustrine geomorphic features and sediments (e.g., *Pollack et al.*, 1987; *Craddock and Maxwell*, 1993; *Mangold et al.*, 2004; *Squyres et al.*, 2004; *Fassett and Head*, 2008; *di Achille et al.*, 2009; *Dehouck et al.*, 2010; *di Achille and Hynek*, 2010), then CO_2 partial pressures must amount to approximately 2 bars (*Pepin*, 1994; *Carr*, 1999; *Manning et al.*, 2006). Using appropriate solubilities of CO_2 in martian basalts, the volcanogenic contribution of CO_2 to the martian atmosphere may be calculated from the cumulative igneous flux model of Hirschmann and Withers (2008).

The parameterization of Hirschmann and Withers (2008) considers the time-integrated accumulation of volcanogenic CO_2 into the martian atmosphere and does not quantify the rates of CO_2 removal by processes such as weathering or loss to space (e.g., *Manning et al.*, 2006; *Gillmann et al.*, 2011). Over the history of Mars, such processes have likely removed much of the CO_2 from the early martian atmosphere, resulting in the comparatively thin (6 mbars) CO_2 pressure today. If substantial CO_2 draw-down occurred during the Noachian, then accumulation of a thick volcanogenic CO_2 greenhouse by the end of the Noachian must be commensurately greater.

Additionally, the magmatic flux parameterization of Hirschmann and Withers (2008) assumes that all extrusive and intrusive volumes degassed completely. It has been suggested that significant fractions of juvenile mantle-derived CO_2 may be trapped in the crust along with intrusive rocks, rather than degassed to the surface (e.g., *O'Neill et al.*, 2007; *Craddock and Greeley*, 2009; *Righter et al.*, 2009). In our view, this type of storage is likely in part temporary, as CO_2 delivered to the crust may be remobilized by crustal magmatism or metamorphism. If any such crustal storage is effectively permanent, then our estimates of total magmatic CO_2 degassing are maxima.

If typical martian basaltic magmatism were similar to that of the basalts at Gusev crater (1350 °C and 1.2 GPa), then the cumulative volcanogenic CO_2 output on Mars since 4.5 Ga could have generated no more than 0.03 and 0.26 bars from sources at IW and IW+1 respectively (solid black lines in Fig. 2.10). Only if such sources were as oxidized as IW+1.9 could the total volcanogenic flux produce an atmosphere with 2 bars CO_2 pressure. Therefore, application of the new experimental results provide qualified support for the contention of Hirschmann and Withers (2008) that volcanogenic degassing cannot account for the mass of CO_2 required to generate a strong greenhouse early in martian history. This conclusion applies if typical martian magmatism since 4.5 Ga has consisted chiefly of normal martian basalts similar to those sampled at Gusev Crater or from most SNC meteorites and if conditions in those basalt source regions were characteristically reduced (i.e., similar to IW+1 or lower). However, a quite different conclusion may be justified if typical martian magmatism was more primitive and hotter.

Volcanogenic fluxes for basalts similar to Y 980459 should be greater than those of Gusev crater owing to the greater intrinsic solubility of CO_2 in this more depolymerized magma as well as the higher temperatures of their sources. If magmas similar to Y 980459 have CO_2 solubility twice as great as measured for Humphrey (Fig. 2.9), the total integrated volcanogenic flux from a source appropriate for Y 980459 (1540 °C and 1.2 GPa) amounts to 0.12 and 1.2 bars at IW and IW+1 respectively (dashed gray lines, Fig. 2.10). Approaching 2 bars of CO_2 pressure would require only slightly more oxidized conditions, amounting to IW+1.2. Thus, if typical martian volcanic activity has been primitive and hot, a strong volcanogenic CO_2 greenhouse is plausible.

Based on simulations of convection and melting in the martian mantle, Musselwhite et al. (2006) and Jellinek et al. (2008) concluded that conditions appropriate for the petrogenesis of Y 980459 have been exceptional rather than typical of post-4.5 Ga martian magmatism. On

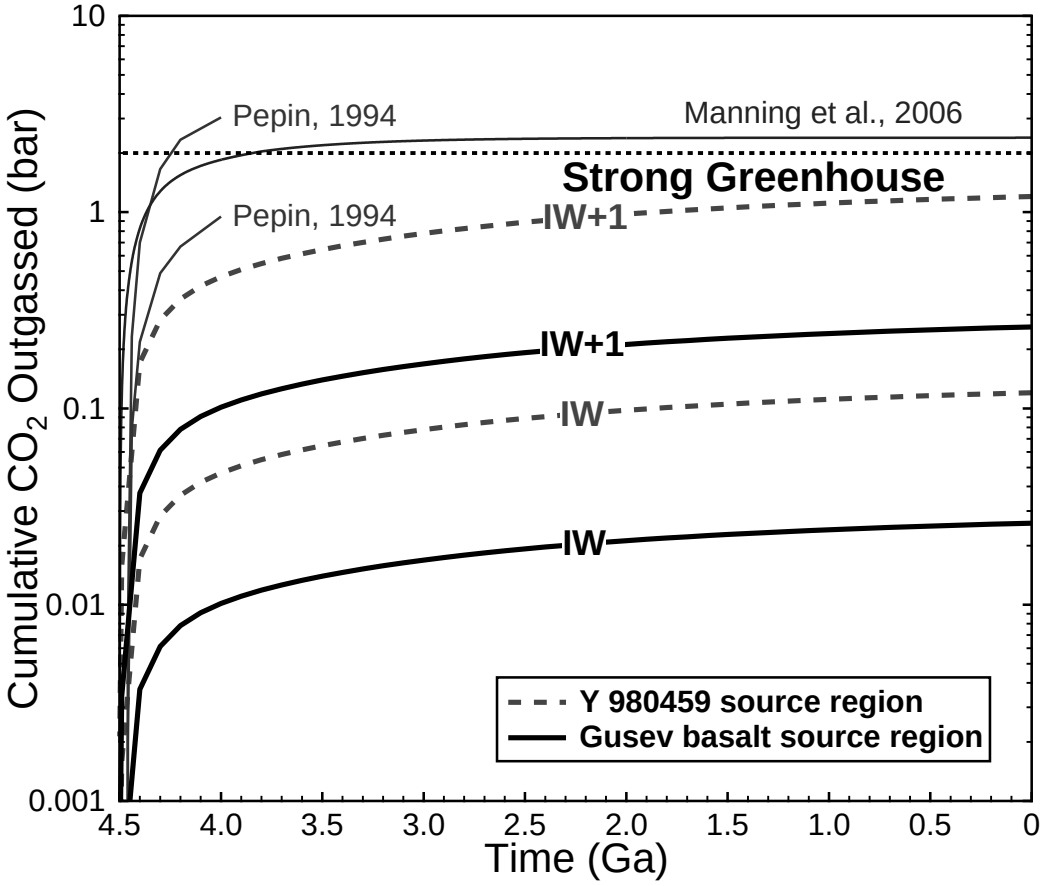

Figure 2.10: Total volcanic outgassing of CO_2 calculated for Mars from 4.5 Ga to the present. Cumulative CO_2 outgassed combine the magmatic production model of Hirschmann and Withers (2008) and mean CO_2 solubility in partial melts for the source regions of Gusev basalt (bold black lines, *Filiberto et al.*, 2008) based on experimental determinations of this study and Y 980459 (dashed gray lines, *Musselwhite et al.*, 2006) (based on assumed enhanced solubility, see text) at oxygen fugacities corresponding to IW and IW+1. The calculation assumes that magmas are formed under graphite-saturated conditions, that the dissolved carbonate concentrations are those calculated in Fig. 2.8, and that the martian crust has a mean density of 3040 kg m^{-3}. The line labeled Strong Greenhouse indicates a martian atmosphere of 2 bars, thought to be thick enough to stabilize liquid water. Data from: Pepin (1994), Manning et al. (2006).

the other hand, about half of the magmatic flux since 4.5 Ga occurred at Tharsis in the late Noachian (*Greeley and Schneid*, 1991; *Phillips et al.*, 2001), nearly contemporaneously with the era of most likely equable climate. As Tharsis is widely interpreted to be the product of a hot plume (*Phillips et al.*, 2001; *Baker et al.*, 2007; *Dohm et al.*, 2007; *Jellinek et al.*, 2008), it would not be surprising if mean eruption temperatures there were more similar to that found for Y 980459 than to Gusev basalts, which are Hesperian or Early Amazonian (*McSween et al.*, 2006a), and not associated with a major thermal anomaly. Thus, we consider the possibility that Tharsis magmatism produced a significant CO_2 greenhouse to be intriguing. Much rests with the actual solubility of CO_2 in magmas like Y 980459, which presently is based on extrapolation (Fig. 2.9) but can be tested experimentally, and on the oxidation state of Tharsis magmatism, which is poorly constrained.

2.5.4 Other greenhouse gases?

If the supply of CO_2 is insufficient to create a strong greenhouse early in martian history, then other atmospheric gases may instead have been partly responsible. Other volatiles that have been considered include SO_2 and CH_4 (*Brown and Kasting*, 1993; *Squyres and Kasting*, 1994; *Fairèn et al.*, 2004; *Bullock and Moore*, 2007; *Halevy et al.*, 2007). Until recently these proposals were motivated by the lack of detection of massive carbonates (e.g., *Bullock and Moore*, 2007; *Chevrier et al.*, 2007) that would be present under a CO_2-rich atmosphere with liquid water stable on the surface (*Schaefer*, 1993). Evidence from several groups (*Ehlmann et al.*, 2008; *Boynton et al.*, 2009; *Palomba et al.*, 2009; *Michalski and Niles*, 2010; *Morris et al.*, 2010) has shown that there are carbonates previously undiscovered on Mars, though it remains unclear whether the mass of these carbonates is sufficient to account for a substantial early CO_2 greenhouse.

Mars has been described as a S-rich planet with the detection of massive sulfate deposits (e.g., *Gendrin et al.*, 2005; *Langevin et al.*, 2005), observation of high S contents in shergottites (e.g., *Zipfel et al.*, 2000; *Shirai and Ebihara*, 2004), and the suggestion of a significant amount of S in the core (e.g., *Stewart et al.*, 2007). Recent models have suggested that S-species could constitute an important additional greenhouse component on early Mars (*Halevy et al.*, 2007; *Johnson et al.*, 2008; *Craddock and Greeley*, 2009) and experimental evidence from Righter et al. (2009) shows that martian magmas are capable of degassing enough SO_2 to balance the observed sedimentary deposits (e.g., *Gendrin et al.*, 2005; *Langevin et al.*, 2005). Though its

importance as a greenhouse gas may be reduced by a short lifetime in the martian atmosphere (Johnson et al., 2009) and evidence that volcanogenic SO_2 might not be capable of maintaining a strong greenhouse effect due to the formation of sulfur and sulfate aerosols causing a net cooling effect over long time scales (*Tian et al.*, 2010).

As a strong greenhouse gas, methane may plausibly influence the martian climate (*Squyres and Kasting*, 1994; *Kasting*, 1997). Recently, groups using Earth-based satellites (*Krasnopolsky et al.*, 2004; *Mumma et al.*, 2009) and Mars Express (*Formisano et al.*, 2004; *Geminale et al.*, 2008) have reported strongly localized detection of CH_4 in the martian atmosphere, though the detection of CH_4 is still debated (*Zahnle et al.*, 2011). The presence of CH_4 would be unexpected because its lifetime in the martian atmosphere (~340 yr, *Krasnopolsky et al.*, 2004) relative to the global mixing time (0.5 yr, *Krasnopolsky et al.*, 2004) requires the CH_4 be recently produced and highly localized.

Appreciable volcanogenic methane is likely only under reducing conditions (*Kadik et al.*, 2006). Terrestrial basalt source regions are generally too oxidized, and therefore emissions from volcanoes such as Mauna Loa have no detectable CH_4 (*Ryan et al.*, 2006). Previous experimental studies of CH_4 solubility in silicate melts have shown no detectable CH_4 dissolved in the melts (*Eggler and Baker*, 1982; *Taylor and Green*, 1987). Though recent studies have found measurable concentrations of methane under reduced conditions (*Kadik et al.*, 2006; *Mysen et al.*, 2009; *Kadik et al.*, 2010; *Mysen and Yamashita*, 2010; *Ardia et al.*, 2011) , they do not show good agreement regarding absolute concentrations nor do they provide well-constrained predictions regarding the dependence on oxygen fugacity or melt composition. Additional studies are required to determine if CH_4 can be dissolved in Fe-rich magmas under conditions appropriate for petrogenesis of martian basalts.

Depending on the source regions and magma compositions used to model magmatic flux over time, the evidence for stable liquid water on the ancient martian surface may not require a strong greenhouse dominated by CO_2. The influences of other volcanogenic volatiles merit further examination.

2.5.5 Graphite buffering of a reduced martian mantle

Our analysis emphasizes the extraction of CO_2 from graphite-saturated martian basalt source regions for which a key constraint, along with primary liquid composition, temperature, and pressure, is the oxygen fugacities of mantle sources at the point of melt extraction. These are,

presumably, similar to those recorded by the magmas themselves and so our analysis does not depend on how the f_{O_2} of a given source evolved prior to melt extraction.

A more general question is variation of oxygen fugacity in the martian mantle, including possible variations associated with dynamic processes of upwelling and partial melting. So long as graphite remains in the residue, the ratio of f_{O_2} and f_{CO_2} fugacities is fixed by Eqn. 2.4, but for vapor-undersaturated conditions, neither f_{O_2} nor f_{CO_2} are likely to remain constant during partial melting. Rather, f_{O_2} and f_{CO_2} should evolve, in large part owing to changes in f_{O_2} driven by differential extraction of Fe^{2+} and Fe^{3+} from the residue (*Holloway*, 1998). If Fe^{3+} is significantly less compatible in residual minerals than Fe^{2+}, as is generally assumed, and if the principal dissolved carbonaceous species is CO_2 or CO_3^{2-}, partial melt extraction should produce a more reduced source (e.g., *Holloway*, 1998). On the other hand, under very reducing conditions, other possibilities are plausible. For example, if dissolved CH_4 is an important melt species (*Mysen et al.*, 2009) and if Fe^{3+} is partially retained in residual spinel and pyroxene, melt extraction could lead to source oxidation.

Righter et al. (2008) argued that the large range of oxygen fugacities observed for SNC meteorites is an endogeneous result of polybaric decompression melting, with more oxidized small-degree melts producing the nakhlites and more reduced high degree partial melts the depleted shergottites. Strong variations in radiogenic isotopic and trace element enrichments among shergottites (e.g., *Herd*, 2003) preclude such a cogenetic relationship among many of the SNCs, but for those that plausibly derive from a common source, more reduced f_{O_2} may indeed accompany progressive melt extraction. Righter et al. (2008) reasoned that f_{O_2} variations would arise from graphite buffering of magmas with constant activity of CO_2. In fact, unless accompanied by fluid saturation, constant activity of CO_2 during progressive partial melting of graphite-saturated melting is unlikely (*Holloway*, 1998). Rather, a trend of reduction with melt depletion could result from diminishing Fe^{3+}/Fe^{T} in the source.

2.6 Conclusions

Basalt generation on Mars likely occurs in a reduced, graphite-saturated mantle. The presence of graphite constrains the CO_2 solubility in martian magmas with respect to oxygen fugacity. For cool, reduced conditions, the experimentally-determined solubility of typical Gusev Crater basalt shows that the martian mantle is incapable of degassing sufficient CO_2 to sustain

a thick greenhouse atmosphere in the late Noachian. For such conditions, models of martian atmospheric evolution considering only the greenhouse effects of CO_2 should be reexamined and additional volatiles such as SO_2 and CH_4 should be considered. However, hotter, more primitive magmas favor greater CO_2 solubility and if volcanic activity at Tharsis during the late Noachian was dominated by high potential temperature, and slightly oxidized (IW+1.2) sources, then a strong volcanogenic greenhouse is plausible.

Chapter 3

CO_2 solubility in primitive martian basalts similar to Yamato 980459, the effect of composition on CO_2 solubility of basalts, and the evolution of the martian atmosphere

This chapter has been accepted to American Mineralogist with co-authors Douglas R. Schaub and Marc M. Hirschmann, and is used in this dissertation with permission from the Mineralogical Society of America.

3.1 Introduction

Evidence for standing liquid water on the martian surface during the late Noachian and early Hesperian epochs (e.g., *Irwin et al.*, 2005; *Fassett and Head*, 2008; *di Achille and Hynek*, 2010; *Grant et al.*, 2011) strongly suggests a thick greenhouse atmosphere not evident on Mars today (*Pollack et al.*, 1987; *Pepin*, 1994). Yet there remains considerable uncertainty as to how this greenhouse was created and maintained, and how it evolved to the current thin, modern

atmosphere. Early studies assumed that this greenhouse was composed chiefly of CO_2 and sustained by significant volcanic outgassing (e.g., *Pollack et al.*, 1987; *Pepin*, 1994; *Carr*, 1999), but the plausibility of sufficient volcanogenic CO_2 fluxes has been questioned (e.g., *Kasting*, 1997; *Hirschmann and Withers*, 2008; *Grott et al.*, 2011; *Stanley et al.*, 2011), in part owing to a relative dearth of substantial layered carbonate deposits that would be the expected record of a thick CO_2 atmosphere (*Schaefer*, 1993; *Bullock and Moore*, 2007; *Chevrier et al.*, 2007). Further, alternative greenhouse environments involving SO_2 and CH_4 have been proposed (*Brown and Kasting*, 1993; *Squyres and Kasting*, 1994; *Fairèn et al.*, 2004; *Bullock and Moore*, 2007; *Chevrier et al.*, 2007; *Halevy et al.*, 2007; *Gaillard and Scaillet*, 2009; *Righter et al.*, 2009).

The volcanogenic supply of volatiles is an important input and key limit to martian atmospheric evolution (*Gillmann et al.*, 2011). Understanding this flux requires constraints on the cumulative magmatic flux to the martian surface and on CO_2 solubilities in primary martian basalts. The time integrated magmatic flux through martian history, though subject to considerable uncertainties, has been estimated from photogeology (*Greeley and Schneid*, 1991; *Jakosky and Shock*, 1998; *Craddock and Greeley*, 2009) and from models of heatflow through time (*Carr*, 1999; *Manning et al.*, 2006; *O'Neill et al.*, 2007), and has been parameterized by Hirschmann and Withers (2008).

A key constraint on the likely CO_2 fluxes accompanying martian magmatic output is that much of the martian mantle is thought to be sufficiently reduced (*Hale et al.*, 1999; *Wadhwa*, 2001; *Herd et al.*, 2002; *Herd*, 2003; *Shearer et al.*, 2006; *Karner et al.*, 2007; *Righter et al.*, 2008) such that carbon resides principally as graphite (*Hirschmann and Withers*, 2008; *Righter et al.*, 2008). The solubility of carbon as carbonate in silicate melts is controlled by the prevailing fugacity of CO_2 (f_{CO_2}) according to the reaction

$$\underset{\text{gas}}{CO_2} + \underset{\text{melt}}{O^{2-}} \rightleftharpoons \underset{\text{melt}}{CO_3^{2-}} \tag{3.1}$$

which has an equilibrium constant given by

$$K_{\text{II}} = \frac{X^{\text{melt}}_{CO_3^{2-}}}{\left(X^{\text{melt}}_{O^{2-}}\right) f_{CO_2}} \tag{3.2}$$

where $X^{melt}_{O^{2-}} = 1 - X^{melt}_{CO_3^{2-}}$(*Holloway et al.*, 1992; *Holloway*, 1998). The value of K_{II} must be calibrated from experimental determinations of CO_2 solubility on a melt of appropriate composition. For graphite-saturated magmas, f_{CO_2} is related to oxygen fugacity (f_{O_2}) by the reaction:

$$\underset{\text{graphite}}{C} + \underset{\text{gas}}{O_2} \rightleftharpoons \underset{\text{gas}}{CO_2} \tag{3.3}$$

which is described by the equilibrium constant

$$K_I = \frac{f_{CO_2}}{f_{O_2}} \tag{3.4}$$

and which can be calculated from basic thermodynamic data for graphite and CO_2 vapor (e.g., *Holloway et al.*, 1992). For graphite-saturated magmas, combining Eqns. 3.2 and 3.4 allows calculation of the mole fraction of dissolved carbonate

$$X^{melt}_{CO_3^{2-}} = \frac{K_I K_{II} f_{O_2}}{1 + K_I K_{II} f_{O_2}}. \tag{3.5}$$

This simple relationship between CO_2 solubility and oxygen fugacity shows that an order of magnitude increase in oxygen fugacity changes the amount of CO_2 dissolved in the melt by one order of magnitude (*Hirschmann and Withers*, 2008).

Stanley et al. (2011) determined experimentally the solubility of CO_2 as a function of temperature and pressure for a synthetic liquid similar to the Humphrey basalt analyzed at Gusev Crater by the Spirit Rover (*McSween et al.*, 2006a). Using resulting values of K_{II}, they showed that the cumulative magmatic flux on Mars, derived from a reduced, graphite-saturated martian mantle, could not degas sufficient CO_2 to support strong greenhouse conditions in the late Noachian or early Hesperian.

The models presented by Stanley et al. (2011) are predicated on the assumption that the CO_2 concentrations in martian magmatism through time can be approximated by measurements made on one Gusev Crater basalt. Recognizing this limitation, Stanley et al. (2011) considered the possibility that other eruptive compositions could have enhanced CO_2 solubility and thereby could be associated with more massive CO_2 fluxes. In particular, one may consider whether the magmatism associated with emplacement of the giant Tharsis volcanic complex may have been

distinctly more CO_2-enriched. Tharsis represents half of all martian igneous activity since the stabilization of the ancient primordial martian crust and the majority was emplaced during the late Noachian (*Phillips et al.*, 2001; *Williams et al.*, 2008), coincident with geologic evidence for a warm moist climate (e.g., *Phillips et al.*, 2001; *Irwin et al.*, 2005; *Fassett and Head*, 2008; *di Achille and Hynek*, 2010; *Grant et al.*, 2011), though volumetrically subordinate resurfacing continued into the Amazonian (*Williams et al.*, 2008). Geologic and geodynamic considerations suggest that Tharsis was the product of a hot mantle plume (*Kiefer*, 2003), and the combination of higher temperature and the primitive associated magmas may have enhanced CO_2 solubility (*Stanley et al.*, 2011).

The high-MgO olivine-phyric shergottite Y 980459 may be a plausible analog for high temperature Tharsis magmatism. In the present collection of martian meteorites, Y 980459 is unique, having the highest MgO content among shergottites (18.9 wt%, *Musselwhite et al.*, 2006) and deriving from the hottest source region, 1540±10 °C (*Musselwhite et al.*, 2006) or 1452±12 °C (*Blinova and Herd*, 2009). Further, inverse experiments suggest that Y 980459 is a near-primary partial melt of the martian mantle (*Musselwhite et al.*, 2006; *Usui et al.*, 2008; *Blinova and Herd*, 2009; *Filiberto and Dasgupta*, 2011). These features compare well with the compositions of magmas expected for the putative Tharsis plume, which may have had a mantle potential temperature of 1532 °C (*Kiefer*, 2003). Stanley et al. (2011) speculated that the CO_2 solubility of this more depolymerized melt may be enhanced, in part based on the empirical correlation between CO_2 solubility and melt polymerization gauged from NBO/T (non-bridging oxygens/tetrahedral cations, *Brooker et al.*, 2001a). Note that Y 980459 is too young (472±47 Ma; *Shih et al.*, 2005) to be derived from Noachian Tharsis magmatism, but it is the best analog among available martian compositions.

The principal aim of this study is to investigate experimentally whether a primitive martian basalt such as Y 980459 has a high CO_2 solubility, and therefore to determine if hot plume volcanism at Tharsis may have vented sufficient CO_2 to support a thick greenhouse in the late Noachian and early Hesperian epochs. Secondarily, the work explores the relationship between carbonate solubility and composition of non-alkalic basalts such as those found on Mars.

Table 3.1: Compositions (wt%) of experimental glass compared to Y 980459, Humphrey martian basalt, and Hawaiian tholeiite.

	Humphrey	Y 980459		Hawaiian tholeiite
Oxide	McSween et al. (2006a)	Musselwhite et al. (2006)	Experimental glass (B382)	Pan et al. (1991)
SiO_2	46.49	49.63	51.59	49.54
TiO_2	0.59	0.51	0.49	2.30
Al_2O_3	10.55	5.70	6.12	13.43
FeO*	18.95	16.75	14.31	10.54
MnO	0.43	0.48	0.45	0.00
MgO	10.82	19.08	18.80	10.49
CaO	8.26	6.87	7.23	11.02
Na_2O	2.38	0.65	0.65	2.17
K_2O	0.09	0.02	0.02	0.51
P_2O_5	0.60	0.30	0.34	0.00
Total	100.00	100.00	100.00	100.00
Mg#	50.44	67.01	70.09	63.95

FeO* = total iron (Fe_2O_3+FeO). Mg# = 100 x (molar MgO/(MgO +FeO). McSween et al. (2006a) is calculated Cr-free. Musselwhite et al. (2006) is calculated Cr- and FeS-free. Hawaiian tholeiite is the starting material with CO_2 added as silver oxalate from Pan et al. (1991).

3.2 Methods

The starting material consisted of a synthetic mixture similar in composition to the primitive shergottite Y 980459 (*Musselwhite et al.*, 2006) (Table 3.1) plus 5 wt% CO_2, and was synthesized from reagent grade oxides and carbonates. The CO_2 was added as $CaCO_3$, Na_2CO_3, and K_2CO_3. P_2O_5 was added as ammonium-ortho-phosphate monohydrate [$(NH_4)_2HPO_4$] (98.0%, Alfa Aesar) to an initial mixture of minor elements including MnO, TiO_2, and K_2CO_3. This minor-element mixture was ground in a mortar and pestle under ethanol for 45 min, and heated in a platinum crucible for 5 h at 300 °C. This heating devolatilized the ammonium-orthophosphate monohydrate but not the K_2CO_3 (decomposition temperature is 898 °C). The resulting minor-element powder was then mixed with major oxides (SiO_2, Al_2O_3, MgO, and FeO) and carbonates ($CaCO_3$ and Na_2CO_3) to achieve the desired composition.

Experiments were performed in 2 mm sealed platinum capsules that were Fe-presaturated

to inhibit Fe-loss from the starting material during the experiment. Presaturation was accomplished by melting powdered basalt in the capsules in a gas-mixing furnace for 24 h at 1250 °C and a CO-CO_2 atmosphere adjusted to an oxygen fugacity of approximately QFM-4. These conditions were chosen to ensure that the iron in the glass was chiefly divalent and that it alloyed with the platinum capsule in large amounts. The basaltic glass was then removed by immersion in a bath of warm hydrofluoric (HF) acid for 2-3 days. Two batches of capsules were made; one was presaturated with a MORB composition (*Aubaud et al.*, 2004), while the other was presaturated with the synthetic Y 980459 starting material. The presaturation material did not influence appreciably Fe-loss during the experiments (relative Fe loss of 12-19% using MORB and 10-15% using Y 980459; Table 3.2).

Experiments were conducted for 30 min at pressures of 1.0-2.0 GPa and temperatures of 1600-1650 °C following the procedures and assemblies detailed by Stanley et al. (2011). We applied a pressure correction of -0.2 GPa for this assembly, and attribute *P-T* uncertainties of ±0.1 GPa and ±12 °C respectively (*Xirouchakis et al.*, 2001). The narrow range of temperatures was constrained by the high liquidus temperature of Y 980459 and the low melting point of the FePt alloy capsules. Conditions for individual experiments are listed in Table 3.3.

Recovered experimental charges were sectioned using a 50 μm diameter tungsten wire saw. One half of the charge was polished for compositional analysis, using 15-1 μm diamond lapping films, while chips of the remaining half were doubly polished to thicknesses between 20 and 80 μm for infrared analysis. Methods used for compositional analysis by electron microprobe and volatile analysis by Fourier transform infrared spectroscopy (FTIR) are reported in detail by Stanley et al. (2011). The density of Y 980459 was not measured; instead we applied the measured value of Humphrey from Stanley et al. (2011, 3040±50 kg m^{-3}). The density of Y 980459 glass is expected to be within error of that for Humphrey based on calculations as a liquid (2760 and 2760 g L^{-1} respectively; *Lange and Carmichael*, 1990) and similar when calculated as a glass (3090 and 3170 g L^{-1} respectively; *Fluegel*, 2007).

We applied the integrated molar absorptivity, ε^*=81500±1500 L mol^{-1} cm^{-2}, for glassy Humphrey basalt that was determined by Stanley et al. (2011). This absorption coefficient is modestly higher than those determined from studies on terrestrial basalts (e.g., 69500±3000 L mol^{-1} cm^{-2}, *Fine and Stolper*, 1986) and should be applied only to similarly Fe-rich basaltic glasses. Dixon and Pan (1995) derived an empirical relationship between linear molar absorptivity (ε) and Na/(Na+Ca) in mafic silicate glasses. Their model predicts significantly different

Table 3.2: Electron microprobe (EMP) analyses (wt%) of experimental glasses.

Exp. #	B387	B400	B385	B399	B382	B390	A874	B392	B393	B384
T(°C)	1600	1625	1600	1625	1600	1600	1625	1625	1650	1650
P (GPa)	1.0	1.0	1.5	1.5	2.0	2.0	2.0	2.0	2.0	2.0
n[a]	15	15	27	15	20	20	16	20	14	14
SiO_2	50.86	49.58	51.32	50.30	51.59	50.43	51.69	51.52	50.88	52.00
TiO_2	0.53	0.52	0.54	0.53	0.49	0.51	0.46	0.50	0.53	0.46
Al_2O_3	5.87	6.09	5.98	5.93	6.12	5.83	5.99	5.77	5.86	6.03
FeO*	14.68	14.68	13.54	14.87	14.31	15.04	14.44	14.45	14.56	14.20
MnO	0.44	0.47	0.46	0.46	0.45	0.46	0.43	0.47	0.44	0.44
MgO	19.59	20.37	20.08	19.79	18.80	19.49	19.00	19.03	19.66	18.78
CaO	6.94	7.24	7.01	7.05	7.23	7.30	7.04	7.29	7.02	7.12
Na_2O	0.73	0.70	0.71	0.71	0.65	0.62	0.65	0.66	0.68	0.63
K_2O	0.02	0.02	0.02	0.02	0.02	0.02	0.02	0.02	0.02	0.03
P_2O_5	0.33	0.33	0.34	0.34	0.34	0.30	0.28	0.29	0.33	0.32
Normalized	100.00	100.00	100.00	100.00	100.00	100.00	100.00	100.00	100.00	100.00
EMP total	100.34[c]	99.42[c]	99.98[c]	100.03[c]	98.20	97.19	98.76	97.13	98.82[c]	97.63
Fe-loss[b]	12.37	12.36	19.15	11.23	14.59	10.21	13.80	13.73	13.06	15.23
Pt dopant	MORB	Y98	MORB	Y98	MORB	Y98	MORB	Y98	Y98	Y98

[a] – Number of electron microprobe analyses. [b] – Fe-loss (%) relative to starting material (16.75 wt% FeO). [c] – These glasses were analyzed in a later session with new software and show a slight elevation in EMP totals due to differences between software ZAF corrections.

Table 3.3: Experimental conditions, FTIR measured CO_2 and H_2O concentrations, imposed CO_2 fugacities, and resulting values of equilibrium constant K_{II} (Eqn. 3.2).

Exp. #	T	P	CO_2		H_2O		$\ln f_{CO_2}$	$\ln K_{II}$
	(°C)	(GPa)	(wt%)		(wt%)		(kbar)	
B387	1600	1.0	0.45	(3)	0.56	(8)	11.33	-16.88
B400	1625	1.0	0.48	(2)	1.17	(8)	11.31	-16.79
B385	1600	1.5	0.89	(3)	0.22	(8)	12.66	-17.52
B399	1625	1.5	0.71	(2)	0.64	(8)	12.63	-17.71
B382	1600	2.0	1.17	(6)	0.60	(8)	13.82	-18.40
B390	1600	2.0	1.24	(3)	0.94	(8)	13.82	-18.34
A874	1625	2.0	1.26	(5)	0.66	(8)	13.77	-18.28
B392	1625	2.0	1.14	(3)	1.11	(8)	13.77	-18.38
B393	1650	2.0	1.20	(5)	1.11	(8)	13.73	-18.29
B384	1650	2.0	1.15	(4)	0.72	(8)	13.73	-18.33

Values in parentheses are uncertainties in analyses in terms of least digits cited. $\ln f_{CO_2}$ calculated according to Sterner and Pitzer (1994)

values for Humphrey and Y 980459, 331 and 403 L mol^{-1}cm^{-1} respectively. Yet, this method has proven unable to reproduce CO_2 absorbtivities in a range of glass compositions (*Jakobsson*, 1997; *Behrens et al.*, 2004; *Botcharnikov et al.*, 2006; *Behrens et al.*, 2009), causing us to question whether Na/(Na+Ca) is a robust predictor of CO_2 extinction coefficients.

3.3 Results

Experimental products consisted almost entirely of glass with minor quench crystallization only in the 1600 °C experiments conducted at 2.0 GPa. All glasses quenched with large (10-500 μm) spherical voids inferred to have been vapor bubbles during the experiments. Electron microprobe analyses of major element composition of all glasses are given in Table 3.2. Despite using Fe-doped capsules, experiments yielded relative Fe-losses of 10-19% (Table 3.2).

A typical FTIR spectrum is shown in Fig. 3.1. All spectra show strong absorption characteristics of the bands at 1430 and 1520 cm^{-1} and no evidence of molecular CO_2 at 2350 cm^{-1}. Spectra also have smaller peaks in the region of 3000-3500 cm^{-1}, indicating the presence of OH^- in the melt, with concentrations ranging from 0.22-1.17 wt% (Table 3.3) using the Jendrzejewski et al. (1996) molar absorption coefficient at the O-H bond fundamental stretching frequency. As discussed in Stanley et al. (2011), owing to the small concentration of dissolved

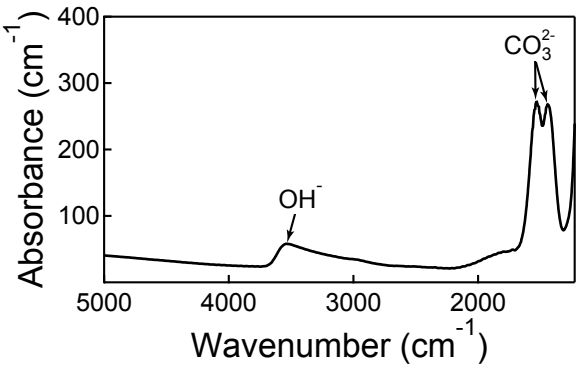

Figure 3.1: Typical FTIR spectrum, normalized to 1 cm, from glass from experiment B399 at 1.5 GPa and 1625 °C. The antisymmetric stretch bands are located at 1430 and 1520 cm^{-1}, and the OH^- stretch band is located at 3550 cm^{-1}.

OH^- and the much larger solubility of H_2O compared to CO_2 in basaltic melts (e.g., *Dixon et al.*, 1995), we assume that the vapor coexisting with the melts was effectively pure CO_2 and that the small concentrations of H_2O in these experiments should not have significant effect on the solubility of CO_2. We did not observe any precipitation of graphite or spectroscopic evidence of dissolved CO (peak located near 2150 cm^{-1}, *Brooker et al.*, 1999) in our quenched glasses, so we assume that the CO content of the vapor is too small to have appreciable effect on the CO_2 fugacity, based on the arguments of Brooker et al. (1999). Dissolved CO_2 contents measured for synthetic martian Y 980549 basalt range from 0.45-1.26 wt% (Table 3.3 and Fig. 3.2). Solubilities increase with increasing pressure and decrease with increasing temperature, as has been documented for many other natural and synthetic silicate melts (*Moore*, 2008, and references therein).

3.4 Applications and discussion

3.4.1 Effect of composition on solubility of primitive mafic magmas

A key question is the influence of major element composition on the CO_2 solubility of mafic and ultramafic magmas. It is well known that CO_2 solubility is significantly enhanced in Ca- or alkali-rich magmatic compositions (*Thibault and Holloway*, 1994; *Dixon*, 1997; *Brooker et al.*, 2001a; *Botcharnikov et al.*, 2005; *Behrens et al.*, 2009). This is attributable to the abundance in these depolymerized liquids of non-bridging oxygens associated with Ca and alkalis, which

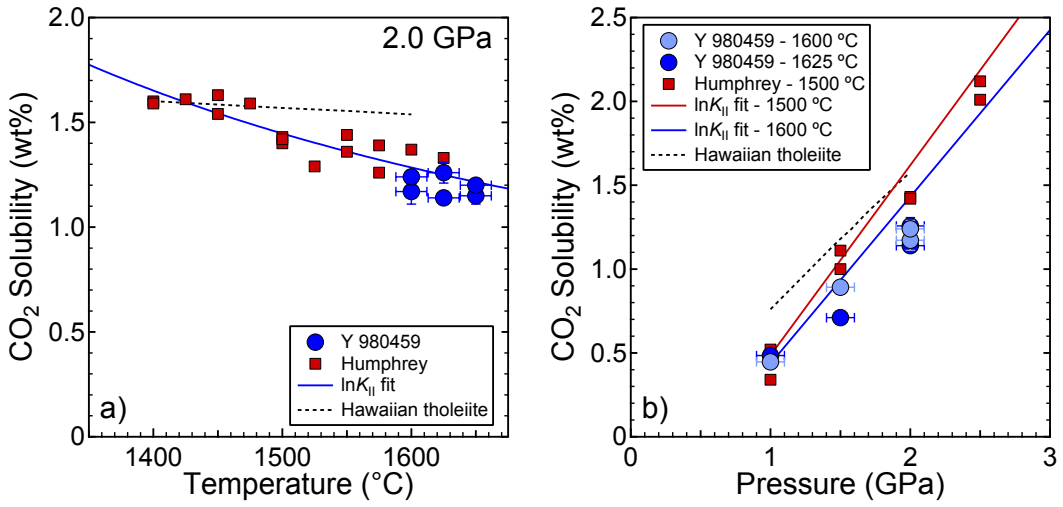

Figure 3.2: Experimentally-determined CO_2 solubility versus temperature at 2.0 GPa for synthetic martian basalts: Y 980459 (blue circles, this study) and Humphrey (red squares; *Stanley et al.*, 2011). b) Variation of CO_2 solubility versus pressure for Y 980459 at 1600 °C (light blue circles) and 1625 °C (blue circles), and Humphrey at 1500 °C (red squares; *Stanley et al.*, 2011). The lnK_{II} fit curves (blue for 2 GPa in Fig. 3.2a; red for 1500 °C and blue for 1600 °C in Fig. 3.2b) are calculated from the fit of both experimental CO_2 solubility datasets to Eqn. 3.6; the parameters used in this calculation are listed in the text. The solubility of CO_2 in Hawaiian tholeiite (*Pan et al.*, 1991, dashed line shown on both panels) is comparable in magnitude, though not identical, to those of martian basalts.

provide favorable bonding environments for carbonate ions (e.g., *Guillot and Sator*, 2011). Less well understood is how solubility is influenced by variations in ferromagnesian components in tholeiitic compositions, including basalts, picrites, komatiites and peridotitic liquids. One might expect that large variations in FeO* and MgO in such liquids could affect the availability of non-bridging oxygens and hence the CO_2 solubility. For example, compared to Hawaiian tholeiite (*Pan et al.*, 1991), both Humphrey and Y 980459 have considerably more FeO* (10 vs. 19 and 17 wt% respectively) and Y 980459 has much more MgO (19 wt%) than either Humphrey (11 wt%) or Hawaiian tholeiite (10 wt%) (Table 3.1). Yet, these tholeiitic basalts all have similar CO_2 solubilities (Fig. 3.2).

The small influence of FeO* and MgO concentrations on CO_2 solubility must be related to their structural role in aluminosilicate melts. On the basis of correlations between CO_2 solubility and NBO/T, Brooker et al. (2001a) argued that in silicate melts ferrous iron is a network-forming cation and that therefore FeO* has a subordinate influence on CO_2 solubility. Stanley

et al. (2011) found support for this interpretation owing to very similar CO_2 solubilities in Humphrey basalt with high and low Fe^{3+}/Fe^{2+} ratios. Similarly, Brooker et al. (2001a) noted that Mg-rich melts have lower CO_2 solubility than would be anticipated from their NBO/T calculated in a traditional manner and suggested that Mg also may act as a network-former in silicate melts. The present results for Y 980459 are consistent with this interpretation. Thus, the similarity in CO_2 solubility in basalts across large variations in FeO* and MgO could be a consequence of polymerization of these cations in silicate melts.

Clues to the bonding environment of carbonate anions can be derived from the structure of the infrared carbonate absorption peak (e.g., *Fine and Stolper*, 1985; *Brooker et al.*, 2001b). In particular, the splitting, $\Delta\nu_3$, of the ν_3 doublet near 1450 cm^{-1} is related to the symmetry of the carbonate ion and therefore provides information on the structural environment of the ion in the silicate glass. Characteristic FTIR spectra of the martian basalts are shown in Fig. 3.3, where they are compared to those for andesite, Mg-melilitite, and Mg-nephelinite (*Brooker et al.*, 2001b), and Hawaiian tholeiite (*Pan et al.*, 1991).

For the martian basalts, the average mid-points for the ν_3 doublets are 1475.8±0.7 cm^{-1} (n=22) and 1483.8±1.2 cm^{-1} (n=10) for Humphrey and Y 980459, respectively, and are similar to the range previously observed from natural samples, 1460-1475 cm^{-1} (*Brooker et al.*, 2001b). The $\Delta\nu_3$ splittings for Humphrey and Y 980459 are similar to each other (93.3±2.9 cm^{-1} and 88.3±3.0 cm^{-1} respectively; 2σ uncertainties) and to that observed for Hawaiian tholeiite (95 cm^{-1}). Peak splittings of this magnitude are generally observed for carbonate ions bonded to non-bridging oxygens and tend to increase with the degree of polymerization, i.e., $\Delta\nu_3$ = 77 cm^{-1} for Mg-melilitite and 105 cm^{-1} for andesite (*Brooker et al.*, 2001b) (Fig. 3.3). In contrast, larger splittings (>200 cm^{-1}) are associated with highly distorted network carbonates (T-carb-T) in which two of the oxygens are shared with the network-forming tetrahedra (*Fine and Stolper*, 1985). Thus, the splittings for martian and terrestrial tholeiitic basalts are intermediate for common depolymerized compositions and are consistent with carbonate associated solely with non-bridging oxygens.

Recent molecular dynamics simulations by Guillot and Sator (2011) suggest that carbonate has a high affinity for NBO associated with Mg^{2+} and Fe^{2+}. These simulations show similar CO_2 solubilities for tholeiitic basalt and for Mg-rich kimberlite at 2 GPa, indicating that high Mg and Fe abundances do not enhance solubility significantly, as originally suggested by

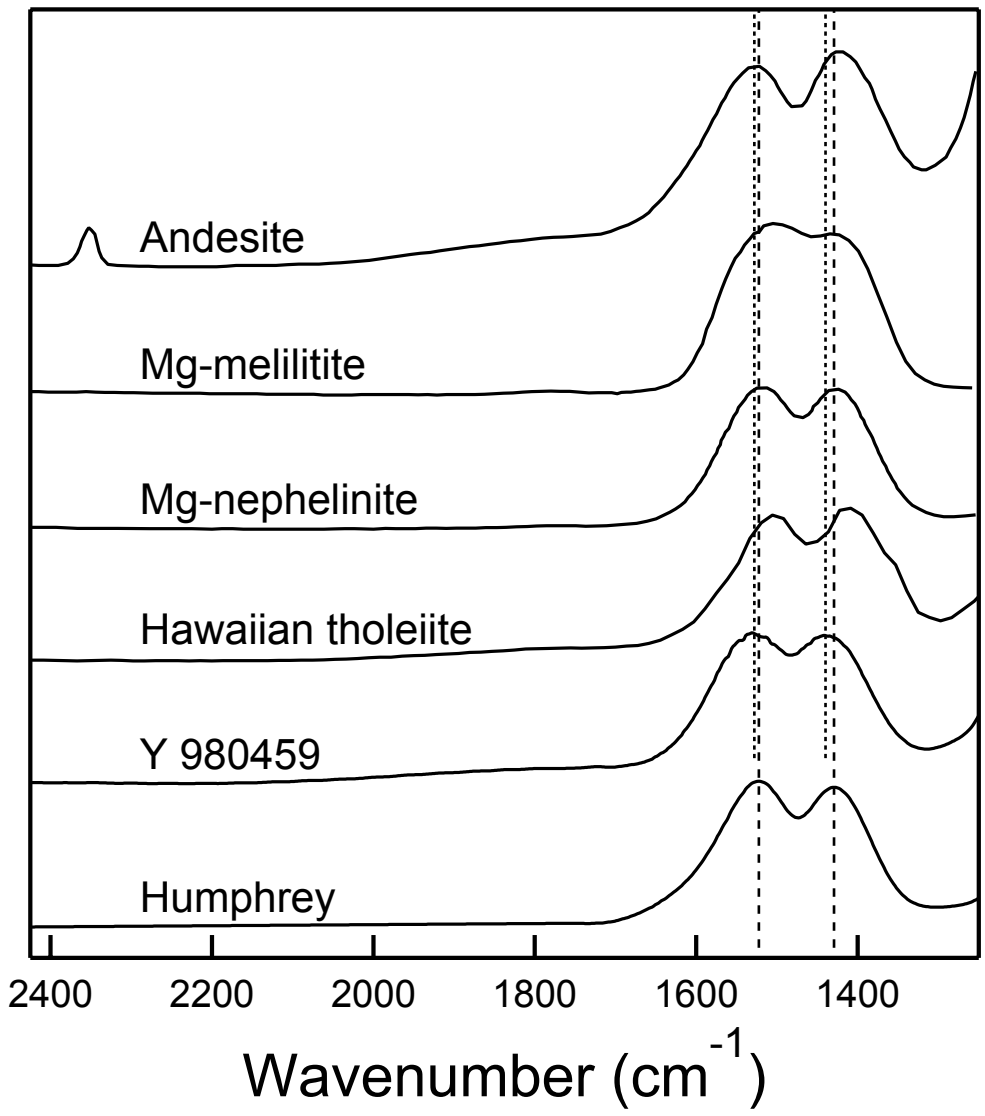

Figure 3.3: FTIR spectra for Y 980459 and Humphrey (*Stanley et al.*, 2011) compared to mafic CO_2-bearing glasses showing similar splitting and position of the carbonate doublet in a variety of natural spectra despite compositional differences. The spectra are scaled to similar heights to aid in visual comparison. Dotted lines have been drawn through the carbonate doublet peaks of both basalts from this study to show the similarity in splitting and position. Molecular CO_2 appears in addition to carbonate at 2350 cm^{-1} only for the more polymerized andesite. Andesite, Mg-melilitite, and Mg-nephelinite spectra are from Brooker et al. (2001b). Hawaiian tholeiite spectrum is from Pan et al (1991).

Brooker et al. (2001a; 2001b). Parenthetically, experiments suggest that the simulations exaggerate the similarity, as the CO_2 solubility in the kimberlite is >5 wt% at 2 GPa (*Brey et al.*, 1991), about 3 times greater than in tholeiitic basalt. If NBO associated with Mg^{2+} and Fe^{2+} are favorable environments for bonding with carbonate anions, but CO_2 solubility is not enhanced in Mg- and Fe-rich melts, then presumably increased Mg^{2+} and Fe^{2+} do not produce substantially more NBO in silicate melts.

Spectroscopic and molecular dynamical simulations indicate that Mg is both a network-forming and network-modifying cation, with the number of oxygens coordinated around Mg^{2+} ions in silicate and aluminosilicate melts or glasses equal to 4, 5, or 6 (*Guillot and Sator*, 2007; *Adjaoud et al.*, 2008; *de Koker et al.*, 2008; *Guignard and Cormier*, 2008; *Shimoda et al.*, 2008; *Wilding et al.*, 2008; *Trcera et al.*, 2009; *Wilding et al.*, 2010; *Cormier and Cuello*, 2011). In natural melts at low pressure, Mg has a mean coordination of 5 (*Guillot and Sator*, 2007; *Vuilleumier et al.*, 2009). This complex structural role of Mg apparently results in a modest effect on CO_2 solubility. Non-bridging oxygens associated with network-modifying Mg may enhance solubility of carbonate in silicate melts, at least when present in very high concentrations, as in the case of kimberlite (36 wt% MgO; 5 wt% CO_2 at 2 GPa and 1650 °C; *Brey et al.*, 1991), but not as substantial as the NBO associated with high-coordinated Ca, Na, and K.

The relative insensitivity of carbonate solubility to the concentrations of mafic components in tholeiitic basaltic melts may provide clues regarding CO_2 solubility in komatiites and peridotitic melts. Carbonate solubility in such ultramafic liquids is of particular interest for understanding CO_2 degassing from magma oceans early in the history of Mars or Earth (e.g., *Kuramoto and Matsui*, 1996; *Elkins-Tanton*, 2008; *Hirschmann and Withers*, 2008; *Hirschmann*, 2012). However, solubility measurements are not available and may not be feasible for these liquids as they resist quenching to glass from high-pressure experiments. Conventional measures of NBO/T (e.g., *Mysen et al.*, 1985) as well as direct measurements of liquid viscosities (e.g., *Liebske et al.*, 2005) indicate that ultramafic natural liquids are highly depolymerized, and this led Stanley et al. (2011) to postulate that the CO_2 solubility of such liquids could be enhanced by a factor of four relative to that of tholeiitic basalt. This would lead to greater retention of C in magma oceans relative to overlying atmospheres. However, the experimental results on Y 980459, as well as the considerations reviewed above regarding the influence of Mg on melt structure and CO_2 solubility, suggest that enhanced solubility in peridotitic and komatiitic

liquids may be modest. Low CaO and alkalis in peridotitic and komatiitic liquids may actually limit CO_2 solubility compared to typical basalts.

3.4.2 Application to graphite-saturated melts in the martian mantle

The similarity in CO_2 solubility between Y 980459 and Humphrey, despite significant compositional differences, suggests that major element variations among martian basalts do not have great influence on their capacity to contribute carbon to the atmosphere and that a single solubility law may be applicable to an even wider spectrum of martian basalts. Therefore, we calibrated a function suitable for martian basalts based on the equilibrium constant K_{II} (Eqn. 3.2):

$$\ln K_{\mathrm{II}} = \ln K_{\mathrm{II}}^{\mathrm{o}} - \left(\frac{\Delta V^{\mathrm{o}}}{\mathrm{R}T}\right)(P-P^{\mathrm{o}}) - \left(\frac{\Delta H^{\mathrm{o}}}{\mathrm{R}}\right)\left(\frac{1}{T} - \frac{1}{T^{\mathrm{o}}}\right) \tag{3.6}$$

(*Stolper and Holloway*, 1988), where $K_{\mathrm{II}}^{\mathrm{o}}$ is the equilibrium constant at a reference temperature and pressure, P^{o} and T^{o}, taken to be 100 MPa and 1473 K, respectively, and ΔV^{o}, and ΔH^{o} are the volume and enthalpy changes associated with the dissolution reaction (Eqn. 3.1) and are assumed to be independent of temperature and pressure. Derivation of $X_{\mathrm{CO_3^{2-}}}^{\mathrm{melt}}$ and $X_{\mathrm{O^{2-}}}^{\mathrm{melt}}$ (Eqn. 3.2) are detailed in Stanley et al. (2011). Linear regression of the experimental data results in values of $\ln K_{\mathrm{II}}^{\mathrm{o}}$=-15.22±0.15, ΔV^{o}=21.64±0.69 cm^3 mol^{-1}, and ΔH^{o}=-25.33±6.78 kJ mol^{-1}. These differ only slightly from values derived by Stanley et al. (2011) from the experiments performed with Humphrey only. The resulting calibration for $\ln K_{\mathrm{II}}$ is compared to the experimentally determined solubilities in Fig. 3.2 (blue and red lines). This parameterization, combined with one for of K_{I} (Eqn. 3.4) after Holloway et al. (1992), allows calculation of concentrations of CO_2 in graphite-saturated martian basalt as a function of pressure, temperature, and oxygen fugacity.

Applying this model for CO_2 concentrations in graphite-saturated martian basalt to the CO_2 outgassed by martian volcanic activity requires appropriate estimates of temperatures and pressures in magmatic source regions. The characteristic conditions of partial melting in the source regions Humphrey and Y 980459 are good illustrative examples to explore these effects. Inverse experiments suggest that the source of Humphrey was near 1350±50 °C and 1.2±0.1 GPa (*Filiberto et al.*, 2008) whereas that of Y 980459 was near 1540±10 °C and 1.2±0.5 GPa

(*Musselwhite et al.*, 2006). At fixed oxygen fugacity and pressure, the hotter temperatures associated with Y 980459 result in a 120% increase in dissolved CO_2 above the same conditions at 1350 °C, i.e., at 1.2 GPa and at the iron-wüstite buffer (IW), 122 ppm vs. 56 ppm. Thus, the high temperature associated with plume sources modestly enhances graphite-saturated CO_2 outgassing. It should be noted that work on a Y 980459 composition by Blinova and Herd (2009) determined source region conditions 75-100 °C lower and 0.2 GPa higher than Musselwhite et al. (2006). Applying these source region conditions results in a slightly lower CO_2 solubility for Y 980459 (75 ppm at IW).

These results can be applied to estimate the potential CO_2 outgassed during emplacement of Tharsis. As noted in the Introduction, this giant province represents about 50% of martian igneous activity since stabilization of the ancient primordial crust, and so comprises approximately 3 x 10^8 km^3 of intrusive and extrusive magma (*Greeley and Schneid*, 1991; *Phillips et al.*, 2001). A key unknown parameter, however, is the oxygen fugacity of the Tharsis source. Following Hirschmann and Withers (2008), we consider likely source oxygen fugacities to be between IW and one order of magnitude more oxidized (IW+1), as this is the range of oxygen fugacities represented by the most primitive martian basalts, including Y 980459 itself (*Shearer et al.*, 2006). At Y 980459 source region conditions, the entire Tharsis event could have contributed no more than 30-300 mbars of CO_2 to the martian atmosphere at IW and IW+1, respectively. This is far short of the predicted 2 bars of CO_2 required to stabilize an equable climate in the late Noachian and early Hesperian epochs. Such large outgassing amounts are only feasible if the source of Tharsis magmatism was comparatively oxidized compared to martian mantle sources (i.e., IW+2 using a CO_2 solubility of 0.9 wt% in the 3 x 10^8 km^3 of Tharsis magmatism).

The critical dependence of magmatic CO_2 outgassing on oxygen fugacity requires further examination of the possibility that significant martian igneous activity derived from comparatively oxidized sources. Thus far we have emphasized sources close to IW to IW+1, as these are the conditions in the sources of primitive depleted shergottites such as Y 980459 (*Shearer et al.*, 2006). Most other depleted shergottites record similar or only slightly more oxidized sources (e.g., *Herd et al.*, 2001; *Wadhwa*, 2001; *Herd*, 2003; *McCanta et al.*, 2004; *Shearer et al.*, 2006; *McCanta et al.*, 2009), but some enriched shergottites and, in particular, some nakhlites derive from sources close to IW+2 and, in one extreme case MIL 03346, above IW+3 (*Righter et al.*, 2008; *McCanta et al.*, 2009). Highly radiogenic initial Sr in the enriched shergottites indicates

either crustal contamination or derivation from a very restricted mantle source (*Herd*, 2003), but an oxidized nakhlite source in the martian mantle is plausible (*Dyar et al.*, 2005; *Righter et al.*, 2008; *McCanta et al.*, 2009). Whether a similar source could be responsible for much of Tharsis or a large proportion of other post-4.5 Ga martian magmatism is not easily evaluated. Interestingly, it has been suggested that the nakhlites could come from Tharsis (*Treiman*, 2005), though their Amazonian age (1.3 Ga; *Treiman*, 2005, and references therein) would require that they derive from the younger resurfaced carapace, rather than the volumetrically dominant Noachian mass.

Chapter 4

Solubility of C-O-H volatiles in graphite-saturated martian basalts

4.1 Introduction

The modern martian atmosphere is thin, leading to surface conditions unable to support liquid water. Yet, there is evidence of liquid surface water early in martian history that is commonly thought to require a thick CO_2 atmosphere (*Pollack et al.*, 1987; *Pepin*, 1994; *Carr*, 1999; *Jakosky and Phillips*, 2001). Alternatively, the early warm climate on Mars might have been produced by other gases, such as CH_4 or SO_2 (*Chevrier et al.*, 2007; *Halevy et al.*, 2007; *Gaillard and Scaillet*, 2009; *Righter et al.*, 2009; *Halevy and Head*, 2012). Regardless of the gas species, the primary greenhouse gases on Mars derive ultimately from the mantle. The processes that liberate these components from the mantle control the total flux of juvenile C-O-H gas from the interior to the near-surface environment.

In a relatively oxidized mantle, carbon is stored as carbonate at depth (*Luth*, 1999), which can significantly lower the locus of melting and leading to efficient extraction of carbon from the deep interior (*Dasgupta and Hirschmann*, 2006). The martian mantle is thought to be reduced, with mantle oxygen fugacities from the iron-wüstite (IW) buffer to one log unit above IW (IW+1) (*Hale et al.*, 1999; *Wadhwa*, 2001; *Herd et al.*, 2002; *Herd*, 2003; *Shearer et al.*, 2006; *Karner et al.*, 2007; *Righter et al.*, 2008), and so the stable phase of carbon in the martian mantle is likely graphite (*Hirschmann and Withers*, 2008; *Righter et al.*, 2008).

Our previous work follows the analysis developed by Holloway and co-workers (*Holloway*

et al., 1992; *Holloway*, 1998) that predicts a linear relationship between CO_2 and oxygen fugacity (f_{O_2}) in graphite-saturated silicate melts. At low oxygen fugacity, the solubility of CO_2 in silicate melts is therefore very low (*Holloway et al.*, 1992; *Pawley et al.*, 1992; *Holloway*, 1998; *Hirschmann and Withers*, 2008). Such low calculated solubilities under reducing conditions lead to small fluxes of CO_2 associated with martian magmatism, and therefore the volume of mantle-derived magma required to produce a thick CO_2 atmosphere may be prohibitively large (*Hirschmann and Withers*, 2008; *Stanley et al.*, 2011, 2012). Thus, these experiments and calculations challenge the current model of the origins of a late Noachian CO_2 greenhouse on Mars.

Our previous studies investigated CO_2 solubility in martian basalts at oxidizing conditions without graphite present, and then extrapolated to more reduced, graphite-saturated conditions. This work investigates the inherent assumptions of that method by experimentally determining the solubilities of C-O-H volatiles as a function of oxygen fugacity in model martian primitive magmas with coexisting graphite. The key assumption is that the carbonate ion is the chief soluble C-O-H species. Our predictions change drastically with any appreciable solubility of other reduced carbon species, including CO (*Brooker et al.*, 1999), carbonyl (C=O; *Kadik et al.*, 2006) complexes, carbide (Si−C; *Kadik et al.*, 2006), or CH_4 (*Taylor and Green*, 1987; *Mysen et al.*, 2009). Brooker et al. (1999) detected CO in $Na_2O-Al_2O_3-SiO_2$ liquids, but did not quantify its concentrations, and it has not been detected in reduced natural magma compositions (*Pawley et al.*, 1992; *Kadik et al.*, 2006). At very reduced conditions (<IW-2) carbonyl (C=O) and carbide (Si−C) complexes have been detected in Fe-bearing silicate melts (*Kadik et al.*, 2006). Recent studies documented CH_4 in quenched silicate and aluminosilicate glasses (*Kadik et al.*, 2006; *Mysen et al.*, 2009; *Kadik et al.*, 2011), though results from Ardia et al. (submitted to *Geochimica et Cosmochimica Acta*) suggest that emissions of methane associated with martian magmatism may also be limited.

The linear relationship between CO_2 solubility and oxygen fugacity would be affected if carbon was stored in a reduced phase other than graphite. In this case the activity of carbon is no longer unity and so one would expected a lower CO_2 solubility at a given oxygen fugacity. Additionally, the Holloway method assumes perfect Henrian behavior, or that the solubility of a gas in a liquid is directly proportional to the fugacity of that gas. The model of Papale (1999) is consistent with experiments, and shows that both H_2O and CO_2 transition from essentially Henrian to strongly non-Henrian behavior as the pressure is increased from tens to hundreds of

MPa. In this model, each dissolved volatile molecule modifies the liquid composition and the mole fractions of all the other components by changing the average number of ions surrounding any specific molecule. As a result the high-pressure solubilities of both volatiles change from those predicted at lower pressures. Clearly, experimental studies of the concentrations of C-O-H volatiles as a function of oxygen fugacity with graphite present are required to assess the validity of these assumptions.

4.2 Methods

4.2.1 Starting materials and experimental procedures

The principal aim of this study is to investigate experimentally the extraction of C-O-H volatiles from the martian mantle by determining the concentrations of C-O-H volatiles as a function of oxygen fugacity in model martian primitive magmas coexisting with graphite. Starting materials were selected to produce appropriate model martian liquid and, when applicable, mineral phase compositions. Three subsets of experiments were performed with a range of starting materials (Tables 4.1 and 4.A.1). All starting materials used synthetic Humphrey basalt (*Stanley et al.*, 2011) mixed with other compositions to produce the desired phases. Initial experiments investigated the solubility of C-O-H volatiles as a function of oxygen fugacity in model martian basaltic melts coexisting with olivine, orthopyroxene, and graphite. Starting materials for the experiments were prepared by mixing ~70% basalt, ~15% olivine, and ~15% pigeonite. The basalt component used varying ratios of oxidized to reduced Humphrey basalt in an attempt to control the oxygen fugacity. Later experiments used a base of reduced Humphrey starting mixed with Fe metal to reduce the charge and, for certain experiments, Pt powder to act as an oxygen fugacity indicator. Detailed methods regarding starting materials are presented in the Supplementary information section.

Experiments were performed in 4 mm Pt-graphite double capsules at pressures of 1.0-3.0 GPa and temperatures of 1340-1600 °C in a half-inch (12.5 mm), end-loaded piston-cylinder apparatus under hot piston-in conditions. Run durations of 3-24 h were chosen to ensure equilibration of coexisting phases. Conditions for individual experiments are listed in Table 4.1. The experimental assembly consisted of $BaCO_3$ or CaF_2 sleeves surrounding straight graphite heaters and internal spacers of crushable MgO. Temperatures were measured and controlled using a $W_{97}Re_3$-$W_{75}Re_{25}$ (Type D) or Pt-$Pt_{90}Rh_{10}$ (Type S) thermocouple placed above the

Table 4.1: Experimental conditions and phase assemblages.

Exp. #	P (GPa)	T (°C)	t (h)	starting material[a]	Pt[b]	phases
B330	1.0	1355	24	100-0	bead	gl, cpx, ol
B332	1.0	1355	24	100-0	bead	gl, cpx, ol
B347	1.0	1355	24	50-50	bead	gl, cpx, ol
B349	1.0	1355	24	75-25	bead	gl, cpx, ol
B361	1.0	1355	24	25-75	wire	gl, cpx, ol
B368	1.0	1340	24	0-100	wire	gl, cpx, ol
B372	1.0	1355	24	12.5-87.5	wire	gl, cpx, ol
B379	1.0	1355	24	50-50	wire	gl, cpx, ol
A877	1.0	1355	24	75-25	wire	gl, cpx, ol
B412	1.0	1340	24	0-100+Fe(2.6)	wire	gl, cpx, ol
B420	1.0	1340	24	0+Fe(2.6)	wire	gl, cpx, ol
B441	1.0	1340	24	0+Fe(2.6)	wire	gl, cpx, ol
B442	1.0	1340	24	0+Fe(2.6)	wire	gl, cpx, ol
B465	1.0	1340	24	0-100+Fe(4.0)	powder	gl
B466	1.0	1340	24	0+Fe(8.0)	-	gl, Fe-C
B477	2.0	1500	4.5	0+Fe(4.0)	powder	gl
B485	2.0	1500	4.5	0+Fe(2.5)*	powder	gl
B486	1.0	1400	6	0+Fe(2.5)*	powder	gl
B489	2.0	1500	4.5	0+Fe(8.0)	-	gl, Fe-C
B490	1.0	1400	6	0+Fe(8.0)	-	gl, Fe-C
B491	3.0	1600	3	0+Fe(8.0)*	-	gl, Fe-C
B492	1.0	1400	6	0+Fe(8.0)*+H_2O	-	gl, Fe-C
B493	2.0	1500	4.5	0+Fe(8.0)*+H_2O	-	gl, Fe-C
B494	3.0	1600	3	0+Fe(8.0)*+H_2O	-	gl, Fe-C
B495	1.0	1400	6	0+Fe(4.0)	powder	gl
B497	2.0	1500	4.5	0+Fe(8.0)*+Pt	powder	gl

[a] - starting material designations are described in Table 4.A.1 and section 4.A;

[b] - indicates method of Pt addition to experiment. gl = suitably large glassy areas formed to perform FTIR analyses, ol = olivine, cpx = clinopyroxene, Fe-C = quenched carbide melt.

capsule. We applied a pressure correction of -0.2 GPa for this assembly, and attribute *P-T* uncertainties of ±0.1 GPa and ±12 °C respectively (*Xirouchakis et al.*, 2001). Experiments were quenched by turning off the power to the piston-cylinder.

4.2.2 Electron microprobe (EMP) analysis

Recovered capsules were sectioned using a 50 μm diameter tungsten wire saw. One half of the capsule was polished for compositional analysis, using diamond lapping films (15-1 μm), while the remaining half was doubly polished for volatile analysis. Major element contents of all phases from run products were analyzed by wavelength-dispersive spectroscopy using a 15 kV acceleration voltage with a JEOL JXA8900R electron microprobe. Silicate phases used count times of 20 s for the peak and 10 s for the background for all elements except Na, which was counted for 10 s and 5 s. Na and K were always measured first on respective spectrometers. Glass analyses were performed using a 10 nA beam current and a partially defocused beam (5 μm), while mineral analyses used 15 nA beam current and a focused beam (0 μm). Silicate standards consisted of natural apatite, hornblende, hypersthene, Na-bearing omphacite, augite, Mn-hortonolite, K-feldspar, San Carlos olivine, and two basaltic glasses. Pure metal Fe, Pt, and Si standards were used for metallic phases. Analyses of FePt alloys and carbides used a focused beam, 5 nA beam current, and count times of 35 s for the peak and 15 s for the background. The Pt Mα line was used because it produces a flatter background and better signal-to-noise ratio than the Kα line.

4.2.3 Fourier transform infrared (FTIR) spectroscopy

The volatile content of experimental doubly polished glass was determined using a Bruker Tensor 37 FTIR spectrometer and Hyperion 2000 microscope. A mid-IR source was used with a KBr beamsplitter for each unpolarized spectra taken on a square 45 × 45 μm spot. 256 scans were taken over a range of 600-7000 cm^{-1} with a resolution of 4 cm^{-1}. Two main regions of interest in each spectra, the CO_3^{2-} absorption region from 1350-1650 cm^{-1} and the OH^- absorption region from 2800-3800 cm^{-1}, were quantified using the Beer-Lambert law as detailed in Stanley et al. (2011). We applied the density, ρ = 3040±50 kg m^{-3}, and CO_2 integrated molar absorptivity, ε^*=81500±1500 L mol^{-1} cm^{-2}, for glassy Humphrey basalt that were determined by Stanley et al. (2011). Discussion of baseline selection is provided in the Supplementary

information section.

4.2.4 Raman spectroscopy

Experimental glasses were analyzed by microRaman spectroscopy using a Witec Alpha300 R confocal microscope with UHTS300 spectrometer and DV401 CCD detector. The laser power was set to 30 mW at the source on a 514.5 nm Omnichrome Argon ion laser using a 600 mm^{-1} grating and a resolution of 1 cm^{-1}. Spectra were recorded in a 1175-4500 cm^{-1} frequency range to investigate the main C-O-H species. Acquisition times were 60 s with 2 acquisitions per analytical spot. Using a 100× lens, the beam diameter is less than 1 μm, with a penetration depth of 2-3 μm into the sample.

4.2.5 Secondary ion mass spectrometry (SIMS)

Concentrations of total C and H_2O in experimental glasses, as well as C contents of experimental carbides were determined by secondary ion mass spectrometry. Experimental capsules and standards were cleaned in three baths of acetone to remove Crystalbond^{TM} and any other C-O-H-bearing contaminants, and were then baked overnight at 100 °C in a vacuum-drying oven. Samples and standards were then pressed into indium (Fig. 4.1), baked overnight at 100 °C, and then mounts were sputter-coated with Au. SIMS analyses were performed on the Cameca 6f at Arizona State University using a Cs^+ primary ion source with a beam current of ~10 nA and an impact energy of 15 KeV. The beam was focused to a spot approximately 35 μm in diameter, but only secondary ions sputtered from the central 8 μm of the crater were allowed into the mass spectrometer. Prior to each analysis, the beam was rastered over a 25 × 25 μm area for 3 min to sputter away the gold coating and any surface adsorbed contaminants. A potential of -5000 V was applied to the sample, resulting in the acceleration of negative secondary ions produced by the primary ion impacts away from the sputtering site. Secondary ions with excess kinetic energies of 0±125 eV (energy bandpass centered and wide open) were allowed into the mass spectrometer, detected with an electron multiplier, and corrected for background and counting system deadtime.

The alignment of the electron gun was achieved by decreasing the sample voltage until the impact energy of the electrons was sufficient to induce an image on a cathodoluminescent (CL) sample. The electron beam was tuned to give a homogeneous CL image (*Chen et al.,* in review

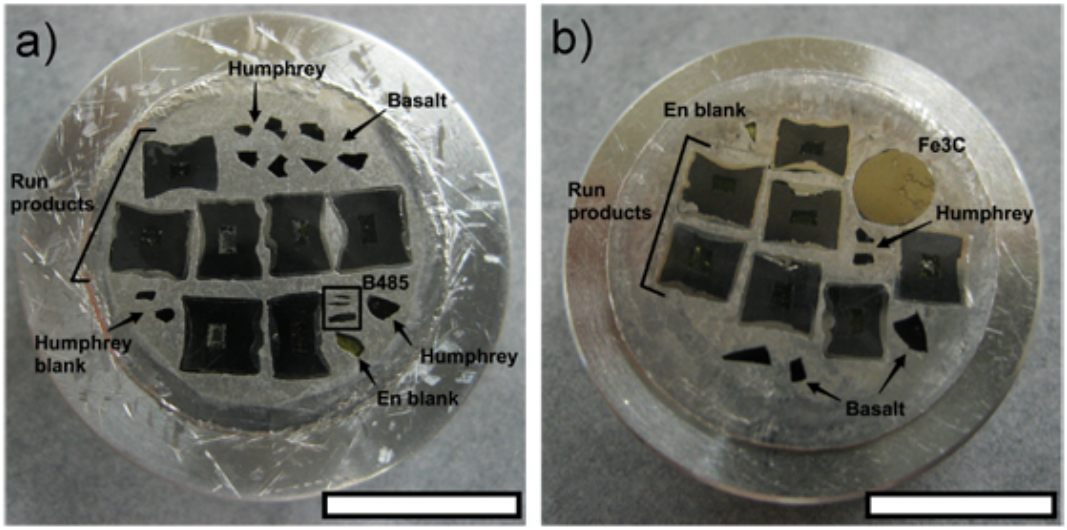

Figure 4.1: Optical micrograph of indium SIMS mount containing experimental run products, basalt standards and blanks, enstatite blanks, and a Fe_3C standard. The diameter of the mount is 25.4 mm and both scale bars are 10 mm.

in *Nuclear Instruments and Methods, B*), and the sample voltage was returned to the same value as the filament. Only very minor corrections of the electron gun tuning (steering the electrons in x and y space on the sample) were needed to obtain a uniform secondary ion image on a test insulator (a gold-coated glass slide) under bombardment by a Cs beam. No changes in electron gun tuning were needed over the 5 days of analysis, as shown by the good reproducibility on unknowns and standards from day to day.

Each silicate glass analysis consisted of counting negative ion intensities for ^{12}C, $^{16}O^{1}H$, ^{19}F, and ^{28}Si, with counting times of 10, 5, 5, and 2 s, respectively. Carbide analyses counted on negative ion intensities for ^{12}C, ^{28}Si, and ^{56}Fe, with counting times of 5, 5, and 10 s, respectively. These cycles were repeated 6 times in each analysis. The intensities of the ^{19}F for glass and ^{28}Si for carbide were not quantified; rather, they were monitored to detect overlap of the analyzed area on any foreign material in pits and/or cracks around the phases of interest.

4.3 Oxygen fugacity determination

The presence of graphite in our experiments does not act as an oxygen fugacity buffer, but rather as an upper limit (*Holloway et al.*, 1992). For this reason, we added small amounts of

Pt to most experiments. During the experiment these become FePt alloys, through equilibrium between all the Fe-bearing phases, and allow post-experiment evaluation of f_{O_2} by at least two different methods. First, we performed experiments designed so that melt coexists with small amounts of olivine and orthopyroxene, allowing thermodynamic analysis of the equilibrium reaction between these phases and FePt alloy,

$$\underset{\text{alloy}}{2\,Fe} + O_2 + \underset{\text{opx}}{Fe_2Si_2O_6} \rightleftharpoons 2\,\underset{\text{ol}}{Fe_2SiO_4}, \tag{4.1}$$

using measured compositions of the phases and thermodynamic models for FePt alloy, pyroxene, and olivine.

The MELTS Supplemental Calculator allows the calculation of the thermodynamic properties of olivines (*Sack and Ghiorso*, 1989; *Hirschmann*, 1991) and pyroxenes (*Sack and Ghiorso*, 1994a,b,c), but only using certain endmembers (e.g. Fe_2SiO_4, Mg_2SiO_4, and $CaMgSiO_4$ for olivines). Pyroxenes in this study have 0.92-2.15 wt% CaO (Table 4.2), requiring the use of the full pyroxene version of the MELTS calculator, including concentrations of SiO_2, MgO, FeO, CaO, and Al_2O_3. Using the MELTS endmembers, the following substitution must be made in Eqn. 4.1

$$\underset{\text{opx}}{Fe_2Si_2O_6} = 2\,\underset{\text{cpx}}{CaFeSi_2O_6} - 2\,\underset{\text{cpx}}{CaMgSi_2O_6} + \underset{\text{clinoenstatite}}{Mg_2Si_2O_6} \tag{4.2}$$

yielding the reaction

$$\underset{\text{alloy}}{2\,Fe} + O_2 + 2\,\underset{\text{cpx}}{CaFeSi_2O_6} - 2\,\underset{\text{cpx}}{CaMgSi_2O_6} + \underset{\text{cpx}}{Mg_2Si_2O_6} \rightleftharpoons 2\,\underset{\text{ol}}{Fe_2SiO_4}, \tag{4.3}$$

from which f_{O_2} can be calculated using

$$\begin{aligned}\log f_{O_2} = \frac{1}{\ln(10)}\Big[&2\,\ln a^{\text{ol}}_{Fe_2SiO_4} - 2\,\ln a^{\text{cpx}}_{CaFeSi_2O_6} + 2\,\ln a^{\text{cpx}}_{CaMgSi_2O_6} - \ln a^{\text{opx}}_{Mg_2Si_2O_6} \\ &-2\,\ln a^{\text{alloy}}_{Fe} - \left(\frac{-\Delta G^{\circ}_r}{RT}\right)\Big].\end{aligned} \tag{4.4}$$

Mineral activities are derived using MELTS Supplemental Calculator and $a_{\mathrm{Fe}}^{\mathrm{alloy}}$ is calculated following Kessel et al. (2001). The MELTS calculator provides free energies for mineral components that are apparent values relative to the elements at 298.15 K and 1 bar. We correct standard state from 298.15 K to the temperature of interest using the method of Kessel et al. (2001, Eqn. 15) and a third-order Birch-Murnaghan pressure correction using coefficients V^{o}, K, and K' from Campbell et al. (2009) and α^{o} from Boehler et al. (1990).

Oxygen fugacity for experiments containing glass and FePt alloy was estimated by analysis of the reaction between FePt alloy and FeO in the melt

$$\underset{\text{alloy}}{\mathrm{Fe}} + \tfrac{1}{2}\mathrm{O}_2 \rightleftharpoons \underset{\text{melt}}{\mathrm{FeO}}. \tag{4.5}$$

(*Grove*, 1981; *Médard et al.*, 2008) from which f_{O_2} can be calculated using

$$\log f_{\mathrm{O}_2} = \frac{2}{\ln(10)}\left[\ln\left(\frac{X_{\mathrm{FeO}}^{\mathrm{melt}}}{X_{\mathrm{Fe}}^{\mathrm{alloy}}}\right) - \ln\gamma_{\mathrm{Fe}}^{\mathrm{alloy}} + \ln\gamma_{\mathrm{FeO}}^{\mathrm{melt}} - \ln K\right] \tag{4.6}$$

with $\gamma_{\mathrm{Fe}}^{\mathrm{alloy}}$ calculated following Kessel et al. (2001). The activity coefficient of FeO in the melt was assumed to be unity in Médard et al. (2008), who use an experimental calibration of the equilibrium constant thereby including any small changes in $\gamma_{\mathrm{FeO}}^{\mathrm{melt}}$. Values of $X_{\mathrm{FeO}}^{\mathrm{melt}}$ were calculated on a cation basis. This second method allows f_{O_2} estimation in a wider range of experiments, but is has lower accuracy than the first owing to uncertainties in estimates of $a_{\mathrm{FeO}}^{\mathrm{melt}}$.

In experiments without FePt alloys, oxygen fugacity can be estimated using Eqn. 4.5 to define the reaction between iron in Fe-C carbide melt and FeO in silicate melt. The equilibrium reaction for this equation is written as

$$\log K = \log\left(\frac{a_{\mathrm{FeO}}^{\mathrm{melt}}}{a_{\mathrm{Fe}}^{\mathrm{Fe-C}}}\right) - \tfrac{1}{2}\log f_{\mathrm{O}_2}^{\mathrm{exp}} \tag{4.7}$$

where $\log f_{\mathrm{O}_2}^{\mathrm{exp}}$ is the oxygen fugacity of the experiment. The equilibrium constant of the reaction between pure Fe and pure FeO (a_{FeO} and $a_{\mathrm{Fe}} = 1$), which is determined by the IW buffer, can be written as

$$\log K = -\tfrac{1}{2} \log f_{O_2}(\mathrm{IW}) \tag{4.8}$$

where $\log f_{O_2}(\mathrm{IW})$ is the oxygen fugacity of the IW buffer at experimental conditions. Using Eqns. 4.7 and 4.8, $\log f_{O_2}^{exp}$ can be rewritten as

$$\log f_{O_2}^{exp} = \log f_{O_2}(\mathrm{IW}) - \Delta \log f_{O_2}(\mathrm{IW}) \tag{4.9}$$

where $\Delta \log f_{O_2}(\mathrm{IW})$ is the difference between the experimental oxygen fugacity and the IW buffer at experimental conditions. Combining the Eqns. 4.7, 4.8, and 4.9 gives

$$\Delta \log f_{O_2}(\mathrm{IW}) = 2 \log \left(\frac{a_{FeO}^{melt}}{a_{Fe}^{Fe-C}} \right) \tag{4.10}$$

with a_{Fe}^{Fe-C} calculated using the method of Wang et al. (1991). The activity coefficient of FeO in the melt was assumed to be unity which makes $a_{FeO}^{melt} = X_{FeO}^{melt}$. Values of X_{FeO}^{melt} were calculated on a cation basis. This method has similar accuracy issues as the second owing to uncertainties in estimates of a_{FeO}^{melt}.

4.4 Results

4.4.1 Electron microprobe results

Experimental products can be divided into three subsets of experiments. First, experiments consisting of coexisting olivine, clinopyroxene, glass, and FePt alloy. In these experiments, Pt was initially added as small, flattened beads and was later added as small strips of wire to reduce the mass of Pt, and therefore Fe-loss to the FePt alloy. About 20 microprobe points were collected for each silicate phase. Those mineral phases analyses with totals > 101% or < 99%, and analyses giving poor stoichiometry (±0.01 total cations) calculated on a 4- (olivine) or 6- (clinopyroxene) oxygen basis, were discarded. Reported compositions are averages of the remaining analyses (7-24 analyses per reported phase, Table 4.2). Glass analyses are reported on a volatile-free basis in Table 4.3.

In all experiments a significant amount of melt quenched to glass with high FeO (~16-24 wt%) similar to martian basalts from our previous studies (*Stanley et al.*, 2011, 2012). Clinopyroxenes formed large (50-100 μm) crystals with thick rims (Fig. 4.2b-c), which were preferentially analyzed by EMP. Olivines formed many small (10-30 μm) crystals; any thin rims (Fig. 4.2b-c) that formed were avoided during EMP analyses due to quench modification. Back-scattered electron images suggest that the analyzed regions of the crystalline phases are homogeneous. Single points on multiple crystals, as well as linear transects on larger crystals, showed little variation between individual spots, suggesting that analyzed regions of mineral phases were homogeneous and approached equilibrium during the experiment. Beads of FePt alloys showed slight compositional zoning and so the rims were analyzed exclusively. The use of Pt wire or powder in later experiments avoided this issue.

Initial attempts to produce charges well below the CCO buffer using only variations in starting material Fe^{3+}/Fe^{T} were unsuccessful (Table 4.4). Médard et al. (2008) showed that adding an Fe-rich FePt alloy to the charge buffers the oxygen fugacity at lower values. We added Fe metal to the starting material, which produced the same effect by alloying with the Pt present in the charge. In experiments without Pt present this additional reduced iron formed the Fe-C carbides seen in the third subset of experiments.

The second subset of experiments consisted of coexisting glass and FePt alloy. These experiments added Pt as a powder along with varying amounts of Fe metal (Tables 4.1 and 4.A.1). Experimental durations were shortened to 3-6 h because the resulting small (1-7 μm) FePt alloy beads (Fig. 4.2d-e) equilibrated with the glass quickly and no large crystals were grown. The small beads bunched together throughout the capsule rather than coalescing into larger blobs. Reported experiments showed minor quench crystallization nucleating from the sides of the capsule but enough glass remained for all analysis techniques. Addition of Fe metal to the

Figure 4.2 ***(following page)*****:** Back-scattered electron (BSE) images of experimental run products. a) B349 (1355 °C, 1.0 GPa, Pt added as a flattened bead) produced coexisting olivine, clinopyroxene, glass, and FePt alloy. The majority of the partial melt quenched at the top of the capsule allowing FTIR measurements of CO_2 and H_2O concentrations. b-c) Textures of olivine and clinopyroxene in similar experiments. Thick rims are present in most large clinopyroxenes and were the focus of EMP analyses. Thin quench rims of the olivines were avoided in favor of more homogeneous cores. d) B486 (1400 °C, 1.0 GPa, Pt added as Pt powder) produced coexisting glass and small (1-7 μm) beads FePt alloy. e) Textures of glass and FePt alloy beads. The beads tend to clump together rather than aggregating into larger blobs. f) B493 (1500 °C, 2.0 GPa, no Pt added) produced coexisting glass and large (10-200 μm) Fe-C carbide droplets. Abbreviations as defined in Table 4.1. All scale bars are 100 μm.

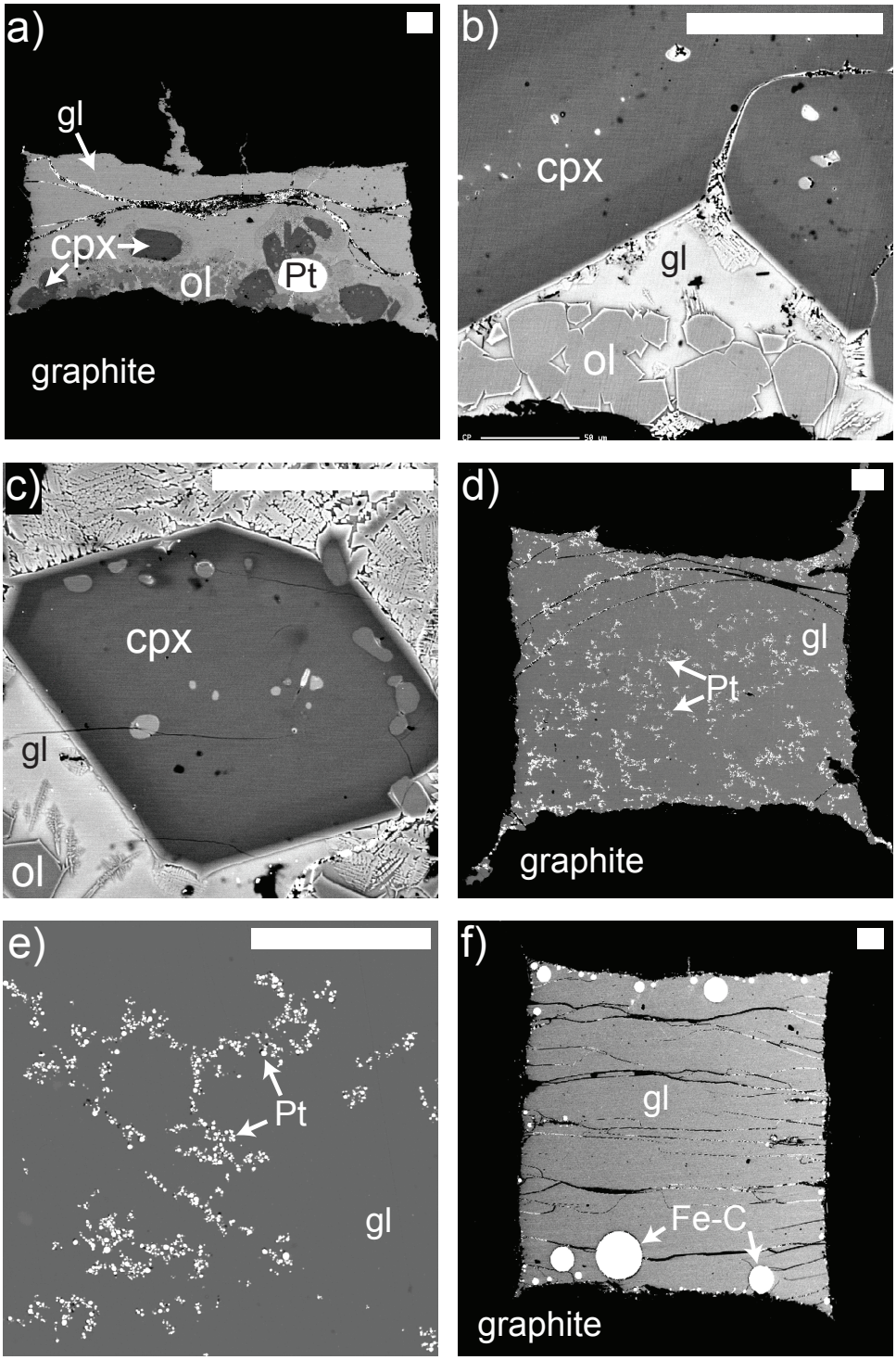
a)
gl
cpx
ol
Pt
graphite
b)
cpx
gl
ol
c)
cpx
gl
ol
d)
gl
Pt
graphite
e)
Pt
gl
f)
gl
Fe-C
graphite

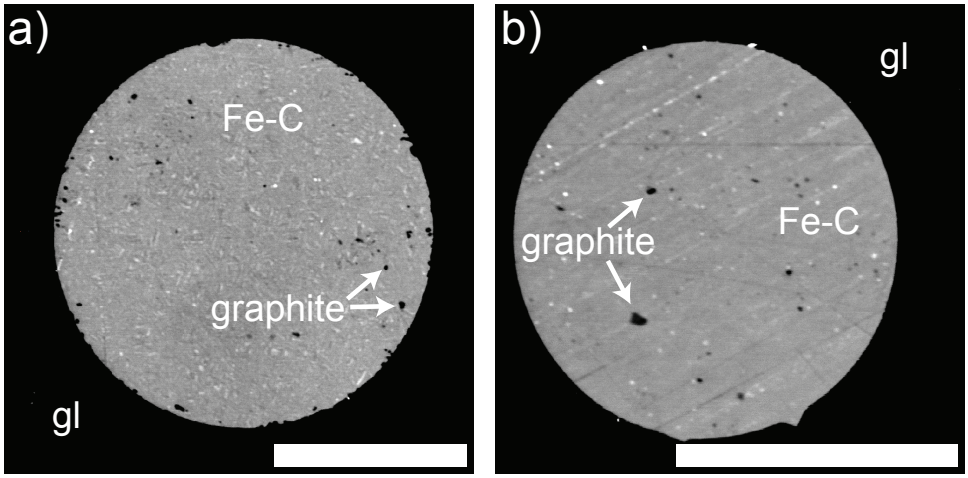

Figure 4.3: Back-scattered electron (BSE) images of quenched Fe-C carbide droplet textures with graphite inclusions in: a) B490 (1400 °C, 1.0 GPa) and b) B493 (1500 °C, 2.0 GPa). Abbreviations as defined in Table 4.1. All scale bars are 100 μm.

charge increased the FeO content of the glass (Table 4.3) but not so much that it was no longer representative of martian basalts.

The final subset of experiments consisted of coexisting glass and Fe-C droplets. These experiments had no Pt added and used starting materials combining reduced Humphrey basalt and 8 wt% Fe metal. Experimental carbide droplets showed quench textures and small dark spots interpreted as graphite inclusions (Fig. 4.3a-b). EMP analyses of Fe-C droplets produced larger standard deviations than FePt alloys (Table 4.4), indicating possible heterogeneous quenching from a liquid at experimental conditions.

Results of glass-Pt and glass-carbide oxygen fugacity determinations are listed in Table 4.4. This study presents experiments over a range of oxygen fugacities, though the olivine-clinopyroxene-Pt method was only applicable to the more oxidized experiments in this study. Values of f_{O_2} determined in experiments with coexisting olivine, clinopyroxene, melt, and FePt alloy using the olivine-clinopyroxene-Pt and glass-Pt (*Médard et al.*, 2008) determination methods are within ~0.30 log units of oxygen fugacity along a parallel linear trend (Fig. 4.4). Our results show that either approach can be used with confidence in experiments at oxygen fugacities near CCO.

Table 4.2: Electron microprobe analyses of silicate minerals, reported in wt%.

Exp. #	phase	n	SiO_2	TiO_2	Al_2O_3	FeO	MnO	MgO	CaO	Na_2O	K_2O	P_2O_5	Total
B330	ol	12	38.63	0.01	0.16	20.92	0.37	38.83	0.30	0.03	0.01	0.09	99.35
	cpx	20	55.52	0.04	1.30	13.04	0.33	28.48	1.44	0.06	0.00	0.02	100.23
B332	ol	13	39.25	0.02	0.05	21.01	0.34	39.64	0.27	0.02	0.01	0.08	100.68
	cpx	17	55.50	0.02	1.25	13.06	0.32	28.53	1.32	0.06	0.00	0.01	100.08
B347	ol	16	39.21	0.02	0.05	17.68	0.33	42.61	0.25	0.02	0.01	0.05	100.23
	cpx	11	55.76	0.04	1.55	12.84	0.32	28.47	1.39	0.05	0.01	0.01	100.43
B349	ol	18	38.75	0.01	0.04	20.12	0.34	40.73	0.23	0.01	0.00	0.04	100.28
	cpx	11	55.95	0.04	1.21	12.34	0.30	29.61	0.92	0.05	0.01	0.01	100.43
B368	ol	24	38.52	0.01	0.05	24.28	0.40	36.78	0.30	0.01	0.01	0.05	100.41
	cpx	8	55.35	0.03	0.96	14.49	0.39	27.12	2.15	0.06	0.00	0.01	100.58
B379	ol	18	38.90	0.01	0.04	22.32	0.35	38.22	0.25	0.02	0.01	0.07	100.19
	cpx	14	55.29	0.05	1.22	13.12	0.31	28.63	1.41	0.05	0.00	0.01	100.08
B420	ol	7	37.21	0.00	0.06	27.40	0.36	34.85	0.25	0.01	0.01	0.05	100.20
	cpx	12	53.93	0.06	1.36	17.22	0.37	24.88	2.02	0.08	0.00	0.01	99.93

n = number of analyses, ol = olivine, cpx = clinopyroxene.

Table 4.3: Electron microprobe analyses of glasses, reported in wt%.

Exp. #	n	SiO_2	TiO_2	Al_2O_3	FeO	MnO	MgO	CaO	Na_2O	K_2O	P_2O_5	Total
B330	20	48.81	0.50	10.14	17.38	0.38	11.04	8.50	2.54	0.16	0.53	100
B332	40	48.24	0.50	9.62	18.27	0.38	11.66	8.28	2.41	0.15	0.50	100
B347	20	49.81	0.41	9.07	15.86	0.40	14.24	7.52	2.14	0.11	0.46	100
B349	19	48.82	0.47	9.39	17.99	0.36	12.47	7.64	2.30	0.11	0.44	100
B361	19	49.17	0.45	9.93	17.07	0.38	11.96	7.97	2.39	0.15	0.51	100
B368	18	49.02	0.49	11.17	17.71	0.35	9.44	8.69	2.41	0.16	0.55	100
B372	16	48.75	0.52	11.57	17.99	0.34	8.81	8.92	2.39	0.15	0.57	100
B379	39	49.39	0.43	10.38	17.98	0.36	10.41	8.21	2.19	0.13	0.51	100
A877	18	47.67	0.58	13.47	18.48	0.33	6.14	9.63	2.83	0.16	0.70	100
B412	17	48.21	0.41	8.72	19.22	0.38	13.66	6.70	2.12	0.10	0.48	100
B420	19	48.84	0.43	9.67	21.45	0.34	9.10	7.16	2.42	0.12	0.46	100
B441	18	48.81	0.41	8.96	19.27	0.36	12.29	7.04	2.31	0.11	0.44	100
B442	12	48.34	0.44	9.55	18.17	0.36	12.69	7.44	2.40	0.11	0.51	100
B465	14	47.15	0.34	7.53	21.29	0.34	15.08	5.96	1.83	0.09	0.39	100
B466	15	46.07	0.35	7.52	23.16	0.33	14.20	6.04	1.87	0.08	0.39	100
B477	28	47.06	0.34	7.57	21.55	0.35	15.08	5.84	1.75	0.08	0.38	100
B485	12	47.21	0.48	10.27	20.63	0.32	10.31	7.51	2.63	0.13	0.51	100
B486	10	47.57	0.46	10.44	20.27	0.34	10.19	7.61	2.50	0.13	0.49	100
B489	18	46.30	0.37	7.74	22.56	0.34	14.31	6.03	1.87	0.10	0.39	100
B490	14	45.60	0.36	7.40	24.41	0.30	13.68	5.89	1.86	0.08	0.42	100
B491	18	46.82	0.52	10.04	20.79	0.32	10.66	7.74	2.58	0.12	0.41	100
B492	12	46.98	0.47	10.05	21.09	0.32	10.42	7.55	2.54	0.14	0.44	100
B493	13	46.75	0.49	10.03	20.72	0.32	10.72	7.79	2.63	0.11	0.44	100
B494	14	46.65	0.53	10.12	20.94	0.34	10.62	7.79	2.52	0.11	0.40	100
B495	12	46.69	0.37	7.41	21.21	0.35	15.44	6.10	1.93	0.09	0.41	100
B497	12	46.38	0.47	9.80	22.45	0.30	10.21	7.45	2.37	0.12	0.46	100

Oxides reported on a volatile-free basis. n = number of analyses.

Table 4.4: Oxygen fugacity determination and volatile contents analyzed by FTIR.

Exp. #	Fe		f_{O_2}			CO_2	CO_2 predicted	H_2O
	(wt%)	s.d.	log	ΔIW	ΔCCO	(wt%)	(wt%)	(wt%)
B330	13.53	0.58	-7.53	2.28	0.33	0.32	1.19	0.44
B332	13.93	0.15	-7.60	2.21	0.27	0.29	1.04	0.39
B347	13.90	0.08	-7.72	2.09	0.14	0.43	0.79	0.40
B349	13.40	0.47	-7.47	2.34	0.39	0.38	1.40	0.55
B361	13.75	0.11	-7.61	2.20	0.26	0.50	1.03	0.78
B368	15.01	0.15	-8.00	1.97	-0.01	0.27	0.58	0.55
B372	15.15	0.13	-7.90	1.91	-0.03	0.31	0.54	0.85
B379	15.17	0.19	-7.91	1.90	-0.04	0.29	0.53	0.53
A877	14.90	0.15	-7.81	2.00	0.05	0.23	0.67	0.49
B412	14.48	0.07	-7.80	2.16	0.18	0.44	0.92	0.33
B420	20.43	0.17	-8.85	1.11	-0.87	0.015	0.083	0.53
B441	16.41	0.23	-8.24	1.73	-0.26	0.19	0.34	0.49
B442	14.21	0.17	-7.79	2.18	0.19	0.38	0.98	0.43
B465	20.86	0.17	-8.47	0.89	-0.94	0.051	0.051	0.35
B466	93.48[a]	1.21	-10.74	-0.77	-2.75	0.0068	0.0011	0.26
B477	28.72	0.49	-8.16	-0.02	-2.01	0.0125	0.0088	0.47
B485	23.90	0.21	-7.75	0.39	-1.60	0.012	0.023	0.39
B486	19.87	0.27	-8.36	1.01	-0.83	0.044	0.091	0.52
B489	92.71	1.28	-9.00	-0.86	-2.84	0.0036	0.0014	0.40
B490	93.62	1.16	-10.19	-0.82	-2.65	0.0047	0.0014	0.29
B491	93.30	0.61	-7.96	-0.92	-3.03	0.0040	0.0014	0.36
B492	93.30	1.13	-10.24	-0.87	-2.70	0.0026	0.0013	0.35
B493	93.34	0.45	-9.01	-0.87	-2.86	0.0060	0.0014	0.36
B494	93.51	0.86	-7.70	-0.65	-2.77	0.0046	0.0027	0.38
B495	42.92	0.28	-10.07	-0.71	-2.54	0.0069	0.0019	0.54
B497	33.18	0.44	-8.41	-0.27	-2.26	0.0081	0.0057	0.45

[a] - Fe contents greater than 90 wt% are carbide-bearing experiments. f_{O_2} determined in Pt-bearing experiments by glass-Pt method using Fe content of FePt alloys analyzed with EMP, and in carbide-bearing experiments by glass-carbide method using C content of carbides analyzed with SIMS. IW buffer from O'Neill and Pownceby (1993) with the pressure dependence of Eugster and Wones (1962). CCO from Frost and Wood (1997). CO_2 predicted uses the parameterization from Stanley et al. (2012) and the P-T-f_{O_2} conditions for each experiment.

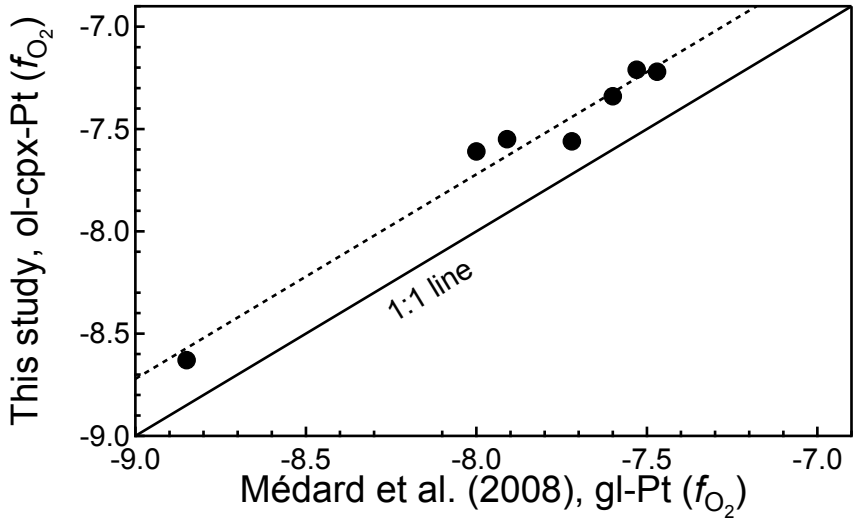

Figure 4.4: Glass-Pt f_{O_2} determination method (*Médard et al.*, 2008) compared to this study's olivine-clinopyroxene-Pt f_{O_2} determination method. The offset between the dashed line fit through the olivine-clinopyroxene-Pt data and the 1:1 line is ~0.30 log units of oxygen fugacity.

4.4.2 SIMS calibration

Experimental glasses were measured using a calibration based on natural, hydrous basalt standards and a natural Bamble enstatite blank from Aubaud et al. (2007), experimental martian basalts (*Stanley et al.*, 2011), and a blank glass of Humphrey basalt composition. This Humphrey composition blank was vitrified in a Pt-crucible in a vertical Deltech 1-atm furnace at 1350 °C for 15 h. The sample was drop quenched into water to produce a nominally volatile-free glass. Using FTIR determined volatile contents of these standards, we established linear calibration curves for both volatiles:

$$\underset{\text{SIMS}}{\text{C}}(\text{wt\%}) = \frac{(\underset{\text{SIMS}}{\text{C}}/\underset{\text{EMP}}{\text{Si}}) \times \underset{\text{EMP}}{\text{SiO}_2}(\text{wt\%})}{1.67(\pm 0.36)} - 0.0005 \tag{4.11}$$

$$\underset{\text{SIMS}}{\text{H}_2\text{O}}(\text{wt\%}) = \frac{(\underset{\text{SIMS}}{\text{OH}}/\underset{\text{EMP}}{\text{Si}}) \times \underset{\text{EMP}}{\text{SiO}_2}(\text{wt\%})}{7.88(\pm 0.84)} - 0.0130 \tag{4.12}$$

(Fig. 4.5a-b) where $\underset{\text{EMP}}{\text{SiO}_2}$ is the silica content of the glass measured by electron microprobe for

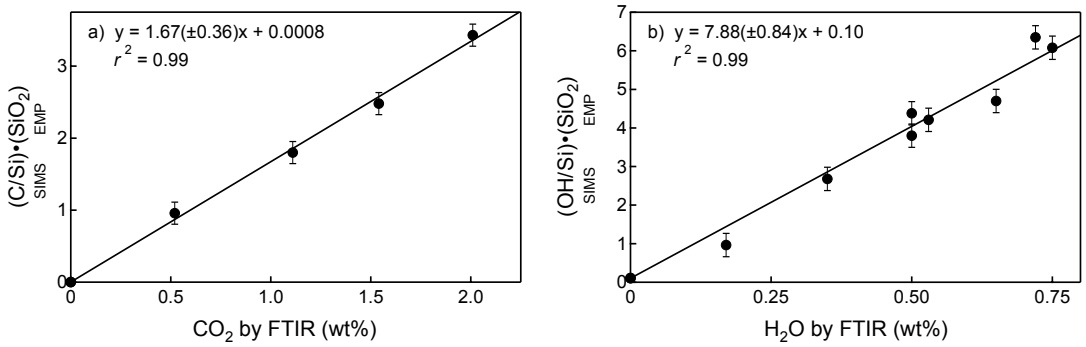

Figure 4.5: FTIR-SIMS calibration curves for a) C and b) H_2O in basalt glass. The ratio observed by the SIMS that is multiplied by SiO_2 contents of the phase analyzed by EMP and compared to FTIR measurements for each standard to create the calibration curve. The uncertainties in SIMS count rates were calculated by averaging the standard deviation on all standard measurements.

each glass in wt%. The C and H_2O backgrounds during SIMS analysis are estimated to be 5 and 130 ppm respectively, derived from 8 measurements of synthetic, drop-quenched Humphrey glass and natural Bamble enstatite (*Aubaud et al.*, 2007) taken over the 5 days of the session. All measurements of unknowns were background corrected after conversion to C_{SIMS} and H_2O_{SIMS} (Eqns. 4.11 and 4.12). The uncertainties in SIMS count rates were calculated by averaging the standard deviation on all standard measurements.

Carbide analyses were calibrated against a Fe_3C standard synthesized in the piston cylinder at 1200 °C and 2 GPa. Fe metal powder (99.9%, Alfa-Aesar) and graphite (reagent grade graphite powder, Carbone of America) were mixed in a Fe_3C stoichiometric proportion in a mortar and pestle for 2.5 h under ethanol and run in a crushable MgO capsule. To insure the structure of the synthesized Fe_3C was accurate, a powder X-ray diffraction (XRD) pattern was collected from a powdered piece of the run product. Carbon contents of carbide droplets were estimated using the average count rates of the Fe_3C standard and assuming it has a stoichiometric C/Fe ratio (C/Fe weight ratio = 0.0717). Count rates on unknowns were then converted to C wt% using this relationship.

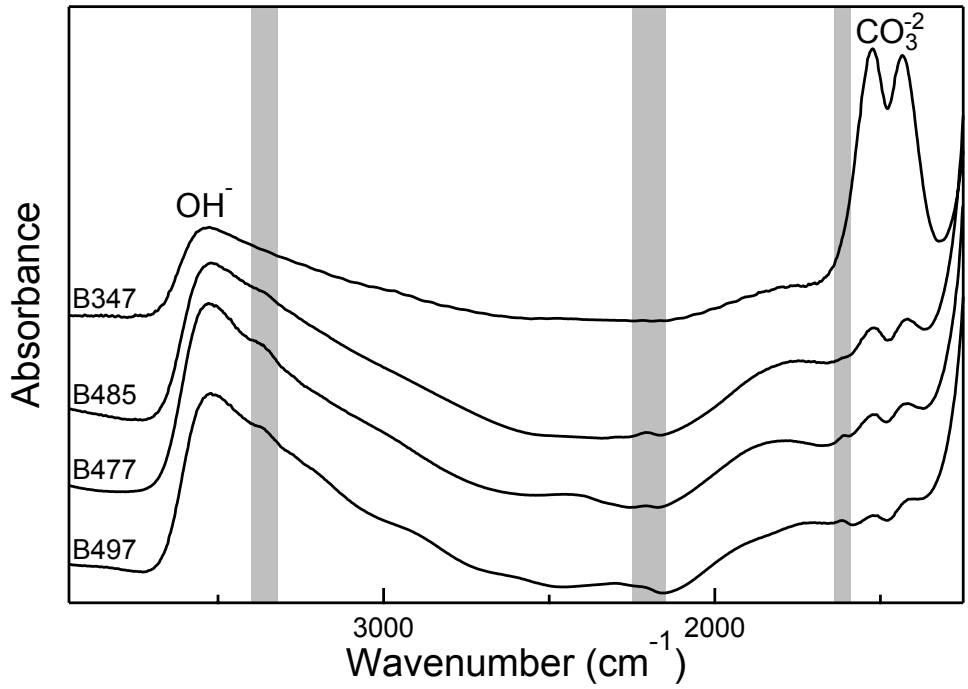

Figure 4.6: FTIR spectra of C-O-H-bearing glasses showing observed OH^- peaks at 3550 cm^{-1} and the variation in CO_3^{2-} doublet heights near 1450 cm^{-1}. Weak peaks at 1615 cm^{-1}, 2205 cm^{-1}, and 3370 cm^{-1} (shaded regions) are discussed in the text and shown in detail in Fig. 4.7. The broad sloping background between 1700 and 2000 cm^{-1} is due to silicate network vibrations and is not representative of dissolved carbonyl. Spectra are normalized to 1 cm to allow visual representation of different volatile concentrations.

4.4.3 C-O-H volatile contents of glasses

FTIR spectra were obtained for all experimental glasses and a representative selection are shown in Fig. 4.6. All samples showed carbonate bands at 1430 and 1520 cm^{-1}, with CO_2 concentrations ranging from 0.0026-0.50 wt% (Table 4.4), and no evidence of molecular CO_2 at 2350 cm^{-1}. For reduced experiments (<IW) carbonate solubilities are very low but remain measurable by using thicker glass chips (200-300 μm). Spectra also have a wide peak at 3550 cm^{-1} indicating the presence of OH^- in the melt and yielding concentrations ranging from 0.26-0.85 wt% (Table 4.4) using the Jendrzejewski et al. (1996) molar absorption coefficient at the O-H bond fundamental stretching frequency. Reduced experiments show additional peaks not seen in oxidized samples (Table 4.5).

The narrow band at 1615 cm^{-1} (Fig. 4.7a) is outside the range attributed to metal carbonyl complexes (1700-2180 cm^{-1}, *Socrates*, 2001). It is unlikely to be a shifted molecular H_2O bending peak (originally at 1630 cm^{-1}) because at such low total water contents there will not be detectable amounts of molecular H_2O. Multiple C-O-H species are possibilities for this peak, as C=O bonds can vibrate in this region in more complex molecules. Carboxylic acid salts,

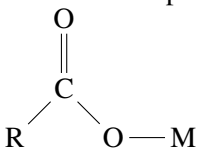

where M is a cation in the melt and R refers to H or C-H groups, unidentate carboxylate complexes

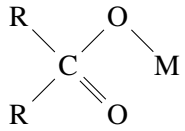

and amides

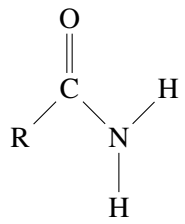

all have a band in the region (*Socrates*, 2001). Each species is weak in Raman, and our spectra show no discernable peak in this region, further complicating efforts at distinguishing the species.

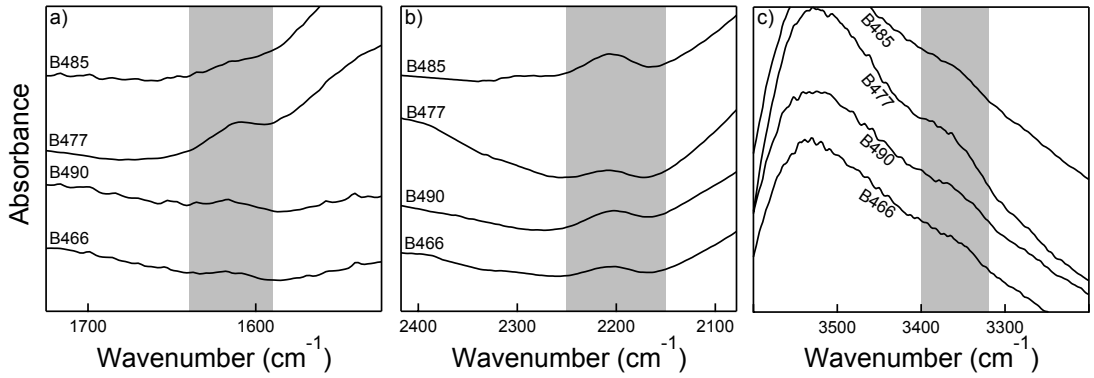

Figure 4.7: FTIR spectra of regions showing weak peaks at a) 1615 cm^{-1} associated with C=O vibrations in amides, b) 2205 cm^{-1} associated with C=O vibrations in the Fe-carbonyl $[Fe(CO)_6]^{2+}$, and c) 3370 cm^{-1} associated with N-H vibrations in amides. Spectra are arranged vertically by decreasing amount of excess C and normalized to 1 cm to allow visual representation of difference in volatile concentrations.

The narrow peak at 2205 cm^{-1} (Fig. 4.7b) is associated with the dissolved Fe-carbonyl $[Fe(CO)_6]^{2+}$ (*Bley et al.*, 1997). Though outside the traditional range of carbonyls, the large number of CO ligands and positive charge both increase the stretching frequency of the C=O bond. Surprisingly, no Fe-carbonyl peak is detected in Raman spectra, whereas Wetzel et al. (submitted to *Science*) found $Fe(CO)_5$ in both FTIR and Raman at 2110 cm^{-1}.

The wide, weak peak at 3370 cm^{-1} (Fig. 4.7c) was attributed to N-H bonds when observed in Raman by Kadik et al. (2011). Taken in tandem with the C=O band at 1615 cm^{-1}, we provisionally interpret both FTIR peaks as associated with vibrations in amides.

CO_2 contents determined by FTIR are plotted versus $\log f_{O_2}$ relative to the IW buffer in Fig. 4.8. Experiments show a linear relationship between $\log f_{O_2}$ and CO_2 content in a graphite-saturated system, confirming earlier models that an order of magnitude change in oxygen fugacity resulting in an order of magnitude change in CO_2 solubility (*Holloway et al.*, 1992; *Holloway*, 1998; *Hirschmann and Withers*, 2008). A more detailed analysis of these results is provided in the Comparison to previous studies section below.

Raman spectra of all glasses show an asymmetrical broad band between 3350 and 3650 cm^{-1} associated with OH^- ions and H_2O molecules (Fig. 4.9). Several experiments show weak peaks near 1350 and 1580 cm^{-1} associated with graphite (*Reich and Thomsen*, 2004), which could represent contamination from the graphite inner capsule during polishing. Vibrations for other C-O-H peaks were not observed in any of the synthesized experimental glasses.

Table 4.5: Excess C and FTIR peak observations.

Exp #	P, T (GPa, °C)	Metal phase	f_{O_2} ΔIW	Excess C (wt%)	1615 peak	2205 peak	3370 peak
B330	1.0, 1355	Pt	2.28	-	×	×	×
B332	1.0, 1355	Pt	2.21	-	×	×	×
B347	1.0, 1355	Pt	2.09	-	×	×	×
B349	1.0, 1355	Pt	2.34	-	×	×	×
B361	1.0, 1355	Pt	2.20	-	×	×	×
B368	1.0, 1340	Pt	1.97	-	×	×	×
B372	1.0, 1355	Pt	1.91	-	×	×	×
B379	1.0, 1355	Pt	1.90	-	×	×	×
A877	1.0, 1355	Pt	2.00	-	×	×	×
B412	1.0, 1340	Pt	2.16	-	×	×	×
B420	1.0, 1340	Pt	1.11	0.0523	×	×	×
B441	1.0, 1340	Pt	1.73	0.0704	×	✓	✓
B442	1.0, 1340	Pt	2.18	-	×	×	×
B465	1.0, 1340	Pt	0.89	0.0685	×	✓	×
B466	1.0, 1340	carbide	-0.77	0.0135	✓	✓	✓
B477	2.0, 1500	Pt	-0.02	0.0350	✓	✓	✓
B485	2.0, 1500	Pt	0.39	0.0526	×	✓	✓
B486	1.0, 1400	Pt	1.01	0.0531	×	×	×
B489	2.0, 1500	carbide	-0.86	0.0156	✓	✓	✓
B490	1.0, 1400	carbide	-0.82	0.0199	✓	✓	✓
B491	3.0, 1600	carbide	-0.92	0.0131	✓	✓	✓
B492	1.0, 1400	carbide	-0.87	0.0105	✓	~	✓
B493	2.0, 1500	carbide	-0.87	0.0078	✓	✓	✓
B494	3.0, 1600	carbide	-0.65	0.0089	✓	✓	✓
B495	1.0, 1400	Pt	-0.71	0.0181	✓	~	✓
B497	2.0, 1500	Pt	-0.27	0.0320	✓	✓	✓

Experiments without Excess C value were not analyzed by SIMS (Table 4.6).
FTIR peaks: ✓strong, ~ barely detected, × not detected.

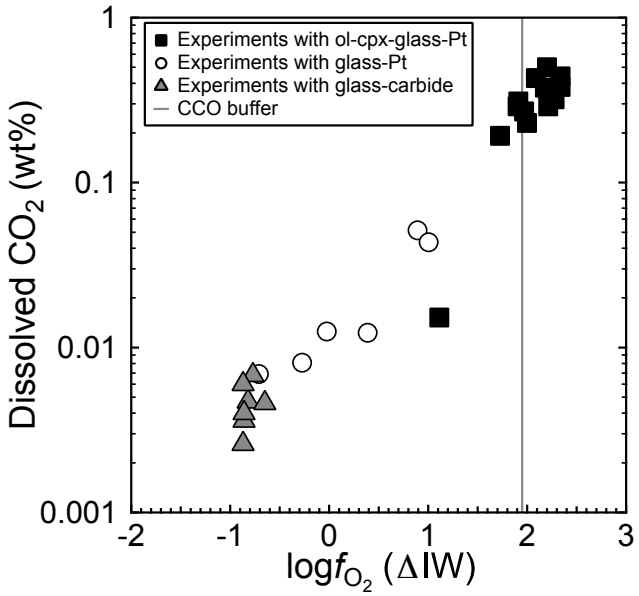

Figure 4.8: Oxygen fugacity relative to the IW buffer compared to dissolved CO_2 analyzed by FTIR. Oxygen fugacity was determined by glass-Pt or glass-carbide method. CCO buffer plotted for visual reference, and defined at 1350 °C and 1.0 GPa using Frost and Wood (1997). IW buffer is described using O'Neill and Pownceby (1993) with the pressure dependence of Eugster and Wones (1962).

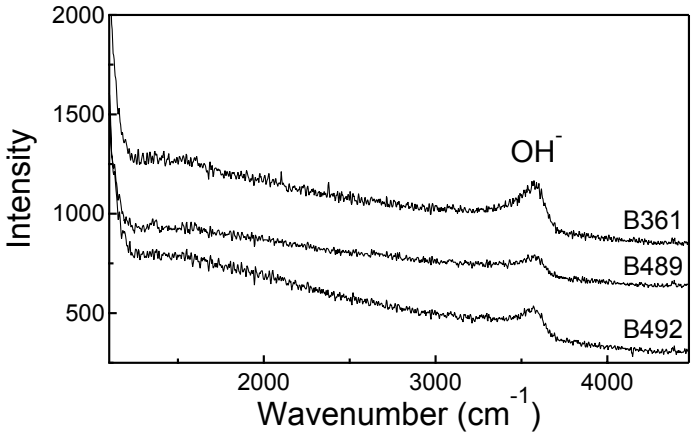

Figure 4.9: Representative Raman spectra of glasses showing region associated with volatile species. The peak assigned to OH^- is highlighted. No peaks for Fe-carbonyls, amides, or other C-O-H species are present in any Raman spectra.

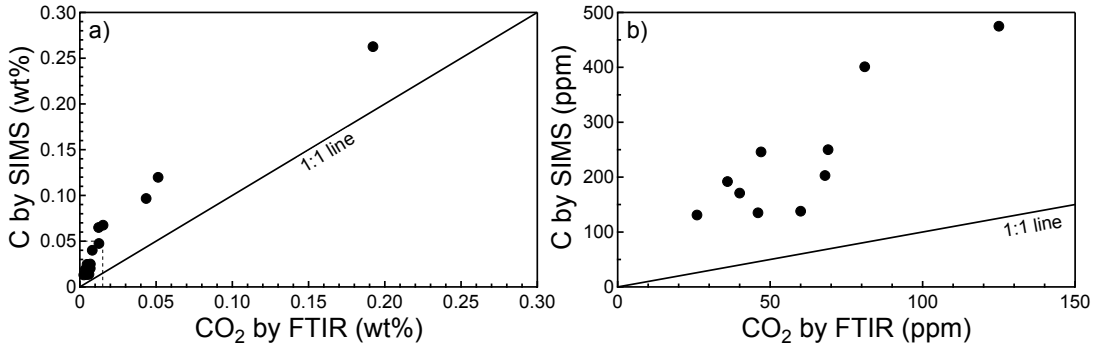

Figure 4.10: CO_2 as determined by FTIR compared to C by SIMS showing increased C contents from SIMS data. b) inset of low concentration region highlighting reduced experiments.

SIMS determinations of C and H_2O contents in glasses are summarized in Table 4.6 and range from 0.0131-0.2626 wt% and 0.29-0.40 wt% respectively. Interestingly, C contents determined by SIMS are consistently higher than C contents determined by FTIR using CO_3^{2-} (Fig. 4.10). This difference, termed excess C, is not constant but varies with total C content (Table 4.6). Excess C correlates with the intensities of peaks 1615, 2205, and 3370 cm^{-1} (Fig. 4.11) suggesting contributions from all three. Intensities of the 1615 cm^{-1} peak correspond particularly well, thereby strengthening our attributing it to the C=O vibration of amides. There is a strong correlation between oxygen fugacity and the appearance of the FTIR peaks for amides and Fe-carbonyls, as they do not appear in more oxidized spectra (Table 4.5). Surprisingly, excess C shows a positive relationship with increasing f_{O_2} (Fig. 4.12), however it is likely that this reflects the combined propagated error in the precision of both SIMS and FTIR analyses of carbon species.

4.4.4 C contents of Fe-C droplets

SIMS-derived C contents of experimental carbides are given in Table 4.7, range from 6.71-8.35 wt%, and agree within error with C calculated by difference from EMP analyses of Fe. The lone exception is B494, as SIMS analyses of this sample produced consistently higher SIMS carbon concentrations (8.35 wt%) relative to EMP results (6.80 wt% C by difference). This could be a result of the Fe-C droplets having more graphite inclusions than other experiments. Experimental carbides plotted on the 2 GPa Fe-C phase diagram by Dasgupta and Walker (2008) confirm that at experimental conditions all of the experiments had coexisting Fe-C melt and

Table 4.6: SIMS analyses of experimental glasses.

Exp #	P, T (GPa, °C)	f_{O_2} ΔIW	$(C/Si)_{SIMS} \cdot SiO_{2\,EMP}$	C_{SIMS} (wt%)	(s.d.)	$CO_{2\,FTIR}$ (wt%)	$C_{SIMS} - CO_{2\,FTIR}$ (wt%)	$(OH/Si)_{SIMS} \cdot SiO_{2\,EMP}$	H_2O_{SIMS} (wt%)	H_2O_{FTIR} (wt%)
B420	1.0, 1340	1.11	0.1134	0.0675	0.0081	0.0152	0.0523	3.39	0.42	0.53
B441	1.0, 1340	1.73	0.4390	0.2626	0.0298	0.1922	0.0704	3.41	0.42	0.49
B465	1.0, 1340	0.89	0.2007	0.1198	0.0004	0.0513	0.0685	3.59	0.44	0.35
B466	1.0, 1340	-0.77	0.0347	0.0203	0.0002	0.0068	0.0135	2.91	0.36	0.26
B477	2.0, 1500	-0.02	0.0801	0.0475	0.0008	0.0125	0.0350	3.16	0.39	0.47
B485	2.0, 1500	0.39	0.1091	0.0649	0.0032	0.0123	0.0526	3.50	0.43	0.39
B486	1.0, 1400	1.01	0.1620	0.0966	0.0117	0.0435	0.0531	3.15	0.39	0.52
B489	2.0, 1500	-0.86	0.0329	0.0192	0.0003	0.0036	0.0156	3.60	0.44	0.40
B490	1.0, 1400	-0.82	0.0418	0.0246	0.0007	0.0047	0.0199	2.83	0.35	0.29
B491	3.0, 1600	-0.92	0.0293	0.0171	0.0006	0.0040	0.0131	3.45	0.42	0.36
B492	1.0, 1400	-0.87	0.0226	0.0131	0.0004	0.0026	0.0105	3.57	0.44	0.35
B493	2.0, 1500	-0.87	0.0239	0.0138	0.0001	0.0060	0.0078	3.37	0.42	0.36
B494	3.0, 1600	-0.65	0.0233	0.0135	0.0002	0.0046	0.0089	3.28	0.40	0.38
B495	1.0, 1400	-0.71	0.0425	0.0250	0.0007	0.0069	0.0181	3.13	0.38	0.54
B497	2.0, 1500	-0.27	0.0677	0.0401	0.0045	0.0081	0.0320	3.14	0.39	0.45

Reported results are the average of 3 analyses taken in the same session. C_{SIMS} and H_2O_{SIMS} values are blank corrected for 0.0005 and 0.0130 wt% respectively.

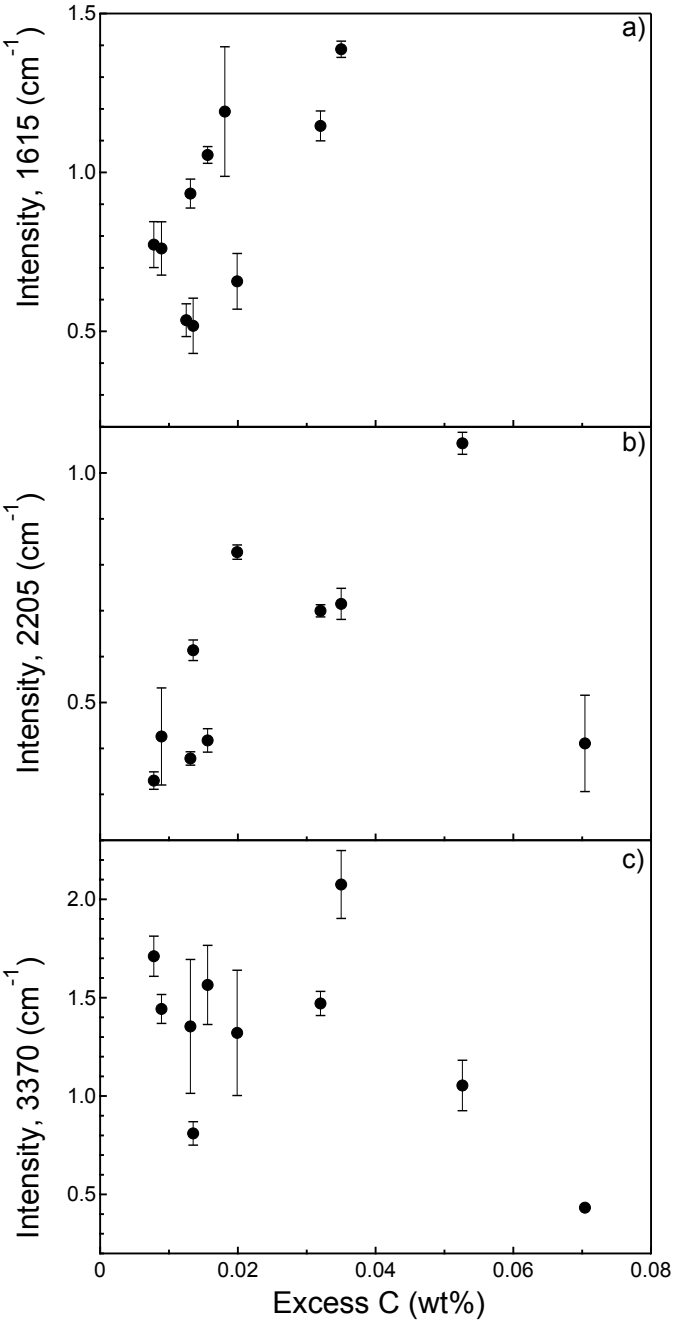

Figure 4.11: Excess C compared to FTIR peak intensities of a) the amide C=O vibration peak at 1615 cm^{-1}, b) the Fe-carbonyl C=O vibration peak at 2205 cm^{-1}, and c) the amide N-H vibration peak at 3370 cm^{-1}. Intensities were measured as heights using a straight line baseline through minima to either side of the peaks.

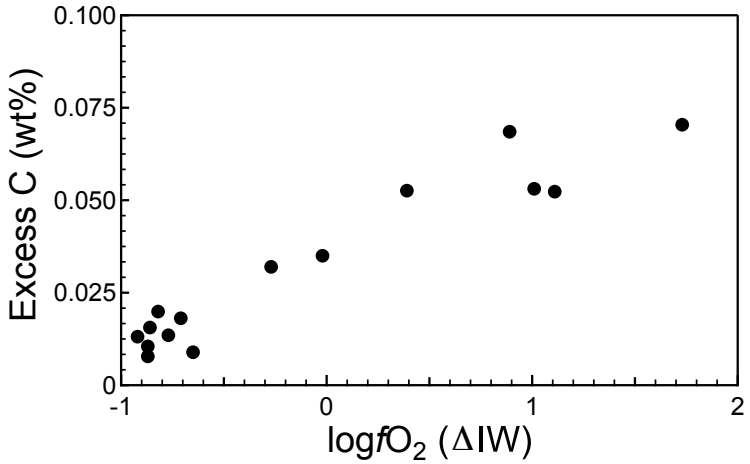

Figure 4.12: Oxygen fugacity relative to IW buffer compared to excess C determined by FTIR and SIMS.

graphite (Fig. 4.13). However, examination of the 5 GPa Fe-C phase diagram (*Wood*, 1993, dashed gray line Fig. 4.13) shows a significantly different slope in the line dividing the fields of liquid Fe-C and graphite + liquid Fe-C. Using the nearly vertical slope reported by Dasgupta and Walker (2008), our experiments would have produced liquids that were more Fe-rich that are measured, suggesting a shallower slope more consistent with the Wood (1993) diagram is preferable.

Oxygen fugacities determined by the glass-carbide method are given in Table 4.4 and shown as open triangles in Fig. 4.8. Carbide-bearing experiments cluster around IW-0.8 and have an average of 46 ppm CO_2 dissolved in the coexisting silicate melts. Using C by difference from Fe analyzed by EMP, instead of C_{SIMS}, to calculate oxygen fugacity causes differences of less than 0.10 log units for all experiments except for B494.

4.5 Applications and discussion

4.5.1 Comparison to previous studies

The concentrations of CO_2 dissolved in graphite-saturated martian basalts vary linearly with oxygen fugacity. Applying our previous model (*Stanley et al.*, 2012) of CO_2 concentrations in graphite-saturated martian basalts to the experimental conditions of this study provides an

Table 4.7: SIMS analyses of experimental carbides.

Exp #	P, T (GPa, °C)	f_{O_2} ΔIW	(C/Fe)$_{SIMS}$	C$_{SIMS}$ (wt%)
B466,1	1.0, 1340	-0.77	2.73E+02	6.76
B466,2	1.0, 1340	-0.77	2.81E+02	6.95
B466,3	1.0, 1340	-0.77	2.88E+02	7.12
B466 Avg.			2.81E+02	6.95
B489,1	2.0, 1500	-0.86	2.73E+02	6.77
B489,2	2.0, 1500	-0.86	2.91E+02	7.19
B489,3	2.0, 1500	-0.86	2.57E+02	6.40
B489,4	2.0, 1500	-0.86	2.60E+02	6.46
B489 Avg.			2.70E+02	6.71
B491,1	3.0, 1600	-0.92	2.60E+02	6.47
B491,2	3.0, 1600	-0.92	2.47E+02	6.16
B491,3	3.0, 1600	-0.92	2.67E+02	6.63
B491,4	3.0, 1600	-0.92	3.01E+02	7.40
B491,5	3.0, 1600	-0.92	2.92E+02	7.20
B491,6	3.0, 1600	-0.92	2.90E+02	7.15
B491 Avg.			2.76E+02	6.84
B492,1	1.0, 1400	-0.87	2.77E+02	6.86
B493,1	2.0, 1500	-0.87	2.58E+02	6.42
B493,2	2.0, 1500	-0.87	2.73E+02	6.76
B493,3	2.0, 1500	-0.87	3.08E+02	7.56
B493,4	2.0, 1500	-0.87	3.00E+02	7.38
B493 Avg.			2.84E+02	7.03
B494,1	3.0, 1600	-0.65	3.45E+02	8.40
B494,2	3.0, 1600	-0.65	3.30E+02	8.07
B494,3	3.0, 1600	-0.65	3.39E+02	8.26
B494 Avg.			3.38E+02	8.35

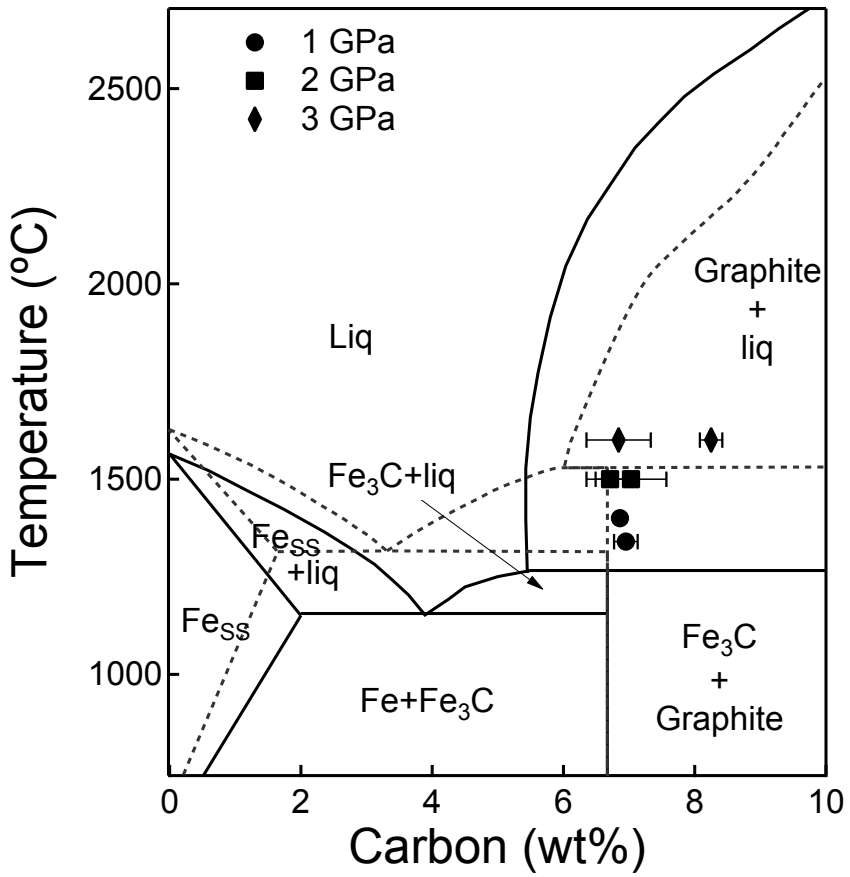

Figure 4.13: SIMS carbide results plotted on the Fe-C phase diagram at 2 GPa after Dasgupta and Walker (2008, solid black line) and 5 GPa after Wood (1993, dashed gray line).

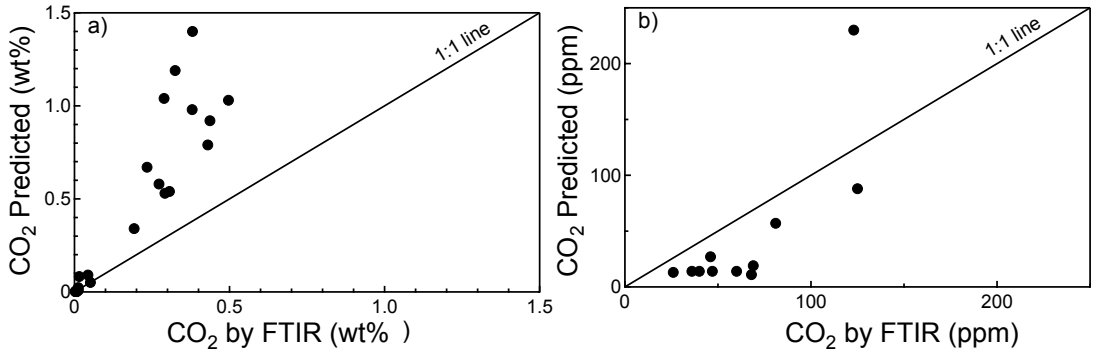

Figure 4.14: CO_2 from FTIR compared to CO_2 predicted using the Stanley et al. (2012) parameterization for each experiment. b) Inset of low concentration region highlighting reduced experiments.

opportunity to assess the viability of those models. The predicted CO_2 contents of each experiment are given in Table 4.4 and are illustrated in Fig. 4.14. At oxidized conditions experimental CO_2 contents are consistently lower than predicted, while more reduced conditions result in an underprediction of measured CO_2 concentrations. The Stanley et al. (2012) parameterization is valid to less than an order of magnitude at reduced conditions of interest. The underprediction can be explained by the lack of inclusion of other C-O-H species. The good correlation between carbonyl and amides peak intensities with excess C (Fig. 4.11) suggests that a large proportion of the difference can be attributed to these dissolved species. Thus, a significant amount of outgassed C-O-H species were not included in previous work causing the need to reexamination the possibility of a thick greenhouse on early Mars.

4.5.2 Application to martian atmospheric evolution

Our results show that dissolved species such as carbonyl and amide could be a significant source of C fluxes to the martian atmosphere, while methane contributions are likely to be negligible. This corresponds well with work by Ardia et al. (submitted to *Geochimica et Cosmochimica Acta*) that predicted methane contents be no more than 10 ppm at IW, and no more than 1 ppm at IW-1 in graphite-saturated martian basalts at 1 GPa with a total H content of 2000 ppm. Such low concentrations are likely insufficient to stabilize liquid water on the ancient martian surface as the primary greenhouse gas, despite its strength as a greenhouse gas (20 times the stronger than CO_2; *Pavlov et al.*, 2000).

An atmosphere produced by degassing of magmas similar to this study would initially consist of CO and H_2O with minor CH_4 and H_2, as dissociation of dissolved Fe-carbonyl produces C-O-H gases through the following reactions:

$$H_2O + [Fe(CO)_6]^{2+} \rightleftharpoons FeO + H_2 + 6\,CO \tag{4.13}$$

$$3\,H_2 + CO \rightleftharpoons H_2O + CH_4. \tag{4.14}$$

Dissociation of dissolved amides would produce a similar atmosphere with additional N-bearing species. In the terrestrial atmosphere, CO plays a key role in climate forcing by affecting methane abundances through reaction with radicals that would otherwise destroy CH_4 molecules (*Daniel and Solomon*, 1998). It is likely that CO could act in the same manner in the martian atmosphere. Additionally, the reactions in the terrestrial atmosphere that oxidize CO to CO_2 could also be active on Mars thereby further strengthening the greenhouse atmosphere. The resulting atmosphere would be more C-O-H-rich than previously modeled, even though the exact quantity of each gas comprising the atmosphere is unclear.

Experiments suggest that the Humphrey source region was near 1350±50 °C and 1.2±0.1 GPa (*Filiberto et al.*, 2008) whereas that of martian meteorite Yamato 980459 (Y 980459) was near 1540±10 °C and 1.2±0.5 GPa (*Musselwhite et al.*, 2006). If Humphrey magmas have total C concentrations similar to experiments such as B465 (1340 °C, 1 GPa, IW+0.89), then dissolved C contents could be more than double those predicted using only CO_2, 1200 ppm vs. 515 ppm respectively (Tables 4.6 and 4.4). Hotter source region temperatures attributed to Y 980459 increase the CO_2 solubility by 120% relative to Humphrey (*Stanley et al.*, 2012). Assuming the same relationship, total C contents of Y 980459 at ~IW+1 would be 2640 ppm.

Applying these results to the cumulative igneous flux model of Hirschmann and Withers (2008) allows the calculation of the volcanogenic contribution of dissolved C-O-H species to the martian atmosphere. If martian magmatism were similar to Humphrey basalt, then the cumulative volcanogenic carbon output on Mars since 4.5 Ga could have generated 0.60 bars of atmosphere. If such sources were similar to Y 980459, the total volcanogenic flux of carbon would produce 1.33 bars of atmosphere. Both scenarios result in significantly more total carbon outgassed to the martian atmosphere than previous predicted using only CO_2 (*Hirschmann and Withers*, 2008; *Stanley et al.*, 2011, 2012). It is likely that the combined direct and indirect

greenhouse effects of CO, CO_2, H_2O, and minor amounts of CH_4 in such an atmosphere could create the required thick greenhouse and result in climate capable of stabilizing liquid water on the ancient martian surface.

4.6 Conclusions

Experimental determinations of C-O-H volatile concentrations in synthetic martian basalts as a function of oxygen fugacity with graphite present are used to model the evolution of the early martian atmosphere.

1. CO_2 solubilities change by one order of magnitude with an order of magnitude change in oxygen fugacity, as predicted by previous work. In a reduced martian mantle (between IW and IW+1), this leads to insufficient dissolved CO_2 to produce a thick martian greenhouse in the late Noachian.

2. Other reduced species, such as Fe-carbonyls and amides, are detected in reduced graphite-saturated martian basalts. An atmosphere produced by degassing of magmas similar to this study would be richer in C-O-H species than previously modeled using only CO_2 and could create a much warmer climate that stabilizes liquid water on the ancient martian surface.

3. Calculating oxygen fugacity using coexisting olivine, pyroxene, and FePt alloys shows good correlation with previous work using coexisting melt and FePt alloys. This should be considered as an alternate method of post-experiment f_{O_2} determination in graphite-saturated high-pressure experiments.

4.A Supplementary information

4.A.1 Making the starting materials

A reduced and carbonated synthetic Humphrey starting material produced for a previous study was used in these experiments. The starting material was placed into a zirconia capsule and decarbonated by heating at a rate of 100 °C/h to 1000 °C and held for 24 h. The powder was then ground to a fine powder. To ensure homogeneity this process was repeated. An

Table 4.A.1: Starting material compositions calculated from initial weight, reported in wt%.

Starting	Humphrey basalt				Fe	Pt	
material name	Oxidized	Reduced	Olivine	Pigeonite	metal	metal	Total
100-0	69.91	-	15.07	15.02	-	-	100
75-25	52.77	17.25	15.66	14.31	-	-	100
50-50	34.61	35.39	14.80	15.20	-	-	100
25-75	18.52	51.12	16.06	14.30	-	-	100
12.5-87.5	8.88	61.57	14.89	14.66	-	-	100
0-100	-	69.66	15.48	14.86	-	-	100
0+Fe0(2.6)[a]	-	68.11	14.75	14.58	2.56	-	100
0+Fe0(4.0)[a]	-	62.59	14.01	14.09	4.16	5.14	100
0+Fe0(8.0)[a]	-	64.39	14.02	13.06	8.53	-	100
0+Fe0(2.5)*	-	92.43	-	-	2.49	5.08	100
0+Fe0(8.0)*	-	91.88	-	-	8.12	-	100
0+Fe0(8.0)*+Pt	-	87.50	-	-	7.73	4.76	100

[a] - starting materials created by mixing 0-100 and some amount of Fe metal. 0+Fe0(8.0)*+H_2O was created by adding ~20 mL of deionized water to a graphite capsule and then filling the capsule with 0+Fe0(8.0)*.

oxidized Humphrey starting material was created from an amount of this decarbonated, reduced Humphrey. Heating at 1000 °C in a horizontal furnace for 12 h in a compressed air gas stream oxidized this powder.

To enable precipitation of olivine and pigeonite from the melt, the Humphrey starting material was mixed with varying amounts of olivine and pigeonite, whose compositions were taken from the normalized average of olivine and pigeonite compositions measured by Filiberto et al. (2008) in their 1300 and 1350 °C experiments. The olivine composition was calculated without trace amounts of TiO_2, Na_2O, and K_2O, while the pigeonite composition was calculated without K_2O. P_2O_5 was added as ammonium-orthophosphate monohydrate [$(NH_4)_2HPO_4$] (98.0%, Alfa Aesar) to two separate initial mixture of trace elements including MnO, TiO_2, and diopside powder. The trace mixtures were ground in a mortar and pestle under ethanol for 45 min, and heated in Pt crucibles for 5 h at 300 °C to remove volatile components. The resulting powders were then mixed with other oxides and mineral powders to achieve the desired olivine and pigeonite compositions. Starting material compositions, calculated from initial weight, are given in Table 4.A.1.

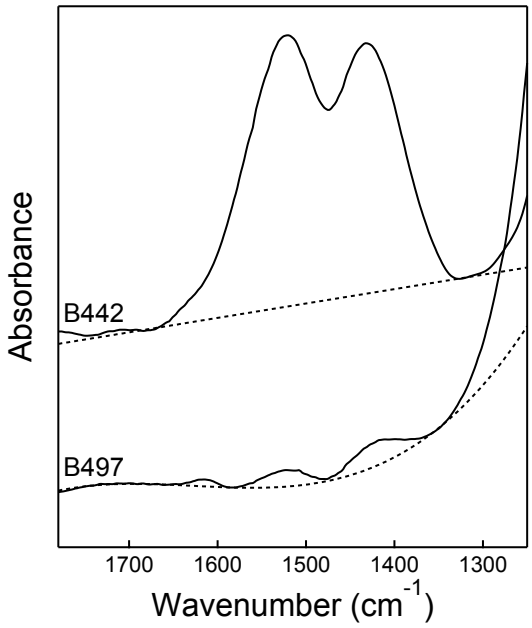

Figure 4.A.1: Representative FTIR spectra of experimental glasses showing fits to remove baselines used to quantify high intensity (straight line) and low intensity (fourth order polynomial) CO_3^{2-} peaks.

4.A.2 Fitting the FTIR spectra

The accuracy of any FTIR determination depends on the choice of baseline and the consistent application of that baseline without bias. This study focuses on the CO_3^{2-} ν_3 doublet near 1500 cm^{-1} with CO_2 solubilities spanning two orders of magnitude. As a result, two baselines have been employed to measure the range of intensities observed in the carbonate doublet. For the more intense carbonate doublets (top spectra in Fig. 4.A.1), the integrated absorption intensity was obtained by subtracting a linear baseline that was fit by least squares minimization to the minima to either side of the doublet.

For very low intensity carbonate doublets (bottom spectra in Fig. 4.A.1), the integrated absorption intensity was obtained by subtracting a fourth order polynomial that was fit by least squares minimization to the minima to either side of the doublet. An interactive fitting routine was also applied to very low intensity carbonate doublets to fit a cubic spline through six points, with three nodes positioned below and three above the frequency range of the region. This is functionally equivalent to fitting a cubic curve through a point either side of the region of interest and specifying the derivatives at those points. Results using the spline method produced slightly

elevated CO_2 contents and it was judged that using fourth order polynomial resulting in a more realistic baseline for the entire doublet. It is our hope that, while this distinction is subjective, the consistent application of one baseline will allow the comparison of spectra fit with the same method.

Bibliography

Adjaoud, O., G. Steinle-Neumann, and S. Jahn (2008), Mg_2SiO_4 liquid under high pressure from molecular dynamics, *Chemical Geology*, *256*(3-4), 185–192.

Agee, C. B., and D. S. Draper (2004), Experimental constraints on the origin of martian meteorites and the composition of the martian mantle, *Earth and Planetary Science Letters*, *224*(3-4), 415–429.

Ardia, P., A. C. Withers, and M. M. Hirschmann (2011), Methane solubility under reduced conditions in a haplobasaltic liquid, in *Lunar Planet. Sci. XLII*, p. 1659, Lunar Planet. Inst.

Aubaud, C., E. H. Hauri, and M. M. Hirschmann (2004), Hydrogen partition coefficients between nominally anhydrous minerals and basaltic melts, *Geophysical Research Letters*, *31*, L20,611.

Aubaud, C., A. C. Withers, M. M. Hirschmann, Y. Guan, L. Leshin, S. J. Mackwell, and D. R. Bell (2007), Intercalibration of FTIR and SIMS for hydrogen measurements in glasses and nominally anhydrous minerals, *American Mineralogist*, *92*, 811–828.

Baker, V., S. Maruyama, and J. Dohm (2007), Tharsis superplume and the geological evolution of early Mars, in *Superplumes: Beyond Plate Tectonics*, edited by D. Yuen, S. Maruyama, S.-I. Karato, and B. Windley, pp. 507–523, Springer.

Behrens, H., S. Ohlhorst, F. Holtz, and M. Champenois (2004), CO_2 solubility in dacitic melts equilibrated with H_2O-CO_2 fluids: Implications for modeling the solubility of CO_2 in silicic melts, *Geochimica et Cosmochimica Acta*, *68*(22), 4687–4703.

Behrens, H., V. Misiti, C. Freda, F. Vetere, R. E. Botcharnikov, and P. Scarlato (2009), Solubility

of H_2O and CO_2 in ultrapotassic melts at 1200 and 1250 °C and pressure from 50 to 500 MPa, *American Mineralogist*, *94*(1), 105–120.

Bertka, C. M., and Y. W. Fei (1997), Mineralogy of the martian interior up to core-mantle boundary pressures, *Journal of Geophysical Research-Solid Earth*, *102*(B3), 5251–5264.

Bertka, C. M., and J. R. Holloway (1994), Anhydrous partial melting of an iron-rich mantle II: Primary melt compositions at 15 kbar, *Contributions to Mineralogy and Petrology*, *115*(3), 323–338.

Blank, J. G., and R. A. Brooker (1994), Experimental studies of carbon dioxide in silicate melts: Solubility, speciation, and stable carbon isotope behavior, in *Volatiles in Magmas*, vol. Reviews in Mineralogy 30, edited by M. R. Carroll and J. R. Holloway, pp. 157–186, Mineralogical Society of America, Washington, D.C.

Bley, B., H. Willner, and F. Aubke (1997), Synthesis and spectroscopic characterization of Hexakis(carbonyl)iron(II) Undecafluorodiantimonate(V), $[Fe(CO)_6][Sb_2F_{11}]_2$, *Inorganic Chemistry*, *36*, 158–160.

Blinova, A., and C. D. K. Herd (2009), Experimental study of polybaric REE partitioning between olivine, pyroxene and melt of the Yamato 980459 composition: Insights into the petrogenesis of depleted shergottites, *Geochimica et Cosmochimica Acta*, *73*, 3471–3492.

Boehler, R., N. Von Bargen, and A. Chopelas (1990), Melting, thermal expansion, and phase transitions of iron at high pressures, *Journal of Geophysical Research-Solid Earth and Planets*, *95*, 21,731–21,736.

Boon, J. A., and W. S. Fyfe (1972), The coordination number of ferrous ions in silicate glasses, *Chemical Geology*, *10*, 287–298.

Borg, L. E., and D. S. Draper (2003), A petrogenetic model for the origin and compositional variation of the martian basaltic meteorites, *Meteoritics and Planetary Science*, *38*(12), 1713–1731.

Borg, L. E., L. E. Nyquist, L. A. Taylor, H. Wiesmann, and C. Y. Shih (1997), Constraints on martian differentiation processes from Rb-Sr and Sm-Nd isotopic analyses of the basaltic shergottite QUE 94201, *Geochimica et Cosmochimica Acta*, *61*(22), 4915–4931.

Botcharnikov, R., M. Freise, F. Holtz, and H. Behrens (2005), Solubility of C-O-H mixtures in natural melts: New experimental data and application range of recent models, *Annals of Geophysics*, *48*(4-5), 633–646.

Botcharnikov, R. E., H. Behrens, and F. Holtz (2006), Solubility and speciation of C-O-H fluids in andesitic melt at T=1100-1300 °C and P=200 and 500 MPa, *Chemical Geology*, *229*(1-3), 125–143.

Boynton, W. V., D. W. Ming, S. P. Kounaves, S. M. M. Young, R. E. Arvidson, M. H. Hecht, J. Hoffman, P. B. Niles, D. K. Hamara, R. C. Quinn, P. H. Smith, B. Sutter, D. C. Catling, and R. V. Morris (2009), Evidence for calcium carbonate at the Mars Phoenix landing site, *Science*, *325*(5936), 61–64.

Brand, R. A. (1987), Improving the validity of hyperfine field distributions from magnetic alloys, part I: Unpolarized source, *Nuclear Instruments and Methods in Physics Research B*, *28*, 398–405.

Brey, G. P., L. N. Kogarko, and I. D. Ryabchikov (1991), Carbon-dioxide in kimberlitic melts, *Neues Jahrbuch fur Mineralogie-Monatshefte*, *4*, 159–168.

Bridges, J. C., and P. H. Warren (2006), The SNC meteorites: Basaltic igneous processes on Mars, *Journal of the Geological Society*, *163*, 229–251.

Brooker, R. A., S. C. Kohn, J. R. Holloway, P. F. McMillan, and M. R. Carroll (1999), Solubility, speciation and dissolution mechanisms for CO_2 in melts on the $NaAlO_2$-SiO_2 join, *Geochimica et Cosmochimica Acta*, *63*(21), 3549–3565.

Brooker, R. A., S. C. Kohn, J. R. Holloway, and P. F. McMillan (2001a), Structural controls on the solubility of CO_2 in silicate melts part I: Bulk solubility data, *Chemical Geology*, *174*(1-3), 225–239.

Brooker, R. A., S. C. Kohn, J. R. Holloway, and P. F. McMillan (2001b), Structural controls on the solubility of CO_2 in silicate melts part II: IR characteristics of carbonate groups in silicate glasses, *Chemical Geology*, *174*(1-3), 241–254.

Brown, L. L., and J. F. Kasting (1993), A carbon dioxide/methane greenhouse atmosphere on early Mars, in *Workshop on Early Mars: How Warm and How Wet?*, vol. LPI Technical

Report 93-03 Part 1, edited by S. W. Squyres and J. F. Kasting, p. 3, Lunar and Planetary Institute, Houston.

Bullock, M. A., and J. M. Moore (2007), Atmospheric conditions on early Mars and the missing layered carbonates, *Geophysical Research Letters*, *34*(19), L19,201.

Campbell, A. J., L. Danielson, K. Righter, C. T. Seagle, Y. B. Wang, and V. B. Prakapenka (2009), High pressure effects on the iron-iron oxide and nickel-nickel oxide oxygen fugacity buffers, *Earth and Planetary Science Letters*, *286*(3-4), 556–564.

Carr, M. H. (1999), Retention of an atmosphere on early Mars, *Journal of Geophysical Research-Planets*, *104*(E9), 21,897–21,909.

Chevrier, V., F. Poulet, and J. P. Bibring (2007), Early geochemical environment of Mars as determined from thermodynamics of phyllosilicates, *Nature*, *448*(7149), 60–63.

Cormier, L., and G. J. Cuello (2011), Mg coordination in a $MgSiO_3$ glass using neutron diffraction coupled with isotopic substitution, *Physical Review B*, *83*(22), 224,204.

Craddock, R. A., and R. Greeley (1995), Estimates of the amount and timing of gases released into the martian atmosphere from volcanic eruptions, in *Lunar Planet. Sci. XXVI*, pp. 287–288, Lunar Planet. Inst.

Craddock, R. A., and R. Greeley (2009), Minimum estimates of the amount and timing of gases released into the martian atmosphere from volcanic eruptions, *Icarus*, *204*(2), 512–526.

Craddock, R. A., and T. A. Maxwell (1993), Geomorphic evolution of the martian highlands through ancient fluvial processes, *Journal of Geophysical Research*, *98*(E2), 3453–3468.

Dalton, H. A., T. G. Sharp, and J. R. Holloway (2007), Investigation of the effects of water on a martian mantle composition, in *Lunar Planet. Sci. XXXVIII*, p. 2102, Lunar Planet. Inst.

Daniel, J. S., and S. Solomon (1998), On the climate forcing of carbon monoxide, *Journal of Geophysical Research-Atmospheres*, *103*, 13,249–13,260.

Dasgupta, R., and M. M. Hirschmann (2006), Melting in the Earth's deep upper mantle caused by carbon dioxide, *Nature*, *440*(7084), 659–662.

Dasgupta, R., and D. Walker (2008), Carbon solubility in core melts in a shallow magma ocean environment and distribution of carbon between the Earth's core and the mantle, *Geochimica et Cosmochimica Acta*, *72*, 4627–4641.

Dasgupta, R., M. M. Hirschmann, and A. C. Withers (2004), Deep global cycling of carbon constrained by the solidus of anhydrous, carbonated eclogite under upper mantle conditions, *Earth and Planetary Science Letters*, *227*, 73–85.

de Koker, N. P., L. Stixrude, and B. B. Karki (2008), Thermodynamics, structure, dynamics, and freezing of Mg_2SiO_4 liquid at high pressures, *Geochimica et Cosmochimica Acta*, *72*(5), 1427–1441.

Dehouck, E., N. Mangold, S. Le Mouelic, V. Ansan, and F. Poulet (2010), Ismenius Cavus, Mars: A deep paleolake with phyllosilicate deposits, *Planetary and Space Science*, *58*(6), 941–946.

di Achille, G., and B. M. Hynek (2010), Ancient ocean on Mars supported by global distribution of deltas and valleys, *Nature Geoscience*, *3*(7), 459–463.

di Achille, G., B. M. Hynek, and M. L. Searls (2009), Positive identification of lake strandlines in Shalbatana Vallis, Mars, *Geophysical Research Letters*, *36*, L14,201.

Dixon, J. E. (1997), Degassing of alkalic basalts, *American Mineralogist*, *82*(3-4), 368–378.

Dixon, J. E., and V. Pan (1995), Determination of the molar absorptivity of dissolved carbonate in basanitic glass, *American Mineralogist*, *80*, 1339–1342.

Dixon, J. E., E. M. Stolper, and J. R. Holloway (1995), An experimental study of water and carbon dioxide solubilities in mid-ocean ridge basaltic liquids part I: Calibration and solubility models, *Journal of Petrology*, *36*(6), 1607–1631.

Dohm, J., V. Baker, S. Maruyama, and R. Anderson (2007), Traits and evolution of the Tharsis superplume, Mars, in *Superplumes: Beyond plate tectonics*, edited by D. Yuen, S. Maruyama, S.-I. Karato, and B. Windley, pp. 523–537, Springer.

Draper, D. S. (2007), Water-undersaturated near-liquidus phase relations of Yamato 980459: Preliminary results, in *Lunar Planet. Sci. XXXVIII*, p. 1447, Lunar Planet. Inst.

Dyar, M. D. (2003), Ferric iron in SNC meteorites as determined by Mössbauer spectroscopy: Implications for martian landers and martian oxygen fugacity, *Meteoritics and Planetary Science*, *38*, 1733–1752.

Dyar, M. D., A. H. Treiman, C. M. Pieters, T. Hiroi, M. D. Lane, and V. O'Connor (2005), MIL 03346, the most oxidized martian meteorite: a first look at spectroscopy, petrography, and mineral chemistry, *Journal of Geophysical Research-Planets*, *110*(E9), E09,005.

Eggler, D. H., and D. Baker (1982), Reduced volatiles in the system C-O-H: implications to mantle melting, fluid formation, and diamond genesis, in *High Pressure Research in Geophysics*, edited by S. Akimoto and M. Manghnani, pp. 237–250, Tokyo: Center for Academic Publications.

Ehlmann, B. L., J. F. Mustard, S. L. Murchie, F. Poulet, J. L. Bishop, A. J. Brown, W. M. Calvin, R. N. Clark, D. J. Des Marais, R. E. Milliken, L. H. Roach, T. L. Roush, G. A. Swayze, and J. J. Wray (2008), Orbital identification of carbonate-bearing rocks on Mars, *Science*, *322*(5909), 1828–1832.

Elkins-Tanton, L. T. (2008), Linked magma ocean solidification and atmospheric growth for Earth and Mars, *Earth and Planetary Science Letters*, *271*(1-4), 181–191.

Eugster, H. P., and D. R. Wones (1962), Stability relations of the ferruginous biotite, annite, *Journal of Petrology*, *3*, 82–125.

Fairèn, A., D. Fernández-Remolar, J. Dohm, V. Baker, and R. Amils (2004), Inhibition of carbonate synthesis in acidic oceans on early Mars, *Nature*, *431*(7007), 423–426.

Farges, F., S. Rossano, Y. Lefrere, M. Wilke, and G. E. Brown (2005), Iron in silicate glasses: A systematic analysis of pre-edge, XANES and EXAFS features, *Physica Scripta*, *T115*, 957–959.

Fassett, C., and J. W. Head (2008), The timing of martian valley network activity: Constraints from buffered crater counting, *Icarus*, *195*, 61–89.

Filiberto, J., and R. Dasgupta (2011), Fe^{2+}-Mg partitioning between olivine and basaltic melts: Applications to genesis of olivine-phyric shergottites and conditions of melting in the martian interior, *Earth and Planetary Science Letters*, *304*(3-4), 527–537.

Filiberto, J., A. H. Treiman, and L. Le (2008), Crystallization experiments on a Gusev Adirondack basalt composition, *Meteoritics and Planetary Science*, *43*, 1137–1146.

Fine, G., and E. Stolper (1985), The speciation of carbon dioxide in sodium aluminosilicate glasses, *Contributions to Mineralogy and Petrology*, *91*(2), 105–121.

Fine, G., and E. M. Stolper (1986), Dissolved carbon dioxide in basaltic glasses: Concentrations and speciation, *Earth and Planetary Science Letters*, *76*(3-4), 263–278.

Fluegel, A. (2007), Global model for calculating room-temperature glass density from the composition, *Journal of the American Ceramic Society*, *90*(8), 2622–2625.

Formisano, V., S. Atreya, T. Encrenaz, N. Ignatiev, and M. Giuranna (2004), Detection of methane in the atmosphere of Mars, *Science*, *306*(5702), 1758–1761.

Frost, D. J., and B. J. Wood (1997), Experimental measurements of the fugacity of CO_2 and graphite/diamond stability from 35 to 77 kbar at 925 to 1650 °C, *Geochimica et Cosmochimica Acta*, *61*(8), 1565–1574.

Gaillard, F., and B. Scaillet (2009), The sulfur content of volcanic gases on Mars, *Earth and Planetary Science Letters*, *279*(1-2), 34–43.

Galoisy, L., G. Calas, and M. A. Arrio (2001), High-resolution XANES spectra of iron in minerals and glasses: Structural information from the pre-edge region, *Chemical Geology*, *174*(1-3), 307–319.

Gellert, R., R. Rieder, J. Bruckner, B. C. Clark, G. Dreibus, G. Klingelhöfer, G. Lugmair, D. W. Ming, H. Wänke, A. Yen, J. Zipfel, and S. W. Squyres (2006), Alpha Particle X-ray Spectrometer (APXS): Results from Gusev crater and calibration report, *Journal of Geophysical Research-Planets*, *111*(E2), E02S05.

Geminale, A., V. Formisano, and M. Giuranna (2008), Methane in martian atmosphere: Average spatial, diurnal, and seasonal behaviour, *Planetary and Space Science*, *56*(9), 1194–1203.

Gendrin, A., N. Mangold, J. P. Bibring, Y. Langevin, B. Gondet, F. Poulet, G. Bonello, C. Quantin, J. Mustard, R. Arvidson, and S. LeMouélic (2005), Sulfates in martian layered terrains: The OMEGA/Mars Express view, *Science*, *307*(5715), 1587–1591.

Gillmann, C., P. Lognonné, and M. Moreira (2011), Volatiles in the atmosphere of Mars: The effects of volcanism and escape constrained by isotopic data, *Earth Planet. Sci. Lett.*, *303*(3-4), 299–309.

Giuli, G., E. Paris, K. U. Hess, D. B. Dingwell, M. R. Cicconi, S. G. Eeckhout, K. T. Fehr, and P. Valenti (2011), XAS determination of the Fe local environment and oxidation state in phonolite glasses, *American Mineralogist*, *96*(4), 631–636.

Grant, J. A., R. P. Irwin, S. A. Wilson, D. Buczkowski, and K. Siebach (2011), A lake in Uzboi Vallis and implications for late Noachian-early Hesperian climate on Mars, *Icarus*, *212*(1), 110–122.

Greeley, R., and B. D. Schneid (1991), Magma generation on Mars: Amounts, rates, and comparisons with Earth, Moon, and Venus, *Science*, *254*(5034), 996–998.

Gross, J., A. H. Treiman, J. Filiberto, and C. D. K. Herd (2011), Primitive olivine-phyric shergottite NWA 5789: Petrography, mineral chemistry, and cooling history imply a magma similar to Yamato 980459, *Meteoritics and Planetary Science*, *46*(1), 116–133.

Grott, M., A. Morschhauser, D. Breuer, and E. Hauber (2011), Volcanic outgassing of CO_2 and H_2O on Mars, *Earth and Planetary Science Letters*, *308*(3-4), 391–400.

Grove, T. L. (1981), Use of FePt alloys to estimate the iron loss problem in 1 atmosphere gas mixing experiments: Theoretical and practical considerations, *Contributions to Mineralogy and Petrology*, *78*, 298–304.

Guignard, M., and L. Cormier (2008), Environments of Mg and Al in MgO-Al_2O_3-SiO_2 glasses: A study coupling neutron and X-ray diffraction and Reverse Monte Carlo modeling, *Chemical Geology*, *256*(3-4), 111–118.

Guillot, B., and N. Sator (2007), A computer simulation study of natural silicate melts. Part II: High pressure properties, *Geochimica et Cosmochimica Acta*, *71*(18), 4538–4556.

Guillot, B., and N. Sator (2011), Carbon dioxide in silicate melts: A molecular dynamics simulation study, *Geochimica et Cosmochimica Acta*, *75*(7), 1829–1857.

Hale, V. P. S., H. Y. McSween, and G. A. McKay (1999), Re-evaluation of intercumulus liquid composition and oxidation state for the Shergotty meteorite, *Geochimica et Cosmochimica Acta*, *63*(9), 1459–1470.

Halevy, I., and J. W. Head (2012), Punctuated volcanism, transient warming and global change in the late Noachian-early Hesperian, in *Lunar Planet. Sci. XLIII*, p. 1908, Lunar Planet. Inst.

Halevy, I., M. T. Zuber, and D. P. Schrag (2007), A sulfur dioxide climate feedback on early Mars, *Science*, *318*(5858), 1903–1907.

Herd, C. D. K. (2003), The oxygen fugacity of olivine-phyric martian basalts and the components within the mantle and crust of Mars, *Meteoritics and Planetary Science*, *38*(12), 1793–1805.

Herd, C. D. K. (2006), Insights into the redox history of the NWA 1068/1110 martian basalt from mineral equilibria and vanadium oxybarometry, *American Mineralogist*, *91*, 1616–1627.

Herd, C. D. K., J. J. Papike, and A. Brearley (2001), Oxygen fugacity of martian basalts from electron microprobe oxygen and TEM-EELS analyses of Fe-Ti oxides, *American Mineralogist*, *86*, 1015–1024.

Herd, C. D. K., L. E. Borg, J. H. Jones, and J. J. Papike (2002), Oxygen fugacity and geochemical variations in the martian basalts: Implications for martian basalt petrogenesis and the oxidation state of the upper mantle of Mars, *Geochimica et Cosmochimica Acta*, *66*(11), 2025–2036.

Hirschmann, M. M. (1991), Thermodynamics of multicomponent olivines and the solution properties of $(NiFeMg)_2SiO_4$ and $(CaMgFe)_2SiO_4$ olivines, *American Mineralogist*, *76*, 1232–1248.

Hirschmann, M. M. (2012), Magma ocean influence on early atmosphere mass and composition, *Earth and Planetary Science Letters*, *341-344*, 48–57.

Hirschmann, M. M., and A. C. Withers (2008), Ventilation of CO_2 from a reduced mantle and consequences for the early martian greenhouse, *Earth and Planetary Science Letters*, *270*(1-2), 147–155.

Holloway, J. R. (1998), Graphite-melt equilibria during mantle melting: Constraints on CO_2 in MORB magmas and the carbon content of the mantle, *Chemical Geology*, *147*(1-2), 89–97.

Holloway, J. R., and J. G. Blank (1994), Application of experimental results to C-O-H species in natural melts, in *Volatiles in Magmas*, vol. Reviews in Mineralogy 30, edited by M. R. Carroll and J. R. Holloway, pp. 187–230, Mineralogical Society of America, Washington, D.C.

Holloway, J. R., V. Pan, and G. Gudmundsson (1992), High-pressure fluid-absent melting experiments in the presence of graphite: Oxygen fugacity, ferric/ferrous ratio and dissolved CO_2, *European Journal of Mineralogy*, *4*(1), 105–114.

Huebner, J. S. (1971), Buffering techniques for hydrostatic systems at elevated pressures, in *Research Techniques for High Pressure and High Temperature*, edited by G. G. Ulmer, pp. 123–177, Springer-Verlag, New York.

Irwin, R. P., A. D. Howard, R. A. Craddock, and J. M. Moore (2005), An intense terminal epoch of widespread fluvial activity on early Mars: 2. Increased runoff and paleolake development, *Journal of Geophysical Research-Planets*, *110*, E12S15.

Jackson, W. E., F. Farges, M. Yeager, P. A. Mabrouk, S. Rossano, G. A. Waychunas, E. I. Solomon, and G. E. Brown Jr. (2005), Multi-spectroscopic study of Fe(II) in silicate glasses: Implications for the coordination environment of Fe(II) in silicate melts, *Geochimica et Cosmochimica Acta*, *69*(17), 4315–4332.

Jakobsson, S. (1997), Solubility of water and carbon dioxide in an icelandite at 1400 °C and 10 kilobars, *Contributions to Mineralogy and Petrology*, *127*, 129–135.

Jakosky, B. M., and R. J. Phillips (2001), Mars' volatile and climate history, *Nature*, *412*(6843), 237–244.

Jakosky, B. M., and E. L. Shock (1998), The biological potential of Mars, the early Earth, and Europa, *Journal of Geophysical Research-Planets*, *103*(E8), 19,359–19,364.

Jayasuriya, K. D., H. S. O'Neill, A. J. Berry, and S. J. Campbell (2004), A Mössbauer study of the oxidation state of Fe in silicate melts, *American Mineralogist*, *89*(11-12), 1597–1609.

Jellinek, A. M., C. L. Johnson, and G. Schubert (2008), Constraints on the elastic thickness, heat flow, and melt production at early Tharsis from topography and magnetic field observations, *Journal of Geophysical Research-Planets*, *113*(E9), E09,004.

Jendrzejewski, N., M. Javoy, and T. Trull (1996), Quantitative measurements of water and carbon concentrations in natural basaltic glasses by infrared spectroscopy. Part II: Water, *Comptes Rendus De L'Academie Des Sciences Serie II Fascicule A-Sciences De La Terre Et Des Planetes*, *322*(9), 735–742.

Johnson, S., M. Mischna, T. L. Grove, and M. T. Zuber (2008), Sulfur-induced greenhouse warming on early Mars, *Journal of Geophysical Research-Planets*, *113*, E08,005.

Kadik, A. A., Y. A. Litvin, V. V. Koltashev, E. B. Kryukova, and V. G. Plotnichenko (2006), Solubility of hydrogen and carbon in reduced magmas of the early Earth's mantle, *Geochemistry International*, *44*(1), 33–47.

Kadik, A. A., N. A. Kurovskaya, Y. A. Ignat'ev, N. N. Kononkova, V. V. Koltashev, and V. G. Plotnichenko (2010), Influence of oxygen fugacity on the solubility of carbon and hydrogen in $FeO-Na_2O-SiO_2-Al_2O_3$ melts in equilibrium with liquid iron at 1.5 GPa and 1400 °C, *Geochemistry International*, *48*(10), 953–960.

Kadik, A. A., N. A. Kurovskaya, Y. A. Ignat'ev, N. N. Kononkova, V. V. Koltashev, and V. G. Plotnichenko (2011), Influence of oxygen fugacity on the solubility of nitrogen, carbon, and hydrogen in $FeO-Na_2O-SiO_2-Al_2O_3$ melts in equilibrium with metallic iron at 1.5 GPa and 1400 °C, *Geochemistry International*, *49*, 429–438.

Karner, J. M., J. J. Papike, C. K. Shearer, G. McKay, L. Le, and P. Burger (2007), Valence state partitioning of Cr and V between pyroxene-melt: Estimates of oxygen fugacity for martian basalt QUE 94201, *American Mineralogist*, *92*(7), 1238–1241.

Kasting, J. F. (1997), Warming early Earth and Mars, *Science*, *276*(5316), 1213–1215.

Kessel, R., J. Beckett, and E. M. Stolper (2001), Thermodynamic properties of the Pt-Fe system, *American Mineralogist*, *86*, 1003–1014.

Kiefer, W. S. (2003), Melting in the martian mantle: Shergottite formation and implications for

present-day mantle convection on Mars, *Meteoritics and Planetary Science*, *38*(12), 1815–1832.

Krasnopolsky, V. A., J. P. Maillard, and T. C. Owen (2004), Detection of methane in the martian atmosphere: Evidence for life?, *Icarus*, *172*(2), 537–547.

Kuramoto, K., and T. Matsui (1996), Partitioning of H and C between the mantle and core during the core formation in the Earth: Its implications for the atmospheric evolution and redox state of early mantle, *Journal of Geophysical Research-Planets*, *101*(E6), 14,909–14,932.

Lange, R. L., and I. S. E. Carmichael (1990), Thermodynamic properties of silicate liquids with emphasis on density, thermal expansion and compressibility, in *Modern Methods of Igneous Petrology: Understanding Magmatic Processes*, vol. Reviews in Mineralogy 24, edited by J. Nicholls and J. K. Russell, pp. 25–64, Mineralogical Society of America, Washington, D.C.

Langevin, Y., F. Poulet, J. P. Bibring, and B. Gondet (2005), Sulfates in the north polar region of Mars detected by OMEGA/Mars express, *Science*, *307*(5715), 1584–1586.

Liebske, C., B. Schmickler, H. Terasaki, B. T. Poe, A. Suzuki, K. Funakoshi, R. Ando, and D. C. Rubie (2005), Viscosity of peridotite liquid up to 13 GPa: Implications for magma ocean viscosities, *Earth and Planetary Science Letters*, *240*(3-4), 589–604.

Luth, R. W. (1999), Carbon and carbonates in the mantle, in *Mantle petrology: field observations and high-pressure experimentation: a tribute to Francis R (Joe) Boyd*, edited by Y. Fei, C. M. Bertka, and B. O. Mysen, pp. 297–316, Geochem Soc Spec Publ 6.

Magnien, V., D. R. Neuville, L. Cormier, B. O. Mysen, V. Briois, S. Belin, O. Pinet, and P. Richet (2004), Kinetics of iron oxidation in silicate melts: a preliminary XANES study, *Chemical Geology*, *213*(1-3), 253–263.

Mangold, N., C. Quantin, V. Ansan, C. Delacourt, and P. Allemand (2004), Evidence for precipitation on Mars from dendritic valleys in the Valles Marineris area, *Science*, *305*(5680), 78–81.

Manning, C. V., C. P. McKay, and K. J. Zahnle (2006), Thick and thin models of the evolution of carbon dioxide on Mars, *Icarus*, *180*(1), 38–59.

McCanta, M. C., M. J. Rutherford, and J. H. Jones (2004), An experimental study of rare Earth element partitioning between a shergottite melt and pigeonite: Implications for the oxygen fugacity of the martian interior, *Geochimica et Cosmochimica Acta*, *68*(8), 1943–1952.

McCanta, M. C., L. Elkins-Tanton, and M. J. Rutherford (2009), Expanding the application of the Eu-oxybarometer to the lherzolitic shergottites and nakhlites: Implications for the oxidation state heterogeneity of the martian interior, *Meteoritics and Planetary Science*, *44*(5), 725–745.

McKay, G., C. Schwandt, T. Mikouchi, E. Koizumi, and J. Jones (2004), Yamato 980459: The most primitive shergottites, in *Lunar Planet. Sci. XXXV*, p. 2154, Lunar Planet. Inst.

McSween, H. Y., M. B. Wyatt, R. Gellert, J. F. Bell, R. V. Morris, K. E. Herkenhoff, L. S. Crumpler, K. A. Milam, K. R. Stockstill, L. L. Tornabene, R. E. Arvidson, P. Bartlett, D. Blaney, N. A. Cabrol, P. R. Christensen, B. C. Clark, J. A. Crisp, D. J. Des Marais, T. Economou, J. D. Farmer, W. Farrand, A. Ghosh, M. Golombek, S. Gorevan, R. Greeley, V. E. Hamilton, J. R. Johnson, B. L. Joliff, G. Klingelhöfer, A. T. Knudson, S. McLennan, D. Ming, J. E. Moersch, R. Rieder, S. W. Ruff, C. Schröder, P. A. De Souza, S. W. Squyres, H. Wänke, A. Wang, A. Yen, and J. Zipfel (2006a), Characterization and petrologic interpretation of olivine-rich basalts at Gusev crater, *Journal of Geophysical Research-Planets*, *111*(E2), E02,510.

McSween, H. Y., S. W. Ruff, R. V. Morris, J. F. Bell, K. Herkenhoff, R. Gellert, K. R. Stockstill, L. L. Tornabene, S. W. Squyres, J. A. Crisp, P. R. Christensen, T. J. McCoy, D. W. Mittlefehldt, and M. Schmidt (2006b), Alkaline volcanic rocks from the Columbia Hills, Gusev Crater, Mars, *Journal of Geophysical Research-Planets*, *111*(E9), E09S91.

Médard, E., C. A. McCammon, J. A. Barr, and T. L. Grove (2008), Oxygen fugacity, temperature reproducibility, and H_2O contents of nominally anhydrous piston-cylinder experiments using graphite capsules, *American Mineralogist*, *93*, 1838–1844.

Michalski, J. R., and P. B. Niles (2010), Deep crustal carbonate rocks exposed by meteor impact on Mars, *Nature Geoscience*, *3*, 751–755.

Monders, A. G., E. Medard, and T. L. Grove (2007), Phase equilibrium investigations of the Adirondack class basalts from the Gusev Plains, Gusev Crater, Mars, *Meteoritics and Planetary Science*, *42*(1), 131–148.

Moore, G. (2008), Interpreting H_2O and CO_2 contents in melt inclusions: Constraints from solubility experiments and modeling, in *Minerals, Inclusions And Volcanic Processes*, vol. Reviews in Mineralogy and Geochemistry 69, edited by K. Putirka and F. Tepley III, pp. 333–361, Mineralogical Society of America.

Morris, R. V., S. W. Ruff, R. Gellert, D. W. Ming, R. E. Arvidson, B. C. Clark, D. C. Golden, K. Siebach, G. Klingelhöfer, C. Schröder, I. Fleischer, A. S. Yen, and S. W. Squyres (2010), Identification of carbonate-rich outcrops on Mars by the Spirit Rover, *Science*, *329*(5990), 421–424.

Mumma, M. J., G. L. Villanueva, R. E. Novak, T. Hewagama, B. P. Bonev, M. A. DiSanti, A. M. Mandell, and M. D. Smith (2009), Strong release of methane on Mars in northern summer 2003, *Science*, *323*(5917), 1041–1045.

Musselwhite, D. S., H. A. Dalton, W. S. Kiefer, and A. H. Treiman (2006), Experimental petrology of the basaltic shergottite Yamato 980459: Implications for the thermal structure of the martian mantle, *Meteoritics and Planetary Science*, *41*(9), 1271–1290.

Mysen, B. O. (2006), The structural behavior of ferric and ferrous iron in aluminosilicate glass near meta-aluminosilicate joins, *Geochimica et Cosmochimica Acta*, *70*(9), 2337–2353.

Mysen, B. O., and S. Yamashita (2010), Speciation of reduced C-O-H volatiles in coexisting fluids and silicate melts determined in-situ to similar to 1.4 GPa and 800 °C, *Geochimica et Cosmochimica Acta*, *74*(15), 4577–4588.

Mysen, B. O., R. J. Arculus, and D. H. Eggler (1975), Solubility of carbon dioxide in melts of andesite, tholeiite, and olivine nephelinite composition to 30 kbar pressure, *Contributions to Mineralogy and Petrology*, *53*(4), 227–239.

Mysen, B. O., D. H. Eggler, M. G. Seitz, and J. R. Holloway (1976), Carbon dioxide solubilities in silicate melts and crystals. Part I. Solubility measurements, *American Journal of Science*, *276*, 455–479.

Mysen, B. O., D. Virgo, and F. A. Seifert (1982), The structure of silicate melts: Implications for chemical and physical properties of natural magmas, *Reviews of Geophysics*, *20*(3), 353–383.

Mysen, B. O., D. Virgo, and F. A. Seifert (1985), Relationships between properties and structure of aluminosilicate melts, *American Mineralogist*, *70*(1-2), 88–105.

Mysen, B. O., M. L. Fogel, P. L. Morrill, and G. D. Cody (2009), Solution behavior of reduced C-O-H volatiles in silicate melts at high pressure and temperature, *Geochimica et Cosmochimica Acta*, *73*(6), 1696–1710.

O'Neill, C., A. Lenardic, A. M. Jellinek, and W. S. Kiefer (2007), Melt propagation and volcanism in mantle convection simulations, with applications for martian volcanic and atmospheric evolution, *Journal of Geophysical Research-Planets*, *112*(E7), E07,003.

O'Neill, H. S. C. (1988), Systems Fe-O and Cu-O: Thermodynamic data for the equilibria Fe-"FeO", Fe-Fe_3O_4, "FeO"-Fe_3O_4, Fe_3O_4-Fe_2O_3, Cu-Cu_2O, and Cu_2O-CuO from emf measurements, *American Mineralogist*, *73*, 470–486.

O'Neill, H. S. C., and M. I. Pownceby (1993), Thermodynamic data from redox reactions at high-temperatures. I. An experimental and theoretical assessment of the electrochemical method using stabilized zirconia electrolytes, with revised values for the Fe-"FeO", Co-CoO, Ni-NiO and Cu-Cu_2O oxygen buffers, and new data for the W-WO_2 buffers, *Contributions to Mineralogy and Petrology*, *114*(3), 296–314.

Palomba, E., A. Zinzi, E. A. Clouds, M. D'Amore, D. Grassi, and A. Maturilli (2009), Evidence for Mg-rich carbonates on Mars from a 3.9 μm absorption feature, *Icarus*, *203*(1), 58–65.

Pan, V., J. R. Holloway, and R. L. Hervig (1991), The pressure and temperature-dependence of carbon dioxide solubility in tholeiitic basalt melts, *Geochimica et Cosmochimica Acta*, *55*(6), 1587–1595.

Papale, P. (1999), Modeling the solubility of a two-component H_2O+CO_2 fluid in silicate liquids, *American Mineralogist*, *84*, 477–492.

Pavlov, A. A., J. F. Kasting, L. L. Brown, K. A. Rages, and R. Freedman (2000), Greenhouse warming by CH_4 in the atmosphere of early Earth, *Journal of Geophysical Research-Planets*, *105*(E5), 11,981–11,990.

Pawley, A. R., J. R. Holloway, and P. F. McMillan (1992), The effect of oxygen fugacity on

the solubility of carbon oxygen fluids in basaltic melt, *Earth and Planetary Science Letters*, *110*(1-4), 213–225.

Pepin, R. O. (1994), Evolution of the martian atmosphere, *Icarus*, *111*(2), 289–304.

Phillips, R. J., M. T. Zuber, S. C. Solomon, M. P. Golombek, B. M. Jakosky, W. B. Banerdt, D. E. Smith, R. M. E. Williams, B. M. Hynek, O. Aharonson, and S. A. Hauck (2001), Ancient geodynamics and global-scale hydrology on Mars, *Science*, *291*(5513), 2587–2591.

Pollack, J. B., J. F. Kasting, S. M. Richardson, and K. Poliakoff (1987), The case for a wet, warm climate on early Mars, *Icarus*, *71*(2), 203–224.

Reich, S., and C. Thomsen (2004), Raman spectroscopy of graphite, *Philosophical Transactions of the Royal Society A*, *362*, 2271–2288.

Righter, K., H. Yang, G. Costin, and R. T. Downs (2008), Oxygen fugacity in the martian mantle controlled by carbon: New constraints from the nakhlite MIL 03346, *Meteoritics and Planetary Science*, *43*(10), 1709–1723.

Righter, K., K. M. Pando, and L. Danielson (2009), Experimental evidence for sulfur-rich martian magmas: Implications for volcanism and surficial sulfur sources, *Earth and Planetary Science Letters*, *288*(1-2), 235–243.

Rossano, S., E. Balan, G. Morin, J. P. Bauer, G. Calas, and C. Brouder (1999), ^{57}Fe Mössbauer spectroscopy of tektites, *Physics and Chemistry of Minerals*, *26*(6), 530–538.

Rossano, S., H. Behrens, and M. Wilke (2008), Advanced analyses of ^{57}Fe Mössbauer data of alumino-silicate glasses, *Physics and Chemistry of Minerals*, *35*(2), 77–93.

Ryan, S., E. J. Dlugokencky, P. P. Tans, and M. E. Trudeau (2006), Mauna Loa volcano is not a methane source: Implications for Mars, *Geophysical Research Letters*, *33*(12), L12,301.

Sack, R. O., and M. S. Ghiorso (1989), Importance of considerations of mixing properties in establishing an internally consistent thermodynamic database: Thermochemistry of minerals in the system Mg_2SiO_4-Fe_2SiO_4-SiO_2, *Contributions to Mineralogy and Petrology*, *102*, 41–68.

Sack, R. O., and M. S. Ghiorso (1994a), Thermodynamics of multicomponent pyroxenes I. Formulation of general model, *Contributions to Mineralogy and Petrology*, *116*, 277–286.

Sack, R. O., and M. S. Ghiorso (1994b), Thermodynamics of multicomponent pyroxenes II. Applications to phase relations in the quadrilateral, *Contributions to Mineralogy and Petrology*, *116*, 287–300.

Sack, R. O., and M. S. Ghiorso (1994c), Thermodynamics of multicomponent pyroxenes III. Calibration of $Fe^{2+}(Mg)_{-1}$, $TiAl(MgSi)_{-1}$, $TiFe^{3+}(MgSi)_{-1}$, $AlFe^{3+}(MgSi)_{-1}$, $NaAl(CaMg)_{-1}$, $Al_2(MgSi)_{-1}$, and $Ca(Mg)_{-1}$ exchange reactions between pyroxenes and silicate melts, *Contributions to Mineralogy and Petrology*, *118*, 271–296.

Sagan, C., and C. Chyba (1997), The early faint Sun paradox: Organic shielding of ultraviolet-labile greenhouse gases, *Science*, *276*(5316), 1217–1221.

Schaefer, M. W. (1993), Aqueous geochemistry on early Mars, *Geochimica et Cosmochimica Acta*, *57*(19), 4619–4625.

Schmidt, M. E., C. M. Schrader, and T. J. McCoy (2011), How oxidized are the Gusev basalts?, in *Lunar Planet. Sci. XLII*, p. 2277, Lunar Planet. Inst.

Shearer, C. K., G. McKay, J. J. Papike, and J. M. Karner (2006), Valence state partitioning of vanadium between olivine-liquid: Estimates of the oxygen fugacity of Y 980459 and application to other olivine-phyric martian basalts, *American Mineralogist*, *91*(1657-1663), 1657–1663.

Shih, C. Y., L. E. Nyquist, H. Wiesmann, C. C. Reese, and K. Misawa (2005), Rb-Sr and Sm-Nd dating of olivine-phyric shergottite Yamato 980459: Petrogenesis of depleted shergottites, *Antarctic Meteorite Research*, *18*, 46–65.

Shimoda, K., T. Nemoto, and K. Saito (2008), Local structure of magnesium in silicate glasses: A ^{25}Mg 3QMAS NMR study, *Journal of Physical Chemistry B*, *112*(22), 6747–6752.

Shirai, N., and M. Ebihara (2004), Chemical characteristics of a martian meteorite, Yamato 980459, *Antarctic Meteorite Research*, *17*, 55–67.

Socrates, G. (2001), *Infrared and Raman Characteristic Group Frequencies: Tables and Charts*, 3rd ed., Wiley and Sons, Chichester, England.

Squyres, S. W., and J. F. Kasting (1994), Early Mars: How warm and how wet?, *Science*, *265*(5173), 744–749.

Squyres, S. W., J. P. Grotzinger, R. E. Arvidson, J. F. Bell, W. M. Calvin, P. R. Christensen, B. C. Clark, J. A. Crisp, W. H. Farrand, K. E. Herkenhoff, J. R. Johnson, G. Klingelhöfer, A. H. Knoll, S. M. McLennan, H. Y. McSween, R. V. Morris, J. W. Rice, R. Rieder, and L. A. Soderblom (2004), In situ evidence for an ancient aqueous environment at Meridiani Planum, Mars, *Science*, *306*(5702), 1709–1714.

Squyres, S. W., O. Aharonson, B. C. Clark, B. A. Cohen, L. S. Crumpler, P. A. de Souza, W. H. Farrand, R. Gellert, J. A. Grant, J. P. Grotzinger, A. F. C. Haldemann, J. R. Johnson, G. Klingelhöfer, K. W. Lewis, R. Li, T. J. McCoy, A. S. McEwen, H. Y. McSween, D. W. Ming, J. M. Moore, R. V. Morris, T. J. Parker, J. W. Rice Jr., S. W. Ruff, M. E. Schmidt, C. Schröder, L. A. Soderblom, and A. S. Yen (2007), Pyroclastic activity at home plate in Gusev Crater, Mars, *Science*, *316*(5825), 738–742.

Stanley, B. D., M. M. Hirschmann, and A. C. Withers (2011), CO_2 solubility in martian basalts and martian atmospheric evolution, *Geochimica et Cosmochimica Acta*, *75*, 5987–6003.

Stanley, B. D., D. R. Schaub, and M. M. Hirschmann (2012), CO_2 solubility in primitive martian basalts similar to Yamato 980459, the effect of composition on CO_2 solubility of basalts, and the evolution of the martian atmosphere, *American Mineralogist*, *in press*.

Sterner, S. M., and K. S. Pitzer (1994), An equation of state for carbon dioxide valid from zero to extreme pressures, *Contributions to Mineralogy and Petrology*, *117*(4), 362–374.

Stewart, A. J., M. W. Schmidt, W. van Westrenen, and C. Liebske (2007), Mars: A new core-crystallization regime, *Nature*, *316*(5829), 1323–1325.

Stolper, E. M., and J. R. Holloway (1988), Experimental determination of the solubility of carbon dioxide in molten basalt at low pressures, *Earth and Planetary Science Letters*, *87*(4), 397–408.

Taylor, W. R., and D. H. Green (1987), The petrogenetic role of methane: Effect on liquidus phase relations and the solubility mechanism of reduced C-H volatiles, in *Magmatic processes: physicochemical principles*, vol. 1, edited by B. O. Mysen, pp. 121–137, Geochemical Society.

Thibault, Y., and J. R. Holloway (1994), Solubility of CO_2 in a Ca-rich leucitite: Effects of pressure, temperature, and oxygen fugacity, *Contributions to Mineralogy and Petrology*, *116*(1-2), 216–224.

Tian, F., M. Claire, J. Haqq-Misra, M. Smith, D. Crisp, D. Catling, K. Zahnle, and J. F. Kasting (2010), Photochemical and climate consequences of sulfur outgassing on early Mars, *Earth and Planetary Science Letters*, *295*(3-4), 412–418.

Trcera, N., D. Cabaret, S. Rossano, F. Farges, A.-M. Flank, and P. Lagarde (2009), Experimental and theoretical study of the structural environment of magnesium in minerals and silicate glasses using X-ray absorption near-edge structure, *Physics and Chemistry of Minerals*, *36*(5), 241–257.

Treiman, A. H. (2005), The nakhlite meteorites: Augite-rich igneous rocks from Mars, *Chemie Der Erde-Geochemistry*, *65*(3), 203–270.

Usui, T., H. Y. McSween, and C. Floss (2008), Petrogenesis of olivine-phyric shergottite Yamato 980459, revisited, *Geochimica et Cosmochimica Acta*, *72*(6), 1711–1730.

Virgo, D., and B. O. Mysen (1985), The structural state of iron in oxidized vs reduced glasses at 1 atm: A ^{57}Fe Mössbauer study, *Physics and Chemistry of Minerals*, *12*(2), 65–76.

Vuilleumier, R., N. Sator, and B. Guillot (2009), Computer modeling of natural silicate melts: What can we learn from ab initio simulations, *Geochimica et Cosmochimica Acta*, *73*(20), 6313–6339.

Wadhwa, M. (2001), Redox state of Mars' upper mantle and crust from Eu anomalies in shergottite pyroxenes, *Science*, *291*(5508), 1527–1530.

Wang, C., J. Hirama, T. Nagasaka, and S. Ban-Ya (1991), Phase equilibria of liquid Fe-S-C ternary system, *ISIJ International*, *31*, 1292–1299.

Wilding, M. C., C. J. Benmore, and J. K. R. Weber (2008), In situ diffraction studies of magnesium silicate liquids, *Journal of Materials Science*, *43*(14), 4707–4713.

Wilding, M. C., C. J. Benmore, and J. K. R. Weber (2010), Changes in the local environment surrounding magnesium ions in fragile MgO-SiO_2 liquids, *Europhysics Letters*, *89*(2), 5.

Wilke, M., C. Schmidt, F. Farges, V. Malavergne, L. Gautron, A. Simionovici, M. Hahn, and P. E. Petit (2006), Structural environment of iron in hydrous aluminosilicate glass and melt-evidence from X-ray absorption spectroscopy, *Chemical Geology*, *229*(1-3), 144–161.

Wilke, M., F. Farges, G. M. Partzsch, C. Schmidt, and H. Behrens (2007), Speciation of Fe in silicate glasses and melts by in-situ XANES spectroscopy, *American Mineralogist*, *92*(1), 44–56.

Williams, J. P., F. Nimmo, W. B. Moore, and D. A. Paige (2008), The formation of Tharsis on Mars: What the line-of-sight gravity is telling us, *Journal of Geophysical Research-Planets*, *113*(E10), E10,011.

Wood, B. J. (1993), Carbon in the core, *Earth and Planetary Science Letters*, *117*, 593–607.

Xirouchakis, D., M. M. Hirschmann, and J. Simpson (2001), The effect of titanium on the silica content and on mineral-liquid partitioning of mantle-equilibrated melts, *Geochimica et Cosmochimica Acta*, *65*(14), 2201–2217.

Zahnle, K., R. S. Freedman, and D. C. Catling (2011), Is there methane on Mars?, *Icarus*, *212*(2), 493–503.

Zipfel, J., P. Scherer, B. Spettel, G. Dreibus, and L. Schultz (2000), Petrology and chemistry of the new shergottite Dar al Gani 476, *Meteoritics and Planetary Science*, *35*(1), 95–106.